Theory of Electronic Conduction in Metal-Graphene Composites

A dissertation presented to

the faculty of

the College of Arts and Sciences of Ohio University

In partial fulfillment

of the requirements for the degree

Doctor of Philosophy

Kishor Nepal

August 2026

This dissertation titled

Theory of Electronic Conduction in Metal-Graphene Composites

by

KISHOR NEPAL

has been approved for

the Department of Physics and Astronomy

and the College of Arts and Sciences by

David A. Drabold

Distinguished Professor of Physics

Matthew Ando

Dean, College of Arts and Sciences

Abstract

NEPAL, KISHOR, Ph.D., August 2026, Physics

Theory of Electronic Conduction in Metal-Graphene Composites (138 pp.)

Director of Dissertation: David A. Drabold

The primary focus of this dissertation is to investigate the mechanisms of electrical conduction in metal-carbon composites, with particular emphasis on the intriguing phenomenon of enhanced conductivity enabled by graphene additives. While increased conductivity in metal-graphene composites challenges traditional principles like Matthiessen's rule, which states that electrical conductivity decreases with additives, this research provides a physical explanation for the experimentally observed mechanism and offers valuable insights into optimizing metal-graphene composites for advanced electrical applications.

The foundational research on metal-graphene composites under structural stress reveals key factors contributing to enhanced electronic conductivity: (a) improved interactions between aluminum's valence electrons and graphene's π-electrons, (b) increased electronic density of states at the Fermi level, (c) the formation of a self-organized low-energy registry at the metal-graphene interface, and (d) semi-conducting like temperature dependence at elevated temperature. Next, the dissertation focuses on the potential of coal-derived graphene for ultraconductors, systematically examining how graphene's quality, specifically its purity, structure, and defect density, affects the composite's electrical performance.

Next, the dissertation presents a novel computational framework, the "N^2 method," developed to map and quantify regions of high electrical conduction in the materials. The method offers a spatially resolved perspective in electronic behavior, revealing localized conduction pathways at the atomic scale. This capability is particularly valuable for understanding and optimizing interfaces and interconnects in advanced electronic devices. By providing both predictive insight and design guidance, the N^2 method serves as a

powerful tool for linking atomic-scale structure to macroscopic electrical performance in metal-carbon composites and related materials.

This dissertation integrates a collection of papers that provide in-depth insights into the fundamental structural and electronic dynamics at metal-carbon interfaces, as well as the resulting electrical conductivity and transport behavior. By linking interface structure, material quality, and conduction mechanisms, this dissertation advances both the fundamental understanding of metal-carbon composites and their practical application in high-performance electronic materials.

Dedication

To my family, whose unwavering love, sacrifices, and belief in me have carried me through every challenge. To my wife, Barsha, whose patience, strength, and constant encouragement have been my anchor and inspiration.

ACKNOWLEDGMENTS

To my Doctoral committee members — Dr. Gang Chen, Dr. David Ingram, and Dr. Sumit Sharma — thank you for being an integral part of this success story.

Dr. Eric Stinaff (Physics Department Chairperson) and Dr. Daniel Philips (Physics Graduate Program Director) - thank you for your leadership, guidance, and steadfast support that shaped my academic journey.

Dr. Keerti Kappagantula (Chief Scientist) and Dr. Yahya Al-Majali (Director of the Institute for Sustainable Energy and the Environment) - thank you for being an exceptional colleague and an even better mentor.

To my people, Chinonso Ugwumadu, Aashish Gautam, Ridwan Hussein, Yoon Gyu Lee, Kashi Subedi, Rajendra Thapa, and Bikash Chauhan — You always have a special place in my heart.

To my advisor, Dr. David A. Drabold - whose guidance, encouragement, and unwavering support have shaped every step of this work. I am truly grateful for the opportunity to learn under your mentorship.

Table of Contents

List of Tables

List of Figures

List of Acronyms

BAD	Bond Angle Distribution
BLD	Bond Length Distribution
CPC	Coal-Plastic Composites
DFT	Density Functional Theory
EDoS	Electronic Density of States
EIPR	Electronic Inverse Participation Ratio
FTIR	Fourier Transform Infrared Spectroscopy
GAP	Gaussian Approximation Potential
GGA	Generalized Gradient Approximation
LAMMPS	Large-scale Atomic/Molecular Massively Parallel Simulator
LDA	Local Density Approximation
MD	Molecular Dynamics
MoFaSA	Model Filtering and Scoring Algorithm
NMR	Nuclear Magnetic Resonance
PAW	Projector-augmented Wave
PBE	Perdew-Burke-Ernzerhof
RDF	Radial Distribution Function
SEM	Scanning Electron Microscopy
SOAP	Smooth Overlap of Atomic Positions
SPC	Space Projected Conductivity
VASP	Vienna *Ab initio* Simulation Package
VDoS	Vibrational Density of States
VIPR	Vibrational Inverse Participation Ratio
XPS	X-ray Photoelectron Spectroscopy
XRD	X-ray Difraction

1 Introduction

1.1 Metal Composites

High electrical conductivity remains the primary requirement in power transmission systems, electric motors, generators, cables, and transformers. Pure copper has traditionally dominated these applications due to its superior intrinsic conductivity. Although less conductive, aluminum is used for its low density, abundance, and favorable cost-to-weight ratio. Over the last two decades, increasing global demand for energy efficiency has driven the development of copper-based composite systems with enhanced transport properties, aimed at reducing Joule heating losses in electrical infrastructure [4, 5]. In parallel, efforts have focused on engineering aluminum-based materials capable of narrowing the copper conductivity gap while preserving the practical advantages of aluminum [6].

To achieve such performance enhancements, research has increasingly shifted from conventional alloy design toward deliberate microstructural engineering [4, 7]. The pursuit of ultra-conductive materials has expanded beyond classical solid-solution alloying to microstructural engineering strategies in which trace additives or secondary phases are incorporated through processes such as high-temperature annealing and severe plastic deformation [8, 9]. These routes produce refined microstructures and metastable interfacial conformations that can significantly influence charge transport behavior. Of particular scientific interest are experimental observations indicating that certain face-centered cubic (FCC) metals exhibit modest but measurable increases in electrical conductivity upon the addition of trace quantities of specific additives [10–12]. This behavior is counterintuitive, as classical impurity scattering models and Matthiessen's rule predict that alloying decreases conductivity due to enhanced electron scattering. The mechanisms responsible for such anomalous transport responses remain insufficiently understood within conventional theoretical frameworks.

1.2 Graphene as Additive for Ultra-Conductors

Among emerging composite systems, metal–graphene composites have attracted significant attention due to enhanced electronic performance. Copper–graphene (Cu–G) and Aluminum-Graphene (Al-G) composites, in particular, have demonstrated promising enhancements in electrical conductivity. Several experimental studies have reported enhanced electrical conductivity in Cu–G composites [13–16]. Such observations challenge the classical interpretation of metallic conduction based on Matthiessen's rule, which states that the addition of impurities or secondary phases increases electron scattering and hence reduces electrical conductivity [17]. A well-known example is the addition of silver to copper, which lowers conductivity despite silver's higher intrinsic conductivity [18].

Recent experimental discoveries by Kappagantula and co-workers, using solid-phase hot extrusion, demonstrated that graphene-related impurities can enhance electrical conductivity in both aluminum and copper beyond that of high-quality pure metals [10–12]. These materials also exhibit a favorable temperature dependence of conductivity (improved conductivity at elevated temperatures required for applications), suggesting the formation of unusual, high-energy interfacial conformations accessible only through non-equilibrium processing. Processing protocols also play a critical role. Techniques that allow atomic-scale control, such as vapor deposition and molecular beam epitaxy, have demonstrated enhanced conductivity in nano- to micron-scale samples [19]. At the bulk scale, solid-phase processing methods, particularly hot extrusion, have proven effective in producing ultraconductive metal–graphene wires [10–12].

Despite these advances, the atomistic mechanisms governing charge-carrier transport across metal–graphene interfaces remain poorly understood. While carrier mobility in graphene deposited on copper foils has been studied [20, 21], comparatively little work

has focused on transport across metal–graphene interfaces embedded within composite microstructures. In particular, the influence of interfacial atomic arrangement, separation distance, and electronic structure on charge transfer remains unclear.

Two prevailing hypotheses have emerged to describe the mechanisms responsible for the enhanced conductivity observed in metal–graphene composites. The first suggests that graphene templates copper grain growth, promoting the formation of highly conductive (111) textures. In this case, graphene indirectly enhances conductivity without actively participating in transport. The second hypothesis posits that graphene directly participates in electronic conduction through carrier exchange with the surrounding metal matrix, a process that depends critically on the nature of the metal–graphene interface. Although Cu and Al (111) are known to have minimal lattice mismatch with graphene, the quantitative contribution of graphene to overall conductivity remains unresolved. Further, the electrical conductivity of metal–graphene composites depends strongly on graphene-related parameters, including graphene content, crystallinity, defect density, and spatial distribution within the metal matrix [10, 22]. These findings highlight the need for atomistically resolved theoretical frameworks capable of explaining enhanced conduction mechanisms.

1.3 Coal-Derived Graphene for Metal–Carbon Composites

The growing global graphite deficit at associated increase in its cost [23], has intensified interest in coal-derived graphene as a scalable and cost-effective alternative for metal–carbon composite applications [24–28]. Unlike pristine graphene produced via chemical vapor deposition or exfoliation, which remains expensive and limited in scalability [29, 30], coal-derived graphene leverages abundant and inexpensive raw materials.

Despite this reality, most prior theoretical and experimental studies have focused almost exclusively on crystalline graphene interfaces [31–42]. This dissertation departs from that paradigm by modeling metal–amorphous graphene interfaces and coal-derived graphene composites, providing a more realistic representation of experimentally processed composites. Amorphous graphene is a topologically disordered carbon structure with unique mechanical and electronic properties [43–49]. The amorphous graphene layers studied here are derived from amorphous graphite [50], with formation and simulation details described elsewhere [51–53].

Coal-derived graphene can be produced through a variety of methods, including pyrolysis, chemical exfoliation, microwave-assisted synthesis, and laser-induced graphene techniques [26, 27, 54–62]. However, such materials inherently contain structural disorder, defects, and chemical functional groups, raising critical questions about how non-crystallinity affects electronic transport in metal–graphene composites. In particular, coal-derived graphene introduces additional complexity due to its inherent defect structures, functional groups, and chemical heterogeneity, which can fundamentally alter metal–graphene interactions. Within this framework, the dissertation systematically examines the structural, electronic, and transport behavior of copper–coal composites to identify the key mechanisms that control conductivity and establish theoretical guidelines for optimizing composite performance under realistic processing conditions.

By extending analysis beyond pristine crystalline graphene to include amorphous and coal-derived graphene, this dissertation provides a unified and realistic theoretical framework for understanding enhanced conductivity in metal–carbon composites. The results advance fundamental knowledge of interfacial charge transport while offering practical guidance for designing next-generation ultraconductive materials.

The scientific contributions of this work are documented through a series of publications. These publications both support the results presented in the following

chapters and highlight the broader impact of the research. The dissertation includes the following primary publications as part of the work:

A1. **K. Nepal**, R. Hussein, Y. Al-Majali, and D. A. Drabold, "Electronic conduction in copper–graphene composites with functional impurities," *The Journal of Chemical Physics*, vol. 163, no. 12, Sep. 2025.

A2. **K. Nepal**, C. Ugwumadu, F. Kraft, Y. Al-Majali, and D. Drabold, "The effects of crystal orientation and common coal impurities on electronic conductivity in copper–carbon composites," *Carbon*, vol. 231, p. 119711, 2025.

A3. **K. Nepal**, C. Ugwumadu, A. Gautam, K. Kappagantula, and D. Drabold, "Electronic conductivity in metal-graphene composites: The role of disordered carbon structures, defects, and impurities," *Journal of Physics: Materials*, vol. 7, no. 2, p. 025003, 2024.

A4. **K. Nepal**, C. Ugwumadu, K. N. Subedi, K. Kappagantula, and D. A. Drabold, "Physical origin of enhanced electrical conduction in aluminum-graphene composites," *Applied Physics Letters*, vol. 124, no. 9, p. 091902, 2024.

A5. K. N. Subedi, **K. Nepal**, C. Ugwumadu, K. Kappagantula, and D. A. Drabold, "Electronic transport in Copper–graphene composites," Applied Physics Letters, vol. 122, p. 031 903, 2023.

In addition to the research directly presented in this dissertation, I have contributed to other projects and publications, not directly related to the dissertation topic. However, these publications demonstrate the broader contributions to the field of electronic transport in materials.

A1. **K. Nepal** et al., "Electronic and Thermal properties of the Phase Change Memory Material GST225 and results from spatially resolved transport calculations," *Solid State Sciences*, vol. 173, p. 108182, 2026.

A2. **K. Nepal**, A. Gautam, C. Ugwumadu, and D. Drabold, "New models of clean and hydrogenated amorphous silicon surfaces," *Journal of Non-Crystalline Solids*, vol. 660, p. 123517, Jul. 2025.

1.4 Outline of Dissertation

This dissertation builds on previous experimental and theoretical studies by systematically investigating the role of graphene quality, disorder, functionalization, and interfacial conformation in the governance of electronic transport in metal–graphene composites.

This dissertation is organized as follows: Chapter 2 focuses on the theoretical and computational framework of the dissertation. Chapter 3 details the incorporation of layers(s) of graphene into copper and aluminum grains, providing the physical explanation of enhanced electronic performances in composites. Chapter 4 extends the discussion to the effects of topological disorders, metal orientations, and impurities in metal-graphene composites. In Chapter 5, realistic graphene structures similar to coal-derived graphene are simulated and incorporated into a copper matrix. Detailed electronic conductivity and transport properties of coal-metal composites are presented. Finally, Chapter 6 concludes the findings of this dissertation.

2 Electronic Transport in Metal-Graphene Composites

2.1 Density Functional Theory and the Kohn–Sham Formalism

Density Functional Theory (DFT) is a first-principles framework for describing the ground-state properties of interacting many-electron systems. In DFT, the total energy of a system is expressed as a functional of the electron density, $\rho(\mathbf{r})$. The Hohenberg–Kohn theorems [63] establish that (i) the ground-state electron density uniquely determines all properties of a many-electron system, and (ii) the total energy functional achieves its minimum at the true ground-state density.

In the widely used Kohn–Sham (KS) formulation [63], the interacting many-body system is mapped onto a fictitious system of non-interacting electrons moving in an effective potential. The Kohn–Sham equations are written as:

$$\hat{H}_{\mathrm{KS}}\psi_i(\mathbf{r}) = \varepsilon_i\psi_i(\mathbf{r}), \quad i = 1, 2, \ldots, N, \tag{2.1}$$

where $\psi_i(\mathbf{r})$ are the single-particle Kohn–Sham orbitals, ε_i are the corresponding eigenvalues, and N is the total number of electrons. The Kohn–Sham Hamiltonian is given by:

$$\hat{H}_{\mathrm{KS}} = -\frac{\hbar^2}{2m}\nabla^2 + V_{\mathrm{ext}}(\mathbf{r}) + V_H[\rho](\mathbf{r}) + V_{\mathrm{XC}}[\rho](\mathbf{r}). \tag{2.2}$$

Here:

- $-\frac{\hbar^2}{2m}\nabla^2$ is the kinetic energy operator of the non-interacting electrons,
- $V_{\mathrm{ext}}(\mathbf{r})$ is the external potential due to atomic nuclei,
- $V_H[\rho](\mathbf{r}) = e^2 \int \frac{\rho(\mathbf{r}')}{|\mathbf{r}-\mathbf{r}'|} d\mathbf{r}'$ is the classical Hartree potential describing electron–electron Coulomb repulsion,

- $V_{\mathrm{XC}}[\rho](\mathbf{r}) = \frac{\delta E_{\mathrm{XC}}[\rho]}{\delta \rho(\mathbf{r})}$ is the exchange–correlation potential, which captures all quantum many-body effects beyond the Hartree term.

2.2 Exchange–Correlation Functional

A central component of Density Functional Theory is the exchange-correlation (XC) functional, which accounts for all many-body effects beyond the classical Hartree term. In this work, the generalized gradient approximation (GGA) was employed. GGA functionals depend not only on the local electron density $\rho(\mathbf{r})$ but also on its gradient $\nabla\rho(\mathbf{r})$, allowing for a more accurate description of spatial variations in the electron density:

$$E_{\mathrm{XC}}^{\mathrm{GGA}}[\rho] = \int f(\rho(\mathbf{r}), \nabla\rho(\mathbf{r}))\, d\mathbf{r}. \tag{2.3}$$

To accurately capture long-range interactions, which are particularly important at metal–graphene and metal–amorphous carbon interfaces, a van der Waals (vdW) correction was included. This correction accounts for dispersion forces that are not inherently described by standard GGA functionals, ensuring a realistic description of interfacial binding, electron density overlap, and charge transfer phenomena.

GGA with vdW corrections provides a reliable framework for modeling both crystalline and amorphous graphene in contact with FCC metals such as copper and aluminum, enabling accurate predictions of structural, electronic, and interfacial properties. A proper review of this vast and mature field can be found in book of R.M. Martin [64].

2.3 Electronic Structure Calculations

First-principles calculations based on DFT [64] were employed to investigate the electronic and transport properties of metal–graphene and metal–coal composite systems. The Kohn–Sham equations were solved self-consistently using the projector augmented-wave (PAW) method [65, 66] as implemented in the plane-wave basis Vienna *Ab initio*

Simulation Package (VASP) [67]. The plane wave energy cutoff is carefully chosen to ensure convergence of total energy and atomic forces. The electronic density $\rho(\mathbf{r})$ was iteratively updated until self-consistency was achieved, with convergence criteria applied to both the total energy and the atomic forces. For selected systems, complementary atomic-orbital-based calculations were performed using the Spanish Initiative for Electronic Simulations with Thousands of Atoms (SIESTA) [68], enabling efficient treatment of large, disordered, or amorphous systems.

These approaches allow simulations across different length and time scales and provide flexibility in treating crystalline, disordered, and interface systems. In addition, classical molecular dynamics simulations were carried out using the Large-scale Atomic/Molecular Massively Parallel Simulator (LAMMPS) [69], including implementations based on machine-learning interatomic potentials such as the Gaussian Approximation Potential (GAP) framework [70, 71]. The combined use of first-principles and machine-learning-based simulations enables efficient modeling of large and complex atomic systems while retaining near first-principles accuracy.

2.3.1 Electronic Features

The electronic structure of materials was analyzed using the total electronic density of states (EDoS), partial density of states (PDoS), and the electronic inverse participation ratio (EIPR). These quantities provide insight into the electronic spectrum and the degree of localization of single-particle states.

In this work, the electronic states are represented by single-particle Kohn–Sham eigenstates obtained from ground state calculations. For finite systems, the electronic density of states is a quantity defined as

$$N(\epsilon) = \frac{1}{N} \sum_i \delta(\epsilon - \epsilon_i), \tag{2.4a}$$

where N denotes the size of the basis set and ϵ_i is the ith Kohn–Sham eigenvalue.

The degree of localization of an electronic eigenstate is quantified using the electronic inverse participation ratio (EIPR), defined as

$$I(\psi_n) = \frac{\sum_i |c_n^i|^4}{\left(\sum_i |c_n^i|^2\right)^2}, \tag{2.5}$$

where c_n^i represents the contribution of the ith basis function (e.g., atomic orbitals, projected from the plane wave basis for VASP or directly with SIESTA) to the eigenstate ψ_n. Localized electronic states yield large EIPR values (approaching unity), whereas extended states exhibit values that scale inversely with the system size, i.e., $I \sim 1/N$.

2.4 Vibrational Properties

Vibrational properties were investigated within the harmonic approximation by computing the vibrational density of states (VDOS) and the vibrational inverse participation ratio (VIPR). The vibrational modes were obtained by constructing the dynamical matrix from finite differences of atomic forces, defined as

$$D_{ij}^{\alpha\beta} = \frac{1}{\sqrt{m_i m_j}} \frac{\partial^2 E}{\partial u_i^\alpha \partial u_j^\beta}, \tag{2.6}$$

where u_i^α denotes a small displacement of atom i along the Cartesian direction α, m_i is the atomic mass, and E is the total potential energy.

The vibrational eigenvalue problem at the Brillouin zone center ($\mathbf{k} = 0$) is given by

$$\omega_m^2 \, e_i^{\alpha,m} = \sum_{j,\beta} D_{ij}^{\alpha\beta} \, e_j^{\beta,m}, \tag{2.7}$$

where ω_m is the vibrational frequency of mode m and $e_i^{\alpha,m}$ is the corresponding eigenvector component.

The vibrational inverse participation ratio (VIPR) for mode m is defined as

$$g(m) = \frac{\sum_{i,\alpha} |e_i^{\alpha,m}|^4}{\left(\sum_{i,\alpha} |e_i^{\alpha,m}|^2\right)^2}, \tag{2.8}$$

which provides a quantitative measure of vibrational localization, much like EIPR. Extended vibrational modes yield $g \sim 1/N$, whereas highly localized modes approach unity.

The dynamical matrix (DM) is constructed by displacing each atom from its equilibrium position along the Cartesian directions and computing the resulting forces. These vibrational modes were subsequently used to analyze vibrational transport properties, including the VDOS and VIPR. For large systems, direct calculation of the dynamical matrix within VASP and SIESTA is computationally prohibitive due to the massive size of the force constant matrix and the large number of finite displacements required. To overcome this, we employed a machine-learning Gaussian Approximation Potential within the LAMMPS.

2.5 Kubo-Greenwood Formula and Space Projected Conductivity

The statistical mechanics of linear response, as explored by Kubo [72], provides a framework for studying how a material responds to external perturbations. In the case of an AC electric field, Kubo investigated the linear response of a material and derived an expression for the electrical conductivity. The resulting expression for electrical conductivity, known as the Kubo-Greenwood formula (KGF), was obtained by approximating the electronic structure within a single-particle picture [72, 73]. The KGF is a mathematical formula that relates the electrical conductivity of a material to its response to an external AC electric field. The expression, for our simplicity, is averaged over the diagonal elements of the conductivity tensor ($\sigma_{\alpha\alpha}$), α is a cartesian coordinate index (x, y, z), for any frequency ω is written as:

$$\sigma(\omega) = \frac{2\pi e^2}{3m^2\Omega\omega}\sum_k w_k \sum_{i,j}\sum_{\alpha}[f(\epsilon_{i,k} - f(\epsilon_{j,k}]| < \psi_{j,k}|P^{\alpha}|\psi_{i,k} >|^2\delta(\epsilon_{j,k} - \epsilon_{i,k} - \hbar\omega) \quad (2.9)$$

where, e and m respectively are electronic charge and mass, Ω is the volume of the supercell, w_k's are the integration weight factors for k-points, and i and j are band numbers for Kohn-Sham states $\psi_{i,j}$ with associated energies $\epsilon_{i,j}$, P^α is a momentum operator along α direction, and f($\epsilon_{i,j}$) denotes the Fermi-Dirac distribution weight. The Kubo-Greenwood formula has become a widely used method for computing electronic conductivity in various materials to calculate the electrical conductivity of materials quantitatively. This approach has proven valuable in studying the transport properties of conductors, semiconductors, and other materials within tight-binding and DFT approximations [64, 74], and may be employed with better (post-DFT) estimates of excited states [75].

Detailed in [76], KGF can be exploited to gain a microscopic understanding of the systems, i.e., get the spatial information of the conduction (called space projected conductivity (SPC)). A concise derivation provided here follows from [76]. Define

$$g_{i,j,k} = \frac{2\pi e^2}{3m^2\Omega\omega}[f(\epsilon_{i,k} - f(\epsilon_{j,k}]\delta(\epsilon_{j,k} - \epsilon_{i,k} - \hbar\omega)$$

and the matrix elements of conductivity are written in position representation with x and x' (real space grid points), such that Equation 2.9

$$\sigma = \sum_k w_k \sum_{i,j,\alpha} \int dx \int dx' g_{i,j,k}[\psi^*_{j,k}(x)P^\alpha\psi_{i,k}(x)][\psi_{j,k}(x)P^\alpha\psi_{i,k}(x)]^* \tag{2.10}$$

A complex-valued function: $\zeta^\alpha_{ijk}(x) = \psi^*_{j,k}(x)P^\alpha\psi_{i,k}(x)$ defined on a discrete real-space grid uniformly spaced in a 3D supercell with spacing h is defined. Next, approximating the integrals as sums on the grid

$$\sigma \approx h^6 \sum_k w_k \sum_{i,j,\alpha} \sum_{x,x'} g_{i,j,k}[\zeta^\alpha_{ijk}(x)][\zeta^\alpha_{ijk}(x')]^* \tag{2.11}$$

The Conduction matrix (Γ matrix) is defined as

$$\Gamma(x, x') = h^6 \sum_k w_k \sum_{i,j,\alpha} g_{i,j,k} [\zeta^{\alpha}_{ijk}(x)][\zeta^{\alpha}_{ijk}(x')]^* \tag{2.12}$$

which is hermitian and positive semi-definite, the matrix elements of which have the dimension of conductivity, and summation over x and x' gives the total conductivity of the system within a limit as $h \to 0$. i.e.,

$$\sigma = \sum_{x,x'} \Gamma(x, x') \tag{2.13}$$

Carrying the summation just over x' gives conductivity at grid x, which we term Space Projected Conductivity (SPC):

$$\zeta(x) = |\sum_{x'} \Gamma(x, x')| \tag{2.14}$$

The modulus is taken to generate a real value for the scalar field ζ. $\zeta(x)$, by construction, offers spatial information concerning the conductivity on the real-space grids x. A code has been developed and efficiently implemented to study the evolution of conduction through different materials [76–78].

2.5.1 Temperature Dependence of Electronic Conductivity

Developing a predictive theory of electronic transport with potential materials design applications requires explicit consideration of both the temperature dependence of conductivity and its spatial variation at the atomistic level.

Various theoretical frameworks exist for incorporating temperature effects into electronic transport calculations. In this work, an adiabatic approximation [79] is adopted, in which the finite-temperature electrical conductivity is obtained by thermally averaging the Kubo–Greenwood formula. Specifically, the conductivities are evaluated for an instantaneous atomic configuration sampled from a constant-temperature molecular

dynamics (MD) simulation, and the final conductivity is obtained by averaging over these configurations.

This method relies on the Born–Oppenheimer approximation, assuming that electrons respond instantaneously to atomic configurations. Under this assumption, the thermally averaged Kubo–Greenwood conductivity accounts for lattice vibrations and thermal disorder, and the temperature dependence of the electronic conductivity arises solely from averaging the conductivity over MD-generated configurations at constant temperature.

Although classical molecular dynamics does not provide a quantum-mechanically exact description of ionic motion, below the Debye temperature θ_D, it generates a statistically meaningful ensemble of atomic configurations. When combined with the Kubo–Greenwood formalism and adiabatic averaging, this ensemble yields a reliable and computationally tractable description of temperature-dependent electronic conductivity in both crystalline and disordered materials.

Previous studies have demonstrated that this method successfully reproduces the temperature dependence of electrical conductivity in crystalline and disordered systems [80], surprisingly including well below the Debye temperature (θ_D). Thus, although classical MD does not provide a quantum-mechanically accurate description of atomic trajectories below θ_D due to the absence of lattice quantization, it appears to generate a statistically meaningful ensemble of atomic configurations. When combined with the Kubo–Greenwood formalism, this ensemble provides a reliable basis for evaluating temperature-dependent electronic transport properties.

To demonstrate the robustness of the methodology for computing temperature-dependence, a 256-atom face-centered cubic (FCC) copper model was employed. The system was equilibrated at constant temperatures ranging from 50 to 350 K, allowing lattice vibrations and thermal disorder to develop naturally during the simulations. At each temperature, multiple statistically independent atomic configurations are sampled, and the

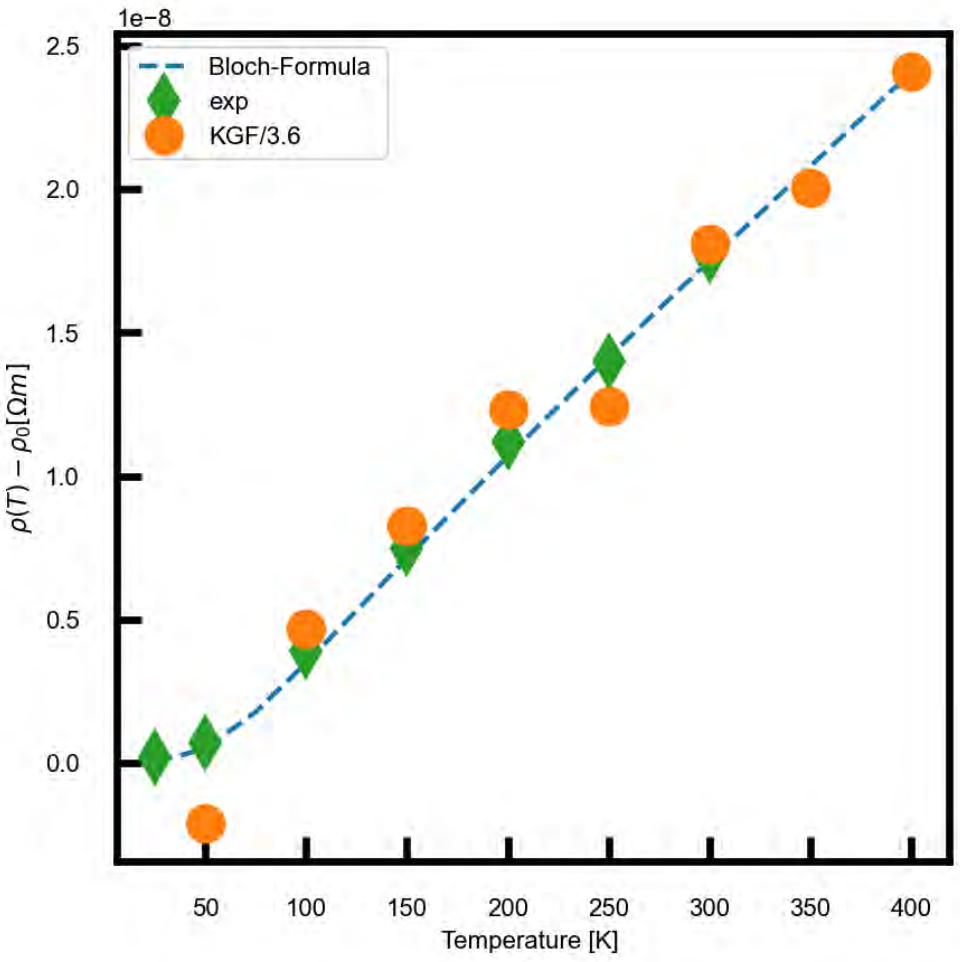

Figure 2.1: Average Kubo-Greenwood Formula (KGF) electronic conductivity plotted versus annealing temperature for FCC copper. KGF conductivities fitted to the Bloch Formula for resistivity and the experimental value [1]. To compute the average KGF conductivity, 10 snapshots were taken at 50-fs intervals over 3-ps annealing.

electronic conductivity is computed using the Kubo–Greenwood approach. This ensures that the resulting transport properties explicitly account for instantaneous atomic disorder and thermally induced electron–phonon scattering. The resistivity extracted from these conductivity values is subsequently analyzed using the Bloch–Grüneisen model for metals [81], expressed as

$$\rho(T) = \rho_0 + A\left(\frac{T}{\theta_D}\right)^5 \int_0^{\theta_D/T} \frac{x^5}{(1-e^{-x})(e^x-1)}\,dx, \tag{2.15}$$

where ρ_0 is the residual resistivity, θ_D is the Debye temperature, and A is a material constant. The close consistency between the MD + KGF predictions and the Bloch–Grüneisen behavior demonstrates that this approach accurately captures the microscopic physics governing temperature-dependent resistivity in copper, validating the methodology as a robust and physically grounded framework for studying finite-temperature electronic transport in FCC metal and metal–graphene composite systems.

2.6 Electronic Conduction Activity Estimates From Squared Density of States at the Fermi Level

Associated Publication

1. **K. Nepal**, C. Ugwumadu, F. Kraft, Y. Al-Majali, and D. A. Drabold, The effects of crystal orientation and common coal impurities on electronic conductivity in copper-carbon composites, Carbon 231 119711 (2025)

The SPC technique has been widely and successfully used to analyze electronic transport pathways in diverse materials, including carbon-based systems [50, 52], metals [78, 82], metal–carbon composites [77, 83, 84], glasses [85], and various oxides [86, 87]. Although SPC offers deep physical insight into transport phenomena, its computational expense can become substantial, particularly for large-scale atomistic systems. Efficiently identifying conductive regions is not only important for understanding fundamental transport but also for guiding the design of technologies such as conducting-bridge RAM (CBRAM), physical unclonable function (PUF) devices, and other systems where atomistic-level charge transport plays a critical role [88, 89]. Several alternative approaches have been explored, such as the $q_i - q_j$ wavefunction-overlap method [85] and techniques based on probing the Kohn–Sham charge density at the Fermi level [90].

In this section, we introduce a simplified yet highly efficient alternative, referred to as the N^2 method, which significantly reduces computational overhead while retaining meaningful resolution of conductive pathways. Unlike SPC, the N^2 method scales more favorably for large systems and is straightforward to implement, making it particularly advantageous within localized-basis DFT frameworks such as SIESTA. This provides a practical and scalable route to assess electronic transport characteristics in complex and realistic material systems.

2.6.1 Random Phase Approximation and Electrical Conductivity

In the sixties and seventies, much research was on electronic eigenfunctions in disordered systems, especially near an optical gap. This was near the heart of some of the most important ideas in solid state theory at the time: Anderson localization and Mott's "mobility edge" (indeed, Anderson, Mott, and Van Vleck shared the 1977 Nobel Prize in Physics for research on disordered systems). To make progress, simple approximations were invoked.

One such idea was the so-called *Random Phase Approximation* (RPA) [91–94], introduced to study the electrical conductivity of disordered systems. The assumption in such systems is that in conducting states, the phase of the probability amplitude for finding an electron on a particular basis orbital varies randomly. Sums of such terms might be expected to exhibit considerable cancellation, and if this assumption is made, simplified (and approximate) expressions for the conductivity accrue.

Here, the RPA method of Hindley is tersely described. The method has its origins in the work of Mott [95] and Cohen [96]. It is emphasized that this is highly approximate but appears from this and other work to be useful in conjunction with the visualization of conduction active parts of a complex network.

Hindley expands the energy eigenstates $\psi_i(\mathbf{r})$ as:

$$\psi_i(\mathbf{r}) = \sum_n \alpha_{i,n}\phi_n(\mathbf{r} - \mathbf{R}_n) \tag{2.16}$$

where $\phi_n(\mathbf{r} - \mathbf{R}_n) \equiv |\phi_n\rangle$ represents an orthogonal localized wave function, or more realistically, an orthonormal Wannier function[1], centred at atomic site $\mathbf{R}_n$. The expansion coefficient is denoted as $\alpha_{i,n}$. It is noteworthy that in the present version of the argument, **k**-space dispersion has been neglected, an assumption that holds for sufficiently large systems where the entire Brillouin zone can be approximated by the Γ point, as is common in large-scale *ab initio* calculations.

From Equation 2.16, the matrix elements for the momentum operator $\hat{\boldsymbol{p}}$ in the energy representation is:

$$P_{i,i'} = \sum_{n,n'} \alpha^*_{i',n'}\alpha_{i,n}p_{n,n'} \tag{2.17a}$$

$$p_{n,n'} = \langle\phi_n|\hat{\boldsymbol{p}}|\phi_{n'}\rangle \tag{2.17b}$$

where $p_{n,n'}$ are the momentum matrix element between the basis states.

In what follows, i and i' index energy eigenfunctions, and m, m', n, n' index basis orbitals. From the Kubo-Greenwood formula, the squared momentum matrix elements are required. The average of the squared momentum matrix elements between energy eigenstates is:

$$\overline{|P_{i,i'}|^2} = \sum_{n,n'}\sum_{m,m'} \overline{\alpha^*_{i',n'}\alpha_{i',m'}\alpha_{i,n}\alpha^*_{i,m}p_{n,n'}p^*_{m;m'}} \tag{2.18}$$

The RPA *assumes* that the phases of $\alpha_{i,n}$ are "random" (more precisely, of such a character that when they are summed, there are cancellations so pronounced that off-diagonal terms are ignored). That is, for:

- $i \neq i'$, phase randomness averages out the off-diagonal terms.

[1] Realistic Wannier functions are not perfectly localized to a single site. The most localized forms decay at best as fast as the density matrix while exhibiting oscillations to preserve orthogonality [97–100].

- $i = i'$, only terms where $m = m'$ and $n = n'$ contribute significantly.

This leads to an approximate relation between the matrix elements of momentum matrix elements in the energy representation i and basis functions n:

$$\overline{|P_{i,i'}|^2} \approx \frac{1}{NV}\overline{\sum_{n,n'} |p_{n,n'}|^2} \tag{2.19}$$

in which N is the atomic number density and V the volume. The electronic conductivity is provided by an energy quadrature of $\kappa(E)$ near the Fermi level as [101]:

$$\kappa(E) = \frac{2\pi\hbar}{3m^2V}\sum_{i',i} |P_{i,i'}|^2 \delta(\epsilon_{i'} - E)\delta(\epsilon_i - E) \tag{2.20}$$

In this formulation, if ψ_i is an eigenstate of the Hamiltonian, then ϵ_i is the conjugate eigenvalue. The spectral function $\kappa(E)$ vanishes for energies at which states are localized. By applying Equation 2.19, along with the definition of the density of states, $N(E)$, and making a few straightforward approximations, one finds that:

$$\kappa(E) \propto [N(E)]^2. \tag{2.21}$$

Carrying out the integral for $T \to 0$, the DC conductivity is approximately proportional to the *squared* density of states at the Fermi level:

$$\sigma \propto N^2(\epsilon_f) \tag{2.22}$$

This approximation is expected to be reasonable for extended electron states at the Fermi level, ϵ_f.

Mott carries out a similar analysis, concluding that:

$$\sigma \propto \overline{|P_{i,i'}|^2}[N(\epsilon_f)]^2 \tag{2.23}$$

where the averaged squared momentum matrix element is over electronic states at the Fermi level (such that, at $T \to 0$, $E_i = E_{i'} = \epsilon_f$). This form emphasizes that the DC conductivity is due to electronic transitions at the Fermi level.

2.6.2 The N^2 Method

The N^2 method is our simplified means to obtain real-space information on electronic conduction. It is a consequence of the random phase approximation (RPA) implemented with the KGF [91–93, 95, 102]. At low temperatures, the conductivity is determined by electrons near the Fermi energy (ϵ_f); Mott derived an equation for DC conductivity:

$$\sigma \propto [N(E)]^2\Big|_{E=\epsilon_f} \tag{2.24}$$

Equation 2.24 indicates that the electronic conductivity, σ, is proportional to the square of the electronic density of states, $N^2(\epsilon_f)$.

Hindley arrived at the same conclusion using the RPA and Luttinger's equation for electronic conductivity [101], as detailed in [94] and briefly revisited in 2.6.1. Both analyses reveal that in systems with extended states near the Fermi level, conductivity scales with N^2. However, in the presence of strong disorder and localized states at ϵ_f, the assumptions underlying the RPA break down, as strong disorder can lead to Anderson localization, where wavefunctions become highly localized. For this method, the cancellation from wave-mechanical interference is assumed. Extended states are observed near ϵ_f for the metal-graphene system, making this approximation appropriate.

A question then arises: *what spatial distribution, $N^2(\epsilon_f, \boldsymbol{r})$, ensures that integrating this distribution provides meaningful insights into the material's conductivity?* To obtain this spatial distribution at $E = \epsilon_f$, the electronic density of states at ϵ_f is first defined as:

$$N(\epsilon_f) = \frac{1}{M}\sum_i \delta_f^i \tag{2.25a}$$

$$\delta_f^i = \delta(\epsilon_i - \epsilon_f) \tag{2.25b}$$

where i represents the band number and M is the dimension of the single-particle Hamiltonian, for example, the Kohn-Sham Hamiltonian. Brillouin zone integrals are ignored here, which is appropriate only for large cells. From Equation 2.25a, the spatial projection of $N^2(\epsilon_f)$ is obtained as:

$$\zeta(\epsilon_f, \mathbf{r}) = \frac{1}{M^2}\sum_{i,j} \delta_f^i \delta_f^j |\psi_i(\mathbf{r})|^2 |\psi_j(\mathbf{r})|^2 \tag{2.26}$$

Here, $|\psi_i(\mathbf{r})|^2$ is the probability density of the i^{th} Kohn-Sham orbital at position $\mathbf{r}$. The volume integral of the Equation 2.26 does *not* directly yield $N^2(\epsilon_f)$, since the integral of $|\psi_i(\mathbf{r})|^2|\psi_j(\mathbf{r})|^2$ is an intricate function of the overlapping wavefunctions [85]. To fix this, a modified form of Equation 2.26 is taken:

$$\bar{\zeta}(\epsilon_f, \mathbf{r}) = \frac{1}{M^2}\sum_{i,j} \delta_f^i \delta_f^j |\psi_i(\mathbf{r})|^2 |\psi_j(\mathbf{r})|^2 \beta_{ij} \tag{2.27}$$

where β_{ij} is a correction term given as:

$$\beta_{ij} = \frac{1}{\int |\psi_i(r)|^2 |\psi_j(r)|^2 d^3r} \tag{2.28}$$

Next, define a non-negative density function, $\eta_{ij}(\mathbf{r})$:

$$\eta_{ij}(\mathbf{r}) = \beta_{ij} |\psi_i(\mathbf{r})|^2 |\psi_j(\mathbf{r})|^2 \tag{2.29}$$

By definition, $\eta_{ij}(\mathbf{r})$ vanishes for non-overlapping wave functions and modified by β_{ij}, otherwise. Equation 2.27 can then be rewritten as:

$$\bar{\zeta}(\epsilon_f, \mathbf{r}) = \frac{1}{M^2} \sum_{i,j} \eta_{ij}(\mathbf{r}) \delta_f^i \delta_f^j \tag{2.30}$$

In Equation 2.30, the integral of $\bar{\zeta}(\epsilon_f, \mathbf{r})$ over the cell volume provide $N^2(\epsilon_f)$. Each grid point $\mathbf{r}$ represents a localized contribution to N^2, indicating the electronically active pathways in the material.

2.6.3 Normalization of the Spatial Distribution

We first verify the normalization of the pair-density function $\eta_{ij}(\mathbf{r})$. From its definition in Eq. (2.29),

$$\int \eta_{ij}(\mathbf{r})\, d^3r = \beta_{ij} \int |\psi_i(\mathbf{r})|^2 |\psi_j(\mathbf{r})|^2\, d^3r. \tag{2.31}$$

Substituting the definition of the normalization factor β_{ij},

$$\beta_{ij} = \frac{1}{\int |\psi_i(\mathbf{r})|^2 |\psi_j(\mathbf{r})|^2\, d^3r}, \tag{2.32}$$

immediately yields

$$\int \eta_{ij}(\mathbf{r})\, d^3r = 1. \tag{2.33}$$

Thus, each pair of states (i, j) contributes a properly normalized, non-negative spatial distribution.

We now evaluate the volume integral of the spatially projected quantity $\bar{\zeta}(\epsilon_f, \mathbf{r})$ defined in Eq. (2.30):

$$\int \bar{\zeta}(\epsilon_f, \mathbf{r})\, d^3r = \frac{1}{M^2} \sum_{i,j} \delta_f^i \delta_f^j \int \eta_{ij}(\mathbf{r})\, d^3r \tag{2.34}$$

$$= \frac{1}{M^2} \sum_{i,j} \delta_f^i \delta_f^j, \tag{2.35}$$

where the normalization condition $\int \eta_{ij}(\mathbf{r}) d^3r = 1$ has been used. Using the definition of the density of states at the Fermi level from Eq. (2.25)a, we obtain

$$\int \bar{\zeta}(\epsilon_f, \mathbf{r})\, d^3r = \left(\frac{1}{M} \sum_i \delta_f^i \right)^2 = N^2(\epsilon_f). \tag{2.36}$$

This demonstrates explicitly that the modified spatial distribution $\bar{\zeta}(\epsilon_f, \mathbf{r})$ is correctly normalized and that its volume integral recovers $N^2(\epsilon_f)$ exactly. Thus, we tentatively interpret ζ as a spatial probability density for electrical conductivity.

2.6.4 Interpretation of N^2 Estimate for Conductivity

RPA is a dramatic assumption but works well for metals and our composite – materials with extended electronic states at the Fermi level. The electronic states in such systems are extended, and the phases of the electronic states are averaged over the many states near the Fermi level. For localized states at the Fermi level, the RPA is expected to fail, *eg* the off-diagonal contribution in Equation 2.18 might be important. This work also emphasizes that the density of states at the Fermi level is not an approximate surrogate for the conductivity, whereas N^2 is.

A link to other work is noted. An effort of the early nineties was devoted to the study of localized representations of the electronic structure, either through the use of Wannier functions [103], or exploiting the decay in real space of the single-particle density matrix (DM) [63], expressed as:

$$\rho(\mathbf{r}, \mathbf{r}') = 2 \sum_{i\ occ} \psi_i^*(\mathbf{r}) \psi_i(\mathbf{r}') \tag{2.37}$$

where the sum is restricted to the occupied electronic subspace and $\mathbf{r}$ and $\mathbf{r}'$ are points in space, and the system is spin unpolarized. Kohn gave a clear picture of the origin of the decay of the DM (as a function of $|\mathbf{r}\text{-}\mathbf{r}'|$), noting that it was due to quantum mechanical destructive wave interference [63]. This work was motivated partly for computational

advantage, as it led to linear scaling computational demand as a function of system size, but also as basic physics of a material, since it implies a unique decay length of the DM determined by the constituent atoms and the structure of the lattice. Hindley's RPA depends on destructive wave-mechanical interference also, though the details are different than the case of ρ.

The space-projected conductivity leads to an expression for σ reminiscent of the N^2 scheme and the DM. The electrical conductivity is written as a double sum on real space grid points $\mathbf{r}$ and $\mathbf{r}'$ for a Hermitian positive semi-definite matrix Γ,

$$\sigma(\omega) = \sum_{\mathbf{r},\mathbf{r}'} \Gamma(\mathbf{r},\mathbf{r}') \tag{2.38a}$$

$$\Gamma(\mathbf{r},\mathbf{r}') = \sum_{i,j} g_{ij} \left[\xi_{ij}(\mathbf{r})\right] \left[\xi_{ij}(\mathbf{r}')\right]^* \tag{2.38b}$$

$$\xi_{ij}(\mathbf{r}) = \psi_i(\mathbf{r}) \hat{\boldsymbol{p}} \psi_j(\mathbf{r}) \tag{2.38c}$$

$$g_{ij} = \frac{2\pi e^2}{3m^2 \mathrm{V} \omega} \left[f(\epsilon_i) - f(\epsilon_j)\right] \delta\left(\epsilon_j - \epsilon_i - \hbar\omega\right) \tag{2.38d}$$

Here, e, m, V, ω, and f are the electron charge, the electron mass, the system's volume, the external Kubo field frequency, and the Fermi-Dirac distribution, respectively, and $\hat{\boldsymbol{p}}$ is the momentum operator. Note the similarity of the expressions for Γ and ρ. Γ is built from a double sum over the momentum-related objects ξ evaluated at two different points, algebraically similar to the DM. However, the DM is a single sum over all the states below the Fermi level, whereas Γ is built from a small range near the Fermi energy. To the extent that there are many states in the small interval (for example in a metal), one might expect decay in $\Gamma(\mathbf{r},\mathbf{r}')$, for large $|\mathbf{r}-\mathbf{r}'|$ which is presumably related to the validity of the RPA. By examining Δ, the diagonal part of Γ:

$$\Delta(\mathbf{r}) = \Gamma(\mathbf{r},\mathbf{r}) \tag{2.39}$$

The spatial conduction activity given by Δ is usually qualitatively similar to a more intricate analysis using the full Γ.

2.7 Conclusion

In this chapter, a comprehensive theoretical and computational framework for investigating electronic transport in metal–graphene composite systems has been detailed. The formalism integrates first-principles Density Functional Theory, the Kohn–Sham representation of electronic states, the Kubo–Greenwood formulation for electrical conductivity, and the space-projected conductivity (SPC) to enable a quantitative description of charge transport at the atomistic scale. The use of molecular dynamics combined with adiabatic averaging of the Kubo–Greenwood conductivity provides a physically grounded approach to model finite-temperature effects, explicitly accounting for thermally induced lattice disorder and electron–phonon interactions.

Motivated by the need for a more scalable descriptor, a simplified N^2 method was developed based on the Random Phase Approximation (RPA). By invoking phase randomness for extended states near the Fermi level, the DC conductivity is shown to scale approximately with the square of the electronic density of states at the Fermi energy, $N^2(\epsilon_f)$. A properly normalized spatial projection of this quantity was derived, yielding a non-negative real-space distribution whose volume integral recovers $N^2(\epsilon_f)$ exactly. This provides an efficient and physically motivated alternative to full SPC calculations, while retaining meaningful spatial resolution of conduction pathways.

The formal similarity between the conduction matrix $\Gamma(\mathbf{r}, \mathbf{r}')$, the density matrix, and the N^2 spatial distribution highlights the fundamental role of quantum interference and phase cancellation in governing electronic transport. In systems with extended states at the Fermi level, such as metals and metal–graphene composites, the assumptions underlying the RPA appear well justified, whereas strong localization would require a more complete treatment beyond this approximation.

3 Physics of Enhanced Electronic Transport in Metal-Graphene Composites

In this chapter, the intricate physics underlying the origin of enhanced electronic performance of metal-graphene composites is explored. Graphene in its pristine form is introduced into the metal matrix, and its structural and electronic properties are studied. First, we discuss transport properties of single-layer graphene in a copper matrix. Next, single and double layer graphene are introduced in Aluminum and exploring the structural and electronic dynamics at the metal-graphene interfaces. We present the pressure and temperature effects on the electronic performance of these metal-graphene composites.

Associated Publication:

1. K. Subedi, **K. Nepal**, C. Ugwumadu, K. Kappagantula and D. A. Drabold, *Electronic transport in copper graphene composites*, Applied Physics Letters, 122, 031903 (2023).

2. **K. Nepal**. C. Ugwumadu, K. N. Subedi, K. Kappagantula and D. A. Drabold, *Physical origin of enhanced electrical conduction in aluminum-graphene composites*, Applied Physics Letters 124, 091902 (2024).

3.1 Copper-Graphene Composites

We explore the electrical transport properties of the Cu-G composites as a function of the interfacial distance between Cu and graphene, a parameter that can be modulated during Cu-G manufacturing and a simple proxy for a possible strained local configuration. We quantify the electronic transport by computing the electronic conductivity using the Kubo–Greenwood formula (KGF), ideally suited for density-functional simulations of materials with its single particle Kohn–Sham orbitals and energies. We also quantify the charge transport by computing net charges on interfacial Cu atoms and the graphene

using Bader charge analysis [104]. Besides quantifying the conductivity, we determine the conduction-active sites in the Cu-G composites using the space-projected conductivity (SPC).

3.1.1 Computational Details

3.1.1.1 Electronic Structure Calculations. DFT calculations were carried out using the VASP code. For atomic structure relaxations of Cu/Gr/Cu models, we used a plane-wave basis set with a kinetic energy cutoff of 400 eV. For static calculations, we used a larger cutoff of 520 eV. Projected augmented wave (PAW) [105] potentials was used to account for ion-election interactions, and the generalized gradient approximation of Perdew-Burke-Ernzerhof (PBE) [106] as the exchange-correlation functional. The Brillouin zone was sampled using the Monkhorst-Pack scheme with 2×2×1 **k**-point meshes except for computing electronic density of states (EDOS) where denser **k**-point meshes of 4×4×2 were used. The periodic boundary conditions were implemented throughout. To determine the partial occupancy of electrons near the Fermi level, Fermi-Dirac distribution function with a smearing temperature of 1000 K was considered. δ function in the expression of KGF was approximated by a Gaussian distribution function of width 0.05 eV. Factors like thermal broadening, **k**-point sampling, and finite-size effects discussed in references [107–110] play a role in employing the KGF.

3.1.1.2 Interface Models and Simulation of External Pressure. We simulated the Cu-Gr composite by constructing an interface model with a geometry of the form copper/graphene/copper (Cu/Gr/Cu). We adopted one of the low-indexed copper surfaces, namely (111), to construct the Cu surface with a dimension of 10.22 × 13.28 $Å^2$. We placed graphene above the Cu-surface and another copper surface of similar dimension, forming an interface structure, or so-called “sandwich” structure. We started with the ”ideal” structure by placing graphene with one sub-lattice site (A) above the top of the

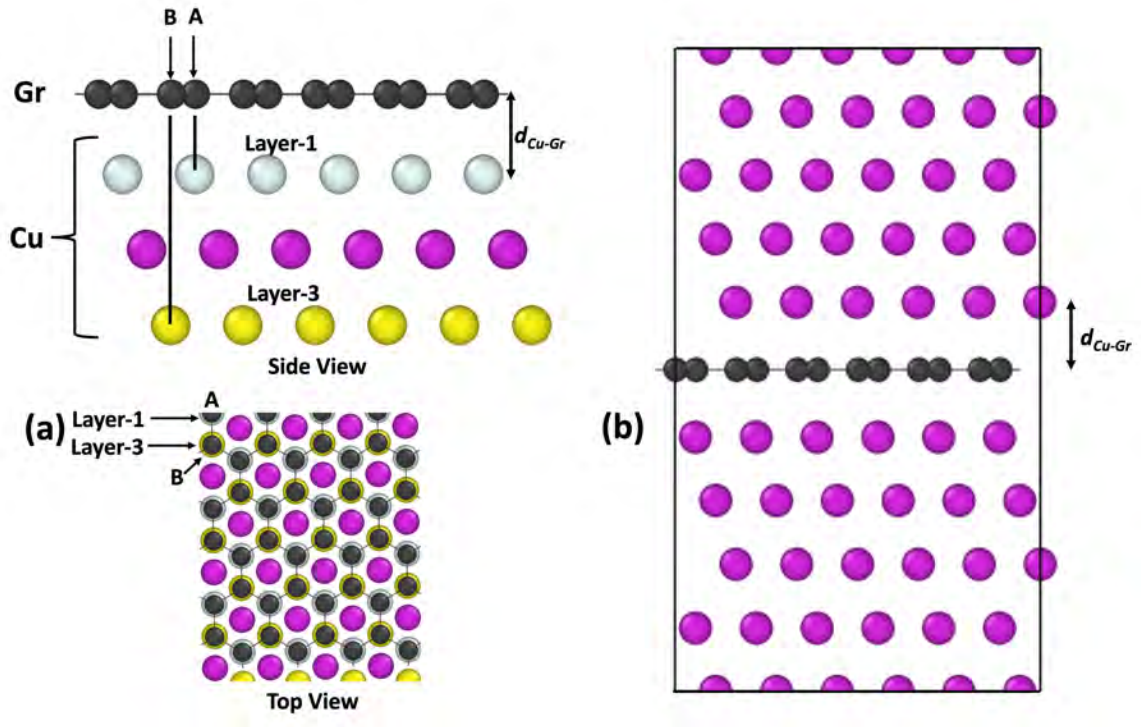

Figure 3.1: (a) Top-fcc configuration of graphene above the Cu 111 surface with A and B representing sub-lattice sites above the Cu atom at first and third layer, respectively. Side and Top views are shown. (b) Geometry of Cu/Gr/Cu model with d_{Cu-Gr} representing Cu-Gr distance. Pink and dark colored spheres represent Cu and C atoms, respectively.

first layer of Cu 111 and the other sub-lattice site (B) placed above the third layer of Cu 111 (refer Figure 3.1 (a)). This arrangement is known as top-fcc, and has been shown to represent the low-energy structure for Cu-Gr surface models [111]. The interface model, shown in Figure 3.2(b) with fcc-top-fcc stacking, was then constructed, which has been shown to represent the low-energy interface models among six different stacking, namely fcc-top-fcc, hcp-top-fcc, top-top-fcc, fcc-top-hcp, hcp-top-hcp, and top-top-hcp [111].

To simulate the pressure effect on the composites, we followed the approach similar to work by Lanzillo [112] to simulate copper and aluminum under external pressure. This is

done by reducing the vertical dimension of the supercell, followed by the atomic structure relaxation. Compression of these models is parameterized by the copper-graphene distance (d_{Cu-Gr}), which undergoes through relaxation process resulting in a distinct interface distance. The parameterized interface distances before and after structural minimization are tabulated in the first and the second column of Table 3.1 respectively. It is apparent that the extent of repulsion of Cu atoms away from the graphene is higher for models with short Cu-Gr distances, indicated by larger shift in Cu-Gr layers (third column of Table 3.1). For long Cu-Gr distances (up to d_{Cu-Gr} = 2.61 Å), most of the Cu-Cu bonds are virtually unaffected and only few Cu-Cu bonds are formed up to ≈2.52 Å, whereas for short Cu-Gr distances, the vertical Cu-Cu bonds are also formed at ≈2.49 and ≈2.46 Å.

d_{Cu-G} (Å) (Initial)	d_{Cu-G} (Å) (Relaxed)	Shift (Å)	P_z [GPa]	d_{Cu-G} (Å) (Initial)	d_{Cu-G} (Å) (Relaxed)	Shift (Å)	P_z[GPa]
3.22	3.25	0.03	1.7	2.20	2.37	0.17	6.5
2.88	2.94	0.06	2.7	2.02	2.29	0.27	10.3
2.71	2.78	0.07	3.2	1.86	2.23	0.37	14.9
2.54	2.61	0.07	3.1	1.69	2.19	0.50	20.2
2.37	2.46	0.09	4.2				

Table 3.1: Variation of Cu-Gr distance for different Cu/Gr/Cu models after atomic structure relaxation and corresponding transverse component of Stress Tensor. d_{Cu-G} corresponds to Cu-Gr distance, and P_z–Transverse component of Stress Tensor.

3.1.2 Electronic and Transport Properties

KGF conductivity for the Cu/Gr/Cu models in the direction normal to the graphene layer (i.e., along c-axis in Fig. 3.1 (a) was computed. Figure 3.2(a) displays conductivities for the models with different Cu-Gr distances normalized by the KGF conductivity of

copper crystal computed at 300 K corresponding to d_{Cu-Cu} = 2.56 Å. From Fig. 3.2(a), we see that the conductivity increases with decreasing Cu-G distance in an almost exponential manner up to d_{Cu-G} = 2.37 Å. Beyond 2.37 Å, there is a sharp rise in conductivity followed by a saturation below ≈2.23 Å. The increase in conductivity may be attributed to increased constructive overlapping of copper and graphene orbitals with decreasing Cu-G distance. For the short Cu-G distances with d_{Cu-G} = 2.23 Å and beyond, the conductivity is obtained to be ≈10% higher compared to that of copper computed at 300 K. To explore such increasing trend in the conductivity, we performed Bader charge analysis to compute net charge on the interfacial Cu atoms and the C atoms of graphene, and is shown in Fig. 3.2(b). From Fig. 3.2(b), we see that the net charge on C atoms increases and the net charge on Cu atoms decreases on interfacial Cu atoms with decreasing Cu-Gr distance. This indicates an increasing charge transfer between interfacial Cu atoms and the graphene with decreasing Cu-G distance.

To further understand the electronic structure of these composites with varying Cu-G distance, we computed total EDOS (TDOS) and the projected EDOS (PDOS) on C atoms for selected models and are shown in Fig. 3.2(c). From Fig. 3.2(c), we find relatively higher EDOS near the Fermi level with decreasing Cu-G distance. Such increase in the EDOS is contributed by both copper and carbon atoms of the Cu-G composites, which are more pronounced for short Cu-G distances. The Fermi level also gets shifted towards the conduction band with decreasing Cu-G distance that allows more electronic states to participate for conduction. According to Mott and Davis [95, 113], the DC conductivity, $\sigma_{dc} \propto (N(\epsilon_f))^2$, where N represents the density of states. So, one expects enhancement of conductivity at short Cu-G distances for these composites as a combined effect of enhanced EDOS near the Fermi level. We note that it was not at all obvious that the graphene would enhance the EDOS at the Fermi level, and we conjecture that this is what underlies experiments showing improved conductivity of the composites.

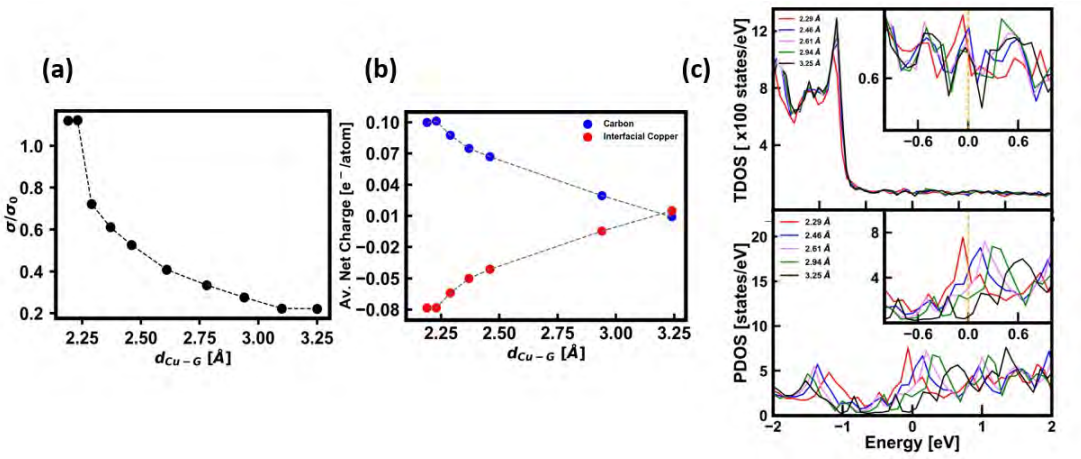

Figure 3.2: (a) KGF conductivities for relaxed Cu/Gr/Cu models with different Cu-G distance normalized by the KGF conductivity (σ_0) of a copper crystal computed at 300K with d_{Cu-Cu} = 2.56 Å. (b) Net charge per atom on interfacial copper atoms (solid red circles) and carbon atoms of graphene (solid blue circles). The dashed lines in subplots (a) and (b) are guides to the eye. (c) Electronic density of states for different Cu/G/Cu models computed at $4 \times 4 \times 2$ **k**-point meshes. The top subplot corresponds to the total EDOS (TDOS), and the bottom subplot corresponds to the projected EDOS (PDOS) onto carbon. The compression of models resulted in an enhanced EDOS near the Fermi level; see the inset for details.

Further exploration was made by investigating a spatial description of conductivity as a function of Cu-Gr distance. We computed the SPC for selected Cu/G/Cu models and are shown in Fig. 3.3. Figure 3.3 displays the SPC projected on 100 plane as a RGB colormap for four such models with different Cu-G distance. The colorbar on the left depicts the magnitude of SPC values, where red color represents low SPC values and blue color represents high SPC values. From Fig. 3.3, it is apparent that the contribution from both Cu and graphene to the conduction increases with decreasing Cu-G distance, and is

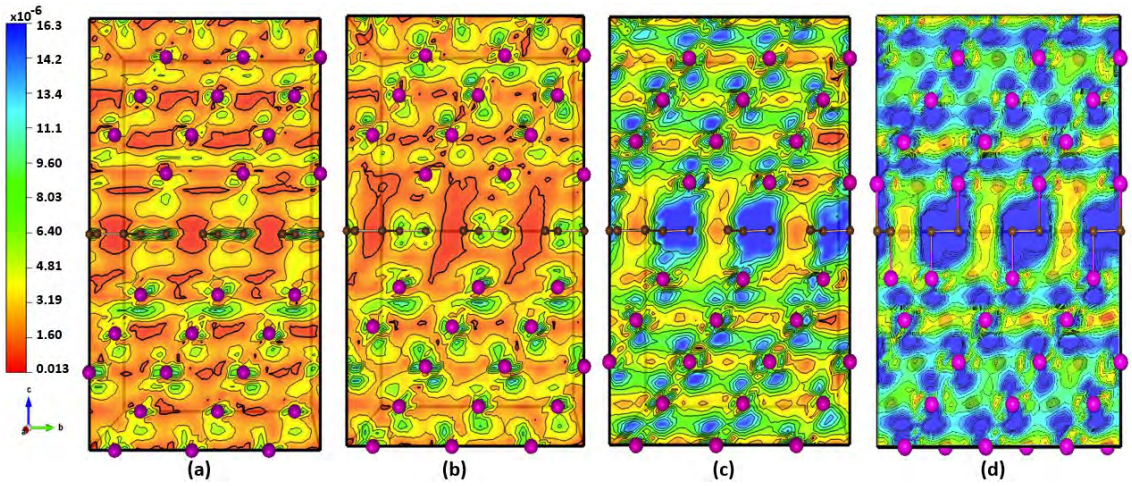

Figure 3.3: Space-projected conductivity plotted as an RGB colormap along a plane normal to the graphene for different Cu/G/Cu models corresponding to d_{Cu-G} = 3.25 Å, 2.94 Å, 2.29 Å, and 2.23 Å, respectively. The colorbar on the left represents the magnitude of SPC values that increases from red towards blue. The SPC values are scaled from the minimum value for d_{Cu-G} = 3.25 Å. Cu and C atoms are represented by pink and brown-colored spheres, respectively.

more significant at short distances. The SPC plots at short Cu-G distances show that the graphene directly participates in conduction and forms a bridge for conduction between Cu atoms on opposite layers. In addition to the graphene, we also see significant contributions from Cu atoms to conduction at short Cu-G distances. This contribution from Cu atoms to the conductivity can be associated with different Cu bonding environments in the Cu-Gr composites.

KGF conductivity for the orthorhombic Cu model for different vertical Cu-Cu distances ranging from 2.43 to 2.55 Å were calculated, and is shown in Fig. 3.4. From Fig. 3.4(a), we see that the conductivity of Cu increases with reducing Cu-Cu distance from ≈2.55 to ≈2.46 Å after which it drops at ≈2.44 Å. We observed that for short Cu-Gr

distances ($d_{Cu-Gr} \leq 2.23$ Å), the Cu-Cu bond lengths are also formed at ≈2.49 and ≈2.46 Å, see Figure 3.4(b). So, the contribution to the conductivity from the Cu atoms with the nearest neighbors close to 2.46 and 2.49 Å is higher compared with Cu atoms at other distances and, in agreement with SPC plots in Fig. 3.3.

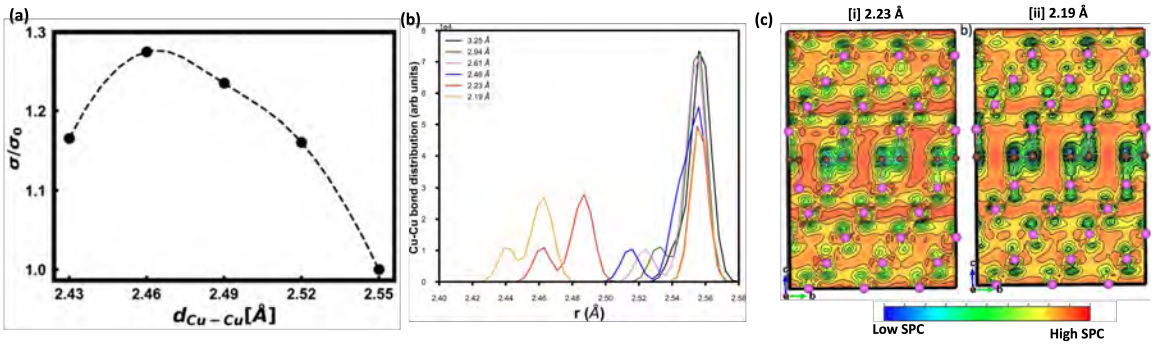

Figure 3.4: (a)Relative conductivity (σ/σ_0) of orthorhombic Cu model computed as a function of vertical Cu-Cu bond length normalized by the KGF conductivity (σ_0) of a copper crystal computed at 300K with d_{Cu-Cu} = 2.56 Å. The dashed line is a guide to the eye.

Saturation in conductivity of Cu/G/Cu model for compression below d_{Cu-G} = 2.23 Å (refer Fig. 3.2(a)) was observed. Such a characteristic is attributed to the contribution of the Cu atoms forming different nearest-neighbor distances. At d_{Cu-G} = 2.23 Å, the repulsion of Cu layers on both sides of graphene leads to formation of Cu-Cu bonds at ≈2.49 and ≈2.46 Å. With further reduction of Cu-G distance, here d_{Cu-G} = 2.19 Å, the Cu-Cu bonds are formed at ≈ 2.46 Å and also at ≈2.44 Å. So, the additional disorder in Cu leads to slightly less contribution from the Cu atoms to the conduction (refer Fig. 3.4) even as the graphene still contributes. The spc plots for d_{Cu-G} = 2.23 Å and d_{Cu-G} = 2.19 Å, shown in Figure 3.4(c), show a similar distribution of SPCs, depicting the saturation in electronic conductivity at these interface distances.

3.1.3 Conclusion

In this work, we investigated Cu/Gr/Cu composites with varying Cu–Gr interfacial distances and demonstrated that decreasing this distance enhances DC conductivity, primarily due to increased electronic density of states near the Fermi level and greater charge transfer between interfacial Cu atoms and graphene. Spatially resolved conductivity (SPC) calculations revealed that graphene actively bridges conduction between Cu atoms, especially at shorter distances. Interestingly, conductivity saturates below a Cu–Gr spacing of 2.23 Å, attributed to reduced Cu contribution from Cu–Cu bond formation around 2.44 Å, despite graphene's continued role. These findings highlight that graphene can participate in, rather than hinder, conduction when interface conditions are optimized, suggesting that processing strategies that control interfacial structure can significantly influence composite performance. While this study focused on dependency of e;ectronic conductivity with the interfacial distance, subsequent chapters will explore other factors such as grain orientation, atomic geometry at interfaces, multi-layer graphene, and defect density in graphene.

3.2 Aluminum-Graphene Composites

This study extends the analysis of the physical origin of enhanced electrical performance of metal-graphene composites by studying aluminum-graphene composites formed with single and double-layer graphene. While experimentally extruded aluminum-graphene composites consist of multiple graphene layers, this study focuses on single and double layers of graphene in interface models, providing key details into the broader comprehension of the remarkable behavior of aluminum-graphene composites. We offer atomistic insights into the electronic consequence of structural relaxation at the aluminum-graphene interface and explore the temperature-dependent conductivity with the number of graphene layers in the composites. Interface models of aluminum-graphene are simulated,

and hereafter, models of Aluminum - single-layer graphene - Aluminum composites are referred to as SL, and Aluminum - double-layer graphene - Aluminum composite is referred to as DL.

3.2.1 Computational Protocols

To create the Al-Gr composite models, we started with an orthorhombic cell of face-centered Al (111) that includes a stacking fault, as shown in Figure 3.5 (a). Single and double (”AB” stacking) graphene sheets were positioned above the aluminum fault layer to form an interface. The side view of the arrangement of the atoms in the SL and DL models is shown in Figures 3.5 (b) and 3.5 (c), respectively. To represent the thermophysical phenomena typically observed in solid-phase processed Al-G composites, we simulated the ”compression” of the composites by reducing the Al-G distance. Next, employing the conjugate gradient algorithm within the VASP, an energy-optimized interface structure of the composite was attained for several constant volume simulations. The compression and relaxation procedures employed in this paper are designed to mimic conditions commonly observed in aluminum composites that exhibit improved electrical conductivity through solid-phase processing methods. For geometry optimization using conjugate gradient in VASP (maximum residual force is less than 0.01 eV/Å), we used a kinetic energy cutoff of 420 eV. For single-point calculations, we used an energy cutoff of 480 eV. The Projected augmented wave (PAW) potential described the ion–election interactions, and the generalized gradient approximation (GGA) of Perdew–Burke–Ernzerhof (PBE) was implemented for the exchange-correlation functional [65, 106]. The Brillouin zone was sampled using the Monkhorst-Pack [114] scheme with a $2 \times 2 \times 1$ k-point mesh. For completeness, we implemented Grimme’s van der Waals (D2) correction [115] for the interfacial structure. However, post-relaxation, there was no notable disparity observed in the presence of the correction.

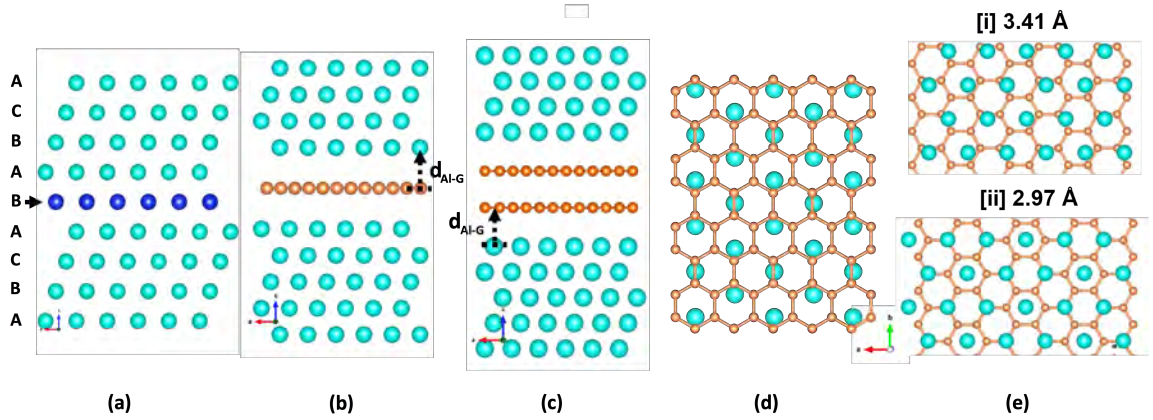

Figure 3.5: (a) ABCABC... planar stacking in the Al (111) face-centered structure with a fault layer, shown by blue atoms. Representative structure of interface models with (b) single-layer and (c) double-layer graphene, where d_{Al-G} is the distance between the aluminum surface and the graphene layer. (d) Top view of the arrangement of carbon atoms in the graphene layer with Al (111) for a weakly interacting Al-graphene system with the interfacial distance of 3.48 Å (before relaxation). (e) Interface structure in composite models after the relaxation of DL composites with [i] d_{Al-G} = 3.41 and [ii] 2.97 Å. For d_{Al-G} = 2.97 Å, the optimized interface structure forms a strain-free registry between Al and C. All cyan (brown) spheres represent Al (C) atoms.

3.2.1.1 Simulation Protocol for Temperature-Dependent Conductivity Calculations. To perform the temperature-dependent conductivity calculations, selected models were equilibrated in a canonical ensemble for a temperature range between 100 K to 600 K, in steps of 50 K [116]. The temperature was maintained using the Nosé-Hoover thermostat, and all atomic species were allowed to thermally fluctuate. The simulations were conducted for 3 ps with a timestep of 1.5 fs. For the subsequent conductivity calculations, we selected the last 10 configurations separated by intervals of 50 fs for each temperature considered. At temperatures below the Debye temperature, classical MD is not justified,

Single Gr layer			**Double Gr layer**		
d_{Al-G} [Å] initial	d_{Al-G} [Å] final	P [kB]	d_{Al-G} [Å] initial	d_{Al-G} Å final	P [kB]
3.48	3.40	0.27	3.48	3.41	1.15
3.42	3.35	3.42	3.42	3.35	2.77
3.36	3.31	8.41	3.36	3.31	6.25
3.31	3.25	16.82	3.30	3.24	9.72
3.28	3.13	20.09	3.24	3.19	14.35
3.21	3.01	27.29	3.18	3.11	17.50
3.16	2.90	36.68	3.12	3.07	22.66
3.09	2.71	69.76	3.06	3.01	27.64
			3.00	2.97	31.88
			2.96	2.94	34.69
			2.92	2.87	53.69

Table 3.2: Summary of variation in the interfacial distance for different Al-Gr models after atomic structure relaxation and corresponding external pressure. The left and right correspond to aluminum-graphene composites with single and double graphene layer, respectively. The average Al-Gr interfacial distance after conjugate gradient relaxation is reported. P is an external pressure computed for the compressed models within VASP.

as lattice quantization should be considered; however, while the dynamics are unrealistic it appears that the naive classical sampling yields sensible results when employed with KGF, as we demonstrated and discussed in detail earlier and discussed in detail [116].

3.2.1.2 Pressure-Relaxed Al-G Composite Models. To impose compression onto the system, the vertical dimension of the composite model was reduced, followed by a structural relaxation. For each compression followed by relaxation, the initial and final interfacial distances were noted and are listed in Table 3.2, along with the external pressure on relaxed models computed within VASP. The final interfacial distance is an average distance between the interface aluminum and graphene layers with a standard average error less than $1e^{-4}$ Å. Table 3.2 left and right correspond to SL and DL composites. The graphene layer formed on either side was a similar configuration with the interfacial Al layers after relaxation.

Visual inspection of the composite models before any compression and structural optimization, as shown in Figure 3.5 (d), shows the misalignment between Al and C atoms as a honeycomb lattice of graphene (lattice constant of 2.46 Å) has a lattice mismatch of $\approx$ 5% with the face-centered Al (111) surface nearest-neighbor distance of 2.34 Å. However, after compression of the models followed by structural optimization (via energy minimization), there appears to be an alignment between the Al and C atoms. Figures 3.5 (e) ([i] and [ii]), corresponding to models with d_{Al-G} = 3.41 Å and 2.97 Å respectively, show that the extent of atomic alignments between C and Al depends on the extent of compression. The self-organized interface configuration for the compressed model (d_{Al-G} = 2.97 Å in this work) is one of the low-energy Al-Gr interface structures, so-called strain-free registry [117–119].

3.2.2 Electronic and Transport Properties

We computed the atom-projected electronic density of states (PDoS) for varying interfacial distance models. The PDoS for the SL and DL composite models are shown in Figure 3.6 (a) and 3.6 (b), respectively. The focus is on the region near the Fermi energy (ϵ_f), indicated by the gray dashed lines and shifted to zero. As the distance between

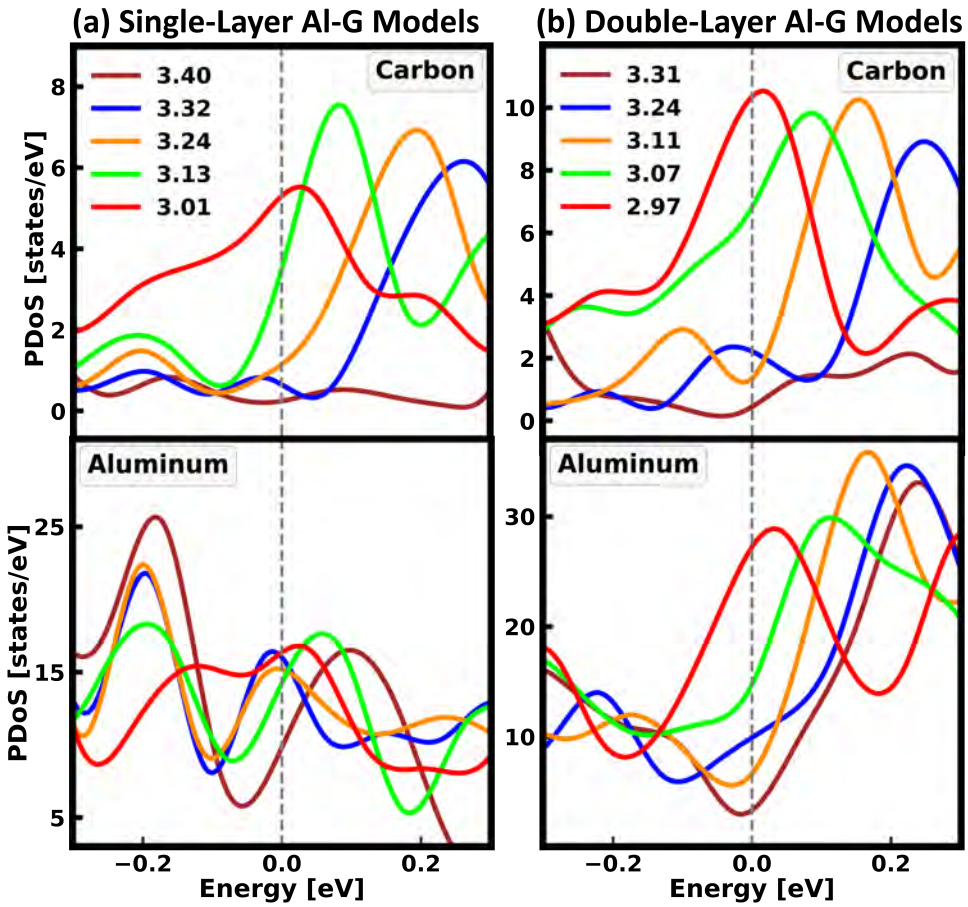

Figure 3.6: Projected electron density of states (PDoS) on carbon and aluminum atoms for (a) SL and (b) DL composites. The Fermi level is shifted to zero and is shown by the gray vertical dashed line in each subplot.

aluminum and graphene (Al-G distance) decreased, we observed an enhancement of the electronic density of states near the Fermi level from both carbon (TOP) and aluminum (BOTTOM) atoms. With a random phase approximation [91–94], Mott and Davis showed that the electronic conductivity is proportional to $N^2(\epsilon_f)$ [102], $N(\epsilon_f)$ being the density of states at the Fermi energy (ϵ_f). To explore this further, we plotted the behavior of $N^2(\epsilon_f)$ for the compressed composite models (brown curve in Figure 3.7 (a). Indeed,

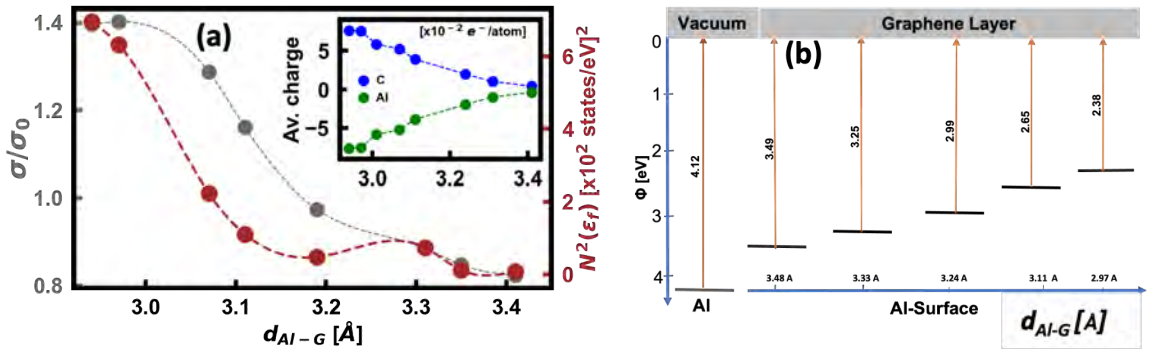

Figure 3.7: (a) Conductivity for the DL model for various Al-G distances (d_{Al-G}) in the x-axis). The average conductivity (σ) is represented by the gray curve, with σ_0 denoting the conductivity of the Al-matrix shown in Figure 3.5 (a) calculated at 300 K. The squared density of states at the Fermi level is shown in brown. In the inset, a Bader analysis [2] illustrates the average charge gain and loss for C (blue) and Al (green) atoms. (b) Estimated energy (Φ) required to remove an electron from a pure Al surface with a graphene layer placed on it at different interfacial distances. Dotted lines are included in all plots as visual aids.

$N^2(\epsilon_f)$ roughly tracks the electronic conductivity (σ) calculated using the Kubo-Greenwood formula, shown by the gray curve in Figure 3.7 (a). As the Al-G distance decreases, both $N^2(\epsilon_f)$ and electronic conductivity increase, consistent with the elementary notion that metallicity/conduction are associated with a large $N(\epsilon_f)$. The DL composites (d_{Al-G} = 2.97 Å and 2.94 Å) exhibit approximately 40% higher conductivity relative to the aluminum matrix at 300 K. These results qualitatively agree with the results reported for the copper-graphene interface [77, 120]. Next, we depicted a flattening in the electrical conductivity for the compression beyond 2.97 Å, detailed below. Analogous results for the SL models can be found in Figure 3.8.

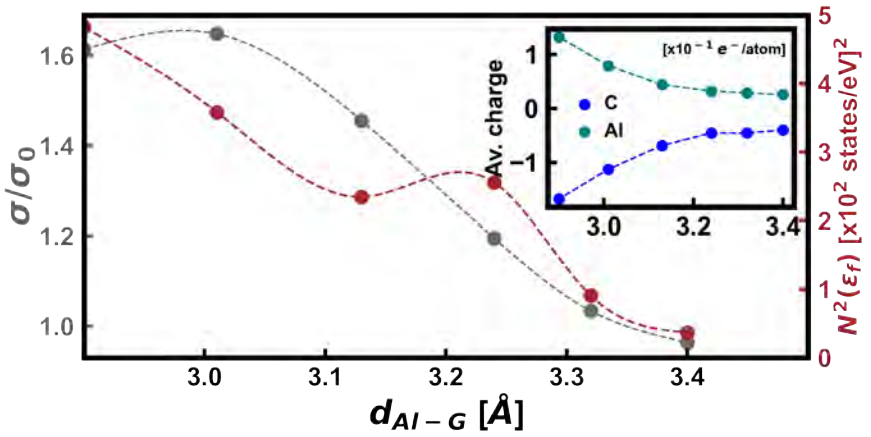

Figure 3.8: All plots correspond to the SL model for the different Al-G distances (d_{Al-G}) on the x-axis. The conductivity of the relaxed SL models is represented by the gray curve, with σ_0 denoting the conductivity of the Al-matrix calculated at 300 K. The squared density of states at the Fermi level is shown in brown. In the inset, Bader analysis illustrates the average charge gain and loss for C (blue) and Al (green) atoms. Dotted lines are included in all plots as visual aids.

To provide salient background information on the electrical conductivity, the conductivity in orthorhombic face-centered (111) aluminum was analyzed as a function of the Al-Al bond length (refer to Figure 3.9). Electrical conductivity in aluminum increases with decreasing Al-Al bond length (d_{Al-Al}) until ≈ 2.76 Å. Beyond this threshold, a decrease in conductivity is observed. In DL composites with d_{Al-G} = 2.97 Å and 2.94 Å, the mean Al-Al bond length was d_{Al-Al} = 2.76 Å, corresponding to the d_{Al-Al} with the highest electrical conductivity, as depicted in Figure S2. Further compression in the composite, resulting in d_{Al-G} < 2.94 Å exhibited a decrease in electrical conductivity. This trend is consistent with observations in copper-graphene heterostructures [77, 120].

The Fermi level shifts towards higher energies with decreasing Al-G distance, allowing more electronic states to participate in conduction (see details in Table 3.3). We

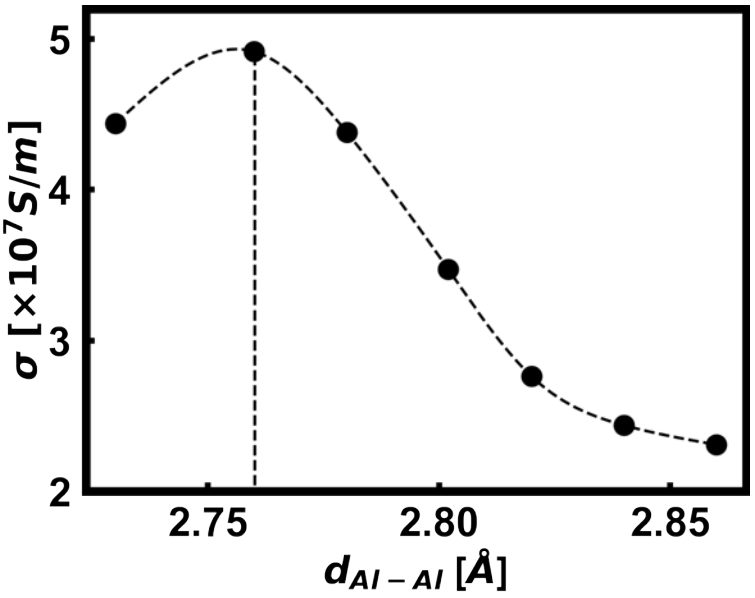

Figure 3.9: Electrical conductivity (σ) of an orthorhombic face-centered (111) aluminum as a function of Al-Al bond length. The vertical line at ≈ 2.76 Å marks the turning point in conductivity, consistent with the non-monotonous trend in conductivity with pressure.

further predicted the work function of the composites for varying Al-G distances which is shown in Figure 3.7 (b). The plot shows that the work function decreases with decreasing Al-G distance and hints at increasing charge transfer between interfacial graphene and aluminum atoms. These effects are quantified by estimating the average charge transfer from interfacial Al to C atoms, shown in the inset of Figure 3.7 (a). At the shortest interfacial distance (d_{Al-G} = 2.97 Å), the average transfer of electronic charge to graphene reached 0.075 electrons per atom.

Next, we computed the conduction path in real space and its Al-G distance dependence. To achieve this, we employed the space-projected conductivity (SPC) method to project the electronic conductivity onto real-space grids. The upper panel of Figure 3.10 shows the isosurface plots of the transverse SPC values for DL composite models with interfacial distances of 3.41 Å and 2.97 Å, represented by (a) and (b) in Figure

3.10, respectively. The color bar on the right indicates the magnitude of SPC values, with red (blue) indicating low (high) values. At short Al-G distances, both aluminum and graphene contribute to conduction, particularly at the Al-G interface. The SPC at short Al-G distances reveals that graphene actively participates in conduction and forms a bridge between Al atoms on opposite layers. Notably, Figure 3.10 (upper panel) illustrates the formation of a continuous network of graphene sheets within the aluminum matrix, establishing a pathway for electron transport.

To further delineate the enhanced electron transport through the Al-G interface, we computed the electronic charge density near the Fermi level. By decomposing 15 bands above and below the Fermi level from the total electron charge density, we generated isosurface plots, shown in the lower panel of Figure 3.10. The same models used for the SPC calculation were employed. In the model with d_{Al-G} = 2.97 Å, a higher degree of interaction between graphene and interfacial aluminum atoms was observed, indicated by the presence of black and red regions in the isosurface plot.

Next, we investigated the temperature dependence of conductivity in the composite models. This was done by estimating the average electrical conductivity from KGF for models held at different temperatures. Figure 3.11 presents the average electronic

Table 3.3: Fermi level as a function of Al-G composites for varying aluminum-graphene interfacial distance. The first and second rows correspond to DL and SL composites, respectively.

d_{Al-G} **[Å]**	3.41	3.35	3.31	3.24	3.19	3.11	3.07	2.97	2.94
E_f **[eV]**	6.70	6.79	6.93	7.05	7.20	7.29	7.36	7.52	7.63
d_{Al-G} **[Å]**	3.40	3.35	3.31	3.25	3.13	3.01	2.90	2.71	
E_f **[eV]**	6.78	7.07	7.34	7.62	7.87	8.18	8.43	8.67	

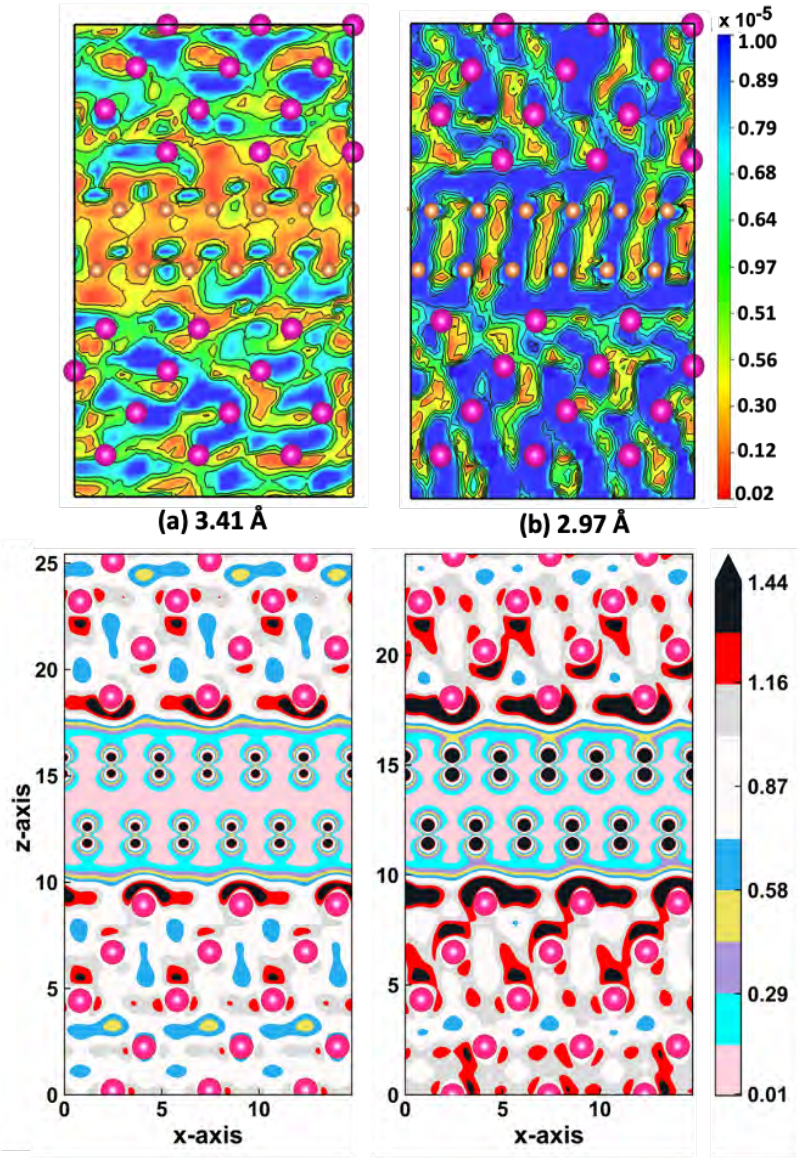

Figure 3.10: [TOP] Projected 2D transverse SPC [in Siemens/cm/Å^3] iso-surface plot. [BOTTOM] Band decomposed charge density [in e^-/Å^3] corresponds to 15 bands below and above the Fermi level. The charge density values were scaled by a factor of 100. The data presented is for DL models with d_{Al-G} = (a) 3.41 Å, (b) 2.97 Å. The pink (brown) spheres represent the Al (C) atoms in the models.

conductivity, obtained from 10 uncorrelated snapshots, as a function of temperature, ranging from 100 K to 600 K. Figure 3.11 (a) shows the conductivity behavior for the DL models corresponding to two interfacial distances. The model with d_{Al-G} = 3.41 Å exhibits a nearly linear relationship, shown by blue plots. However, the model with short Al-G distance, d_{Al-G} = 2.97 Å (shown by red plots), displays local extrema at around 300 K (minima) and 400 K (maxima). This non-monotonic behavior is in accord with experimental observations of conductivity enhancement in solid-phase processed metal-graphene composites [11, 12], suggesting that this work captures, to some extent, the physics of the real material. In contrast, the extrema are not observed in the SL composite models, as shown in Figure 3.11 (b) and 3.11 (c) which correspond to Al-G distances d_{Al-G} = 3.01 Å and 3.40 Å respectively. The non-monotonic temperature dependence observed exclusively in the compressed DL composites can be attributed to two factors: (1) The active involvement of graphene layers in charge transfer at shorter Al-G distances and (2) thermally driven hopping across the inter-layer galleries between the compressed graphene double-layer [121–124].

3.2.3 Conclusion

We show that graphene and graphene stacks enhance the electronic conductivity of Al and while a key addition to the area, it is not the full story. The graphene structures are dispersed in an unknown way throughout the metal microstructures in the experimentally synthesized bulk composites and conspire to create a globally enhanced conductivity and globally modified temperature dependence. These effects could be due to (1) reduced scattering at grain boundaries from the graphene or (2) forming a network of isolated or weakly interacting Al-Gr structures. Our work complements both of these imaginings. The registry between the sp^2 carbon network (see Figure 3.5e [ii]) and the Al (111) surface

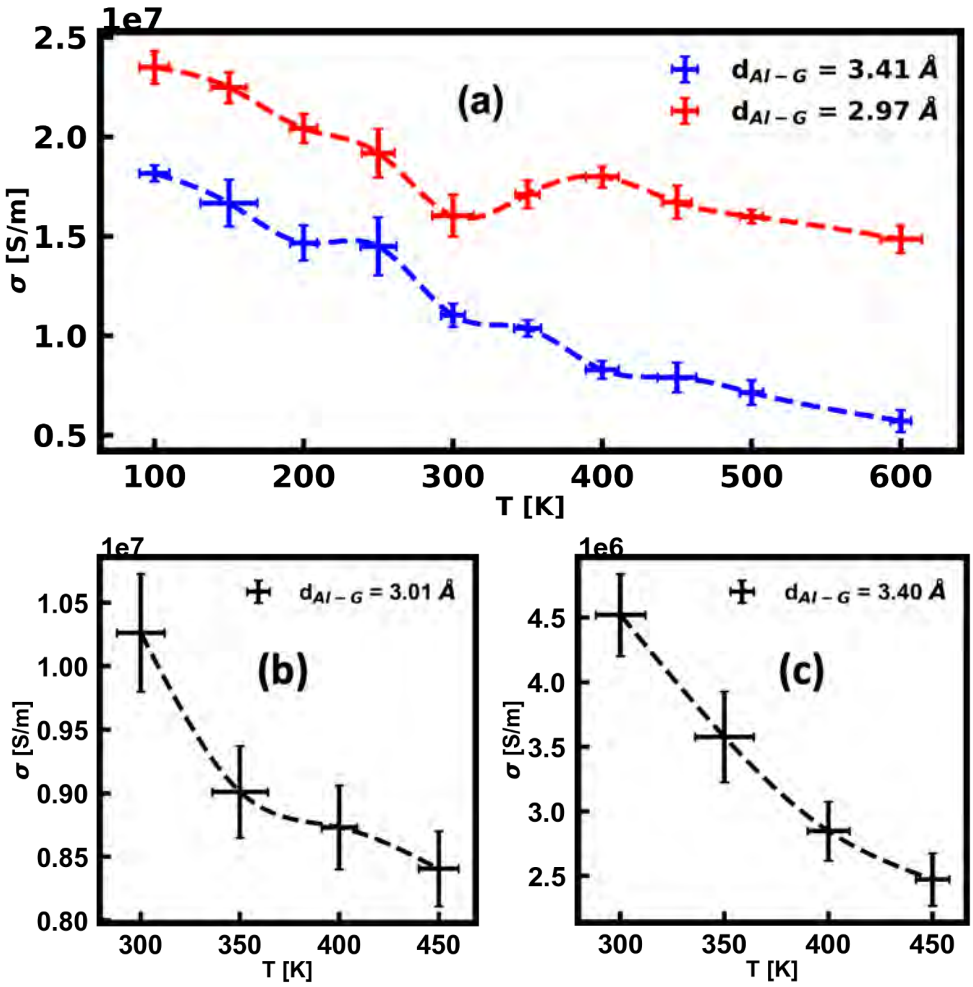

Figure 3.11: (a) Average electronic conductivity plotted versus annealing temperature for DL composite models with Al-G distances of 2.97 Å (red) and 3.41 Å (blue). (b) and (c) Similar plots for SL composite models, with Al-G distances of 3.01 Å and 3.40 Å, respectively. Vertical bars represent the standard deviation from the mean conductivity, averaged from the last 10 snapshots taken at 50 fs intervals over 3 ps annealing. Horizontal bars represent temperature fluctuations during constant temperature annealing.

suggests that mechanism (1) may be a key player in conductivity enhancement, as we demonstrate that a self-organized grain boundary buffer may form at Al (111) surfaces.

This study provided a comprehensive atomic-level understanding of the role of graphene as an additive in aluminum grains, focusing on single- and double-graphene stack(s) in the aluminum matrix. We demonstrated that the increased electrical conductivity observed in Al-graphene composites arises from the enhanced electronic dynamics at the Fermi level. The interaction between carbon and interfacial aluminum atoms highlights the active role of graphene in facilitating electronic conduction. Furthermore, our study depicts the experimentally observed enhanced electrical conductivity within the temperature range of 300 K to 400 K.

The increased conductivity observed in these new metal/carbon composites defies traditional principles to understand the conductivity in metals, such as Matthiessen's rule, which posits that electrical conductivity decreases with metal imperfection. Experiments support that this phenomenon exists, and this chapter provides a detailed physical explanation for the mechanism. This chapter shows that the enhanced conductivity is attributed to two guiding principles: (1) the establishment of an interfacial coverage by graphene sheet(s) serving as a conduit for electron transport across metal grains, and (2) enhanced electronic density of states at the Fermi level. Note that the ideal geometries with pristine graphene and metal matrices are considered in this chapter. The role of alloy disorder, functional impurities, and topological disorders in the electronic performances of metal-carbon composites is detailed in subsequent chapters.

4 Crystal Orientation, Topological Disorders and Common-Coal Impurities Effects on Electronic Conductivity of Metal-Carbon Composites

Associated Publications

1. **K. Nepal**, C. Ugwumadu, A. Gautam, K. Kappagantula, and D. A. Drabold, Electronic conductivity in metal-graphene composites: the role of disordered carbon structures, defects and impurities, J. Phys. Materials 7 025003 (2024)

2. **K. Nepal**, C. Ugwumadu, F. Kraft, Y. Al-Majali and D. A. Drabold, The effects of crystal orientation and common coal impurities on electronic conductivity in copper-carbon composites, Carbon 231 119711 (2025)

The outcomes of the preceding chapter showed that the addition of single- or multi-layered graphene sheet(s) to metals like aluminum (Al) and copper (Cu) produces unconventional electrical wires with enhanced electronic conduction. Two pertinent questions arise: (1) How does this phenomenon manifest in metals other than copper and aluminum? (2) To what extent must the layered carbon material's purity and crystallinity be maintained to attain these improvements? The second question is addressed in this chapter. The question highlights the practical challenges associated with large-scale graphene production. The process of graphite exfoliation frequently results in defective graphene, while the synthesis of high-quality graphene is often limited to small quantities through methods such as chemical vapor deposition [29, 30]. On the other hand, ultra-fast Joule heating offers the potential for generating more substantial quantities [125, 126], but the method still grapples with cost and high energy consumption issues. Even the "crystalline" CVD graphene procured commercially is never completely crystalline. At best, it has crystalline domains with amorphous sections that are considered grain boundaries.

Despite the presence of amorphous regions in graphene, various studies on metal-graphene composites have primarily focused on the interfacial properties of crystalline graphene [31–42]. This work takes a novel approach by modeling the metal/amorphous-graphene interface to fully describe metal/graphene behavior, broadening our understanding beyond crystalline domains.

4.1 Effect of Topological Disorder in Aluminum-Amorphous Graphene (Al-aGr) Composites

Amorphous graphene (aGr) is a topologically disordered carbon structure that exhibits distinct and intriguing structural, mechanical, and electronic characteristics, perhaps enabling innovative material design and technological advancements [43–49]. The aGr layer used in this work is derived from amorphous graphite [50]. Details on the simulation/formation of different layered amorphous carbon structures can be found in References [51–53]. In this work, the potential of aGr to ameliorate scattering at grain boundaries is studied. This chapter reveals reduced scattering at grain boundaries dressed by graphene, exhibiting how aGr integrates effectively into the interface. Additionally, the implications of incorporating nitrogen into both crystalline and amorphous graphene within a metal-graphene interface were examined. Previous studies incorporating nitrogen into hexagonal graphene have shown the existence of material with unique electronic properties for diverse applications [127–129]. With the emergence of amorphous carbon structures, a detailed investigation of nitrogen-added amorphous carbon material holds significant interest [130–132].

4.1.1 Models and Methods

The interface design for the aluminum-carbon composite in this work naturally evolved from earlier calculations discussed in References [77] and [133]. In what follows, metal-graphene composite with crystalline graphene is defined as Al-Gr composites, and

that with amorphous graphene as Al-aGr composites. A *"sandwich"* structure of Al-aGr composites was constructed by stacking a layer of aGr (see representative structure in Figure 4.1 (a)) between two (111) terminations of Al, as depicted in Figure 4.1 (b). Aluminum (111) was chosen due to its low surface energy compared to other crystallographic orientations [134, 135]. The models were relaxed at constant volume to a configuration with minimal energy, corresponding to an average interface distance of $\approx$ 2.94 Å. Next, we modeled the Al-Gr composites with geometrical dimensions similar to those of Al-aGr composites. For a relaxed Al-aGr interface structure, C atoms in the aGr layer lack an atomic alignment/registry with interfacial Al atoms that contrasts with a low-energy interface registry observed in Al-Gr composites; the latter one is discussed in detail in Reference [136].

First-principles calculations were conducted using the VASP code. The electron-ion interactions were described using the projector augmented wave (PAW) method [105], and the exchange-correlation functional was based on the generalized gradient approximation (GGA) of Perdew–Burke–Ernzerhof (PBE) [106]. A kinetic energy cutoff of 420 eV for relaxation and a larger cutoff of 540 eV was used for electronic properties calculations, and the system's total energy convergence accuracy was set at 1.0×10^{-6} eV/atom. The Brillouin zone was sampled using a $2 \times 2 \times 1$ Monkhorst–Pack $\boldsymbol{k}$-mesh for structural relaxation, electronic conductivity and space projected conductivity calculations, whereas for the density of states calculation, a finer $4 \times 4 \times 2$ $\boldsymbol{k}$-mesh grid was used. Periodic boundary conditions were implemented throughout. The Fermi-Dirac distribution function in the KGF used a smearing temperature of 1000 K. The δ function in the expression of KGF was approximated by a Gaussian distribution function of width 0.02 eV. References [107–110] provide a detailed discussion of various approximations inherent in the KGF formulation, such as Gaussian width, the number of atoms, smearing temperature, and energy cutoff for finite-size cells.

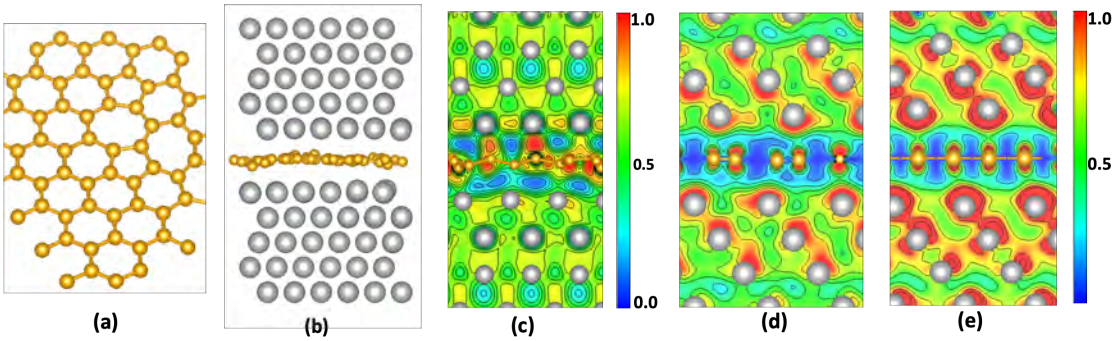

Figure 4.1: (a) A typical configuration of aGr with topological disorder (non-hexagonal carbon rings). (b) The geometry of the Al-aGr interface model. (c) 2-dimensional contour plot of electron localization function depicting mixed interfacial bonding character in the interfacial region in Al-aGr composite. Contour plot of charge density computed for twenty bands symmetrically chosen around the Fermi level for (d) Al-aGr composite and (e) Al-Gr composites along the plane transverse to the graphene. The charge density is normalized with the maximum value for the Al-Gr composite. Gold and light gray spheres are carbon and Al atoms.

4.1.2 Results and Discussions

4.1.2.1 Al-aGr Composites. To examine the electronic dynamics at the interface region, the energy required for an electron in aluminum to surmount the potential barrier from the interface gallery to the aGr plane was calculated, yielding an energy of $\approx$ 2.97 eV. A structure representing the Al-Gr interface was constructed in a similar aluminum and carbon environment to facilitate a qualitative comparison. For this case, the computed energy barrier for the Al-Gr interface was $\approx$ 2.38 eV. The Al-aGr interface exhibited a higher energy barrier, likely stemming from a misaligned interface registry and the intrinsic topological disorder in the structure of the aluminum (111) surface and carbon.

Next, the analysis of the interfacial bonding character was carried out using the electron localization function (ELF, call it χ). χ values typically span the range from 0 to 1, with 1 indicating a covalent bond, 0.5 corresponding to a metallic bond, and 0 being undefined, as defined in [137]. Figure 4.1(c) displays contour plots of χ across (100) planes, with χ values of 1, 0.5, and 0 colored in red, yellow-green and blue, respectively. χ for the composite reveals a mixed bonding character at the interface, with both metallic and covalent bond characteristics between aluminum and carbon atoms. This suggests that the interface bonding properties depend on the relative positions (interfacial configuration) of Al and C, the finding consistent with References [31, 138].

The electronic charge distribution in the composite was analyzed from the charge density for twenty bands chosen around the Fermi level. The charge density plot along the (010) plane is shown in Figure 4.1(d) for the Al-aGr interface model, where the charge density increases from blue to red color. A similar calculation was done for the Al-Gr system as shown in Figure 4.1 (e). While an interaction between the electron gas of the interfacial aluminum and the π orbitals of sp^2 carbon atoms is observed for Al-aGr, it is weak compared to that of the Al-Gr system. The Al-Gr system showed relatively greater electron dynamics at the interface, attributed to the low-energy interfacial configuration, detailed in Reference [136]. Nevertheless, observations from the electron localization function and charge density indicate that the incorporation of aGr aligned with aluminum grains may enhance electronic dynamics.

The electronic density of states for the Al-aGr composites was computed and compared to Al-Gr composites containing hexagonal graphene, as well as graphene featuring di- and tri-vacancy defects, referred to as Al-Gr-DV and Al-Gr-TV, respectively. The total density of states (TDoS; green plot) for the four categories are shown in Figure 4.2. The Fermi level, indicated by the vertical drop line, has been shifted to zero. The

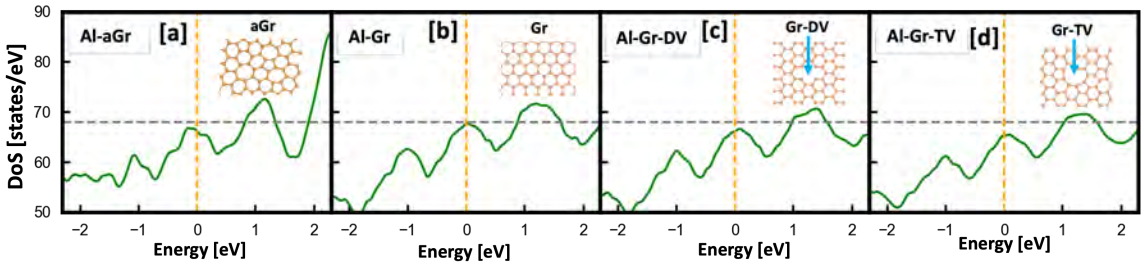

Figure 4.2: Total electronic density of states (green plots) for (a) Al-aGr composites, (b) Al-Gr composite, (c) Al-Gr composites with di-vacant graphene sheet, and (d) Al-Gr composite with a tri-vacant graphene sheet. All inset shows a representative graphene structure in each of the composites. The Fermi level is shifted to E = 0, indicated by a vertical drop line. The horizontal line, drawn in TDoS, serves as a guide for comparing electronic states at the Fermi level.

magnitude of total DoS at the Fermi level goes as Al-Gr > Al-aGr > Al-Gr-DV > Al-Gr-TV.

In line with the conventional understanding of conductivity associated with states at the Fermi level, the decrease in electronic density states correlates with a reduction in electrical conductivity (σ). As argued by Mott and Davis from a random phase approximation [91–94], the dc conductivity involves a product of the squared density of states (N_ϵ^2) and an average of the squared momentum matrix elements over all energy states at the Fermi level ($\epsilon = \epsilon_f$), as discussed in detail in [102]. The conductivity computed for each Al-graphene interface model is shown in the bar graph presented in Figure 4.3(a) (left axis), tracks the variation as $N_{\epsilon_f}^2$, which is shown in the right axis, depicted by red bars. For the Al-aGr composite, the average conductivity computed using the KGF formalism is $\approx 2 \times 10^7$ Siemens/m, which is $\approx 40\%$ of the average electrical conductivity of ideal graphene Al-Gr composites. This decrease in conductivity is expected due to the reduced transport response through the topologically disordered graphene [50]. However,

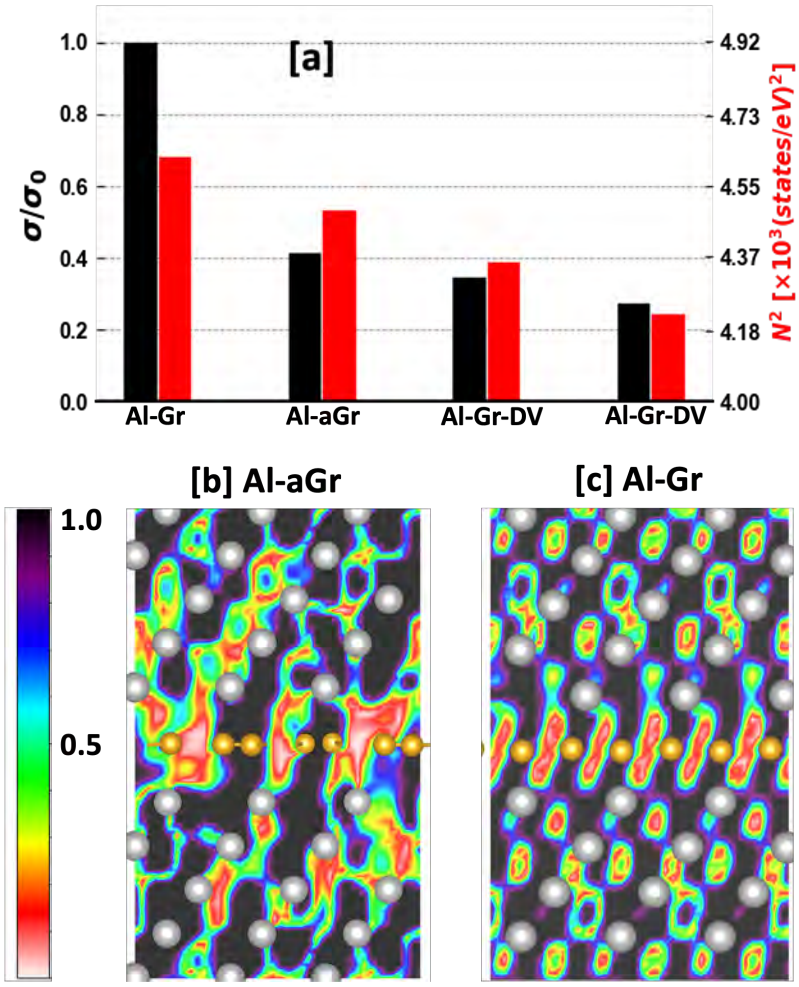

Figure 4.3: (a) Average KGF Conductivities (σ) for Al-aGr and Al-Gr with perfect and defective graphene, normalized by the conductivity ($\sigma_0 \approx 6 \times 10^7$ siemens/m) of perfect Al-Gr composite, shown on left axis by black bars. The right axis with a red bar depicts the squared density of states at the Fermi level for different composites (see text). Two-dimensional normalized space-projected conductivity as a heat map computed along the transverse direction (the direction normal to the plane of the graphene layer) for (b) Al-aGr and (c) Al-Gr composites. The SPC is normalized with the maximum value for the Al-Gr composite. Grey (gold) spheres represent the aluminum (carbon) atoms.

the electrical conductivity of the Al-aGr composite is approximately 17% higher than Al-Gr-DV and 34% higher than Al-Gr-TV composites, respectively. This suggests that while deviation from a hexagonal graphene structure results in reduced electrical conductivity, the topological disorder is less detrimental than a vacancy defect in a layered carbon structure providing insights to aGr as an alternative to realistic graphene metal composites that possess topological defects. This study is of course not exhaustive, owing to the variation of defects in the real interface.

To obtain a visual understanding of conductivity in Al-aGr, transverse SPC (ζ) was computed. A two-dimensional isosurface plot for a plane along (010) is shown in Figure 4.3 (b). The ζ is normalized such that the dark region depicts high ζ values or highly favorable conduction pathways, while the reddish-light region depicts low ζ regions. The formation of a mixed bonding environment at the interface results in graphene forming a weaker connecting link between the two Al grains on opposite sides. To make a qualitative comparison, Figure 4.3 (c) corresponding to Al-Gr composites is presented, depicting continuous conduction across graphene. In line with charge density analysis, the lack of structural alignment in Al-aGr hinders efficient transport, only facilitating partially as depicted in Figure 4.3 (b) by mixed colored regions at the interface.

4.1.2.2 Al-aGr With Impurities. Recent work to investigate the chemical process of graphitization involving coal-like composition (carbon and nitrogen, oxygen, sulfur impurities), showed that nitrogen forms a planar sp^2 ring substitutionally with carbon atoms at low nitrogen concentration (carbon layer formed is amorphous) [53]. This makes the investigation of materials with nitrogen-added amorphous graphene timely, as the world is pushing toward an alternative to graphitic material for applications. In this section, the effect of nitrogen impurities on the transport properties of Al-aGr composites is studied by substituting nitrogen into the carbon atom in the aGr layer. The model is then optimized to a

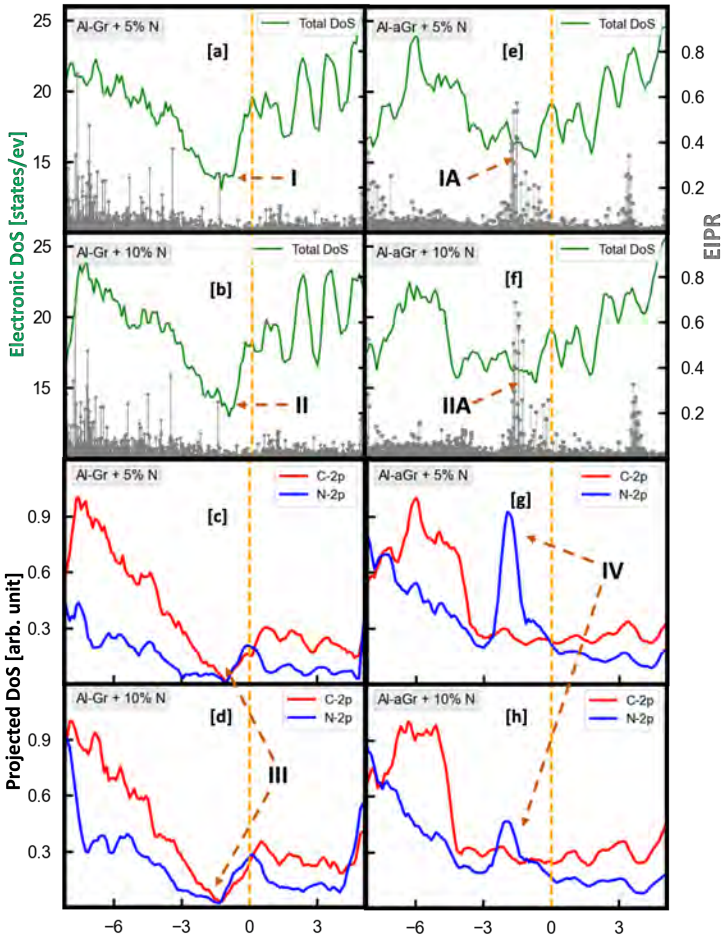

Figure 4.4: Total density of states (TDoS) is shown as green plots, and the projected density of states (PDoS) onto valence 2p of nitrogen (N) and carbon (C) are shown by red and blue plots, respectively. TDoS for Al-Gr system with (a) ≈ 5 % (b) ≈ 10% of nitrogen impurity in graphene. (c) and (d) shows PDoS for ≈ 5 % and ≈ 10% nitrogen for Al-Gr systems. TDoS for Al-aGr system with (e) ≈ 5 % (f) ≈ 10% nitrogen by weight in amorphous graphene. (g) and (h) represents PDoS for ≈ 5 % and ≈ 10% nitrogen in Al-aGr systems. The Fermi level is set at zero, shown by vertical drop lines. Energies of particular interest [I-IV] are discussed in the text. The Electronic Inverse Participation Ratio (EIPR) for impurity models is shown on the right axis in Figures (a), (b), (e), and (f) shown by grey droplines.

low-energy configuration. Subsequently, the transport properties of the resulting composite system are examined.

Two impurity models with ≈ 5% and ≈ 10% nitrogen by weight in aGr were simulated. To make a qualitative analysis of the conductivity of these systems, Al-Gr composites with the same impurity concentrations in graphene were also studied. For both impurity concentrations, the electronic density of states was analyzed, and hence the conduction behaviors.

The total electronic density of states for composites with different impurity concentrations is shown in Figure 4.4. The green plots represent the total density of states, while the red and blue plots signify the density of states projected into the valence 2p orbital of carbon (C) and nitrogen (N) atoms, respectively. Subplots (a) and (b) respectively depict the TDoS for ≈ 5 % and ≈ 10% nitrogen impurity in the Al-Gr composites, while subplots (e) and (f) respectively depict for Al-aGr models. In hexagonal carbon rings, the addition of nitrogen introduces excess electrons [139, 140]. Consequently, the Fermi level is shifted up, shown in the left column in Figure 4.4. Notice a minimum in TDoS in subplots 4.4 (a) and (b) labeled by I and II as an effect of the semi-conducting behavior of graphene. Carbon sp^2 planar rings are characterized by a prominent DoS minimum, which is depicted in Figures 4.4 (c) and (d) labeled III by projecting the DoS onto the valence 2p orbital of carbon atoms. In contrast, a distinguishing feature in TDoS of Al-aGr composites compared to their crystalline counterpart is the filling of the minimum in DoS that was observed in Al-Gr just below the Fermi level. This is shown in Figures 4.4 (e) and (f). The observed electronic effect is due to the effect of odd rings in amorphous graphene, leading to an increase in the density of states near the Fermi level. Despite the modified DoS, the nitrogen addition effect in the Al-aGr interface showed an upward shift in the Fermi level similar to the Al-Gr interface. The vertical drop lines in Figures 4.4 (e) and (f) denote the shifted Fermi level upon N addition in aGr, initially identified in regions labeled IA and IIA.

Also, PDoS onto 2p orbital of nitrogen atoms is shown by blue plots in Figure 4.4. For the case of Al-Gr, PDoS onto nitrogen shows a distinct peak at the Fermi level in par with the peak in PDoS onto carbon atoms, shown in Figures 4.4(c) and (d). For nitrogen in aGr within the composite, PDoS is characterized by an unusual peak in the energy range of -2.5 eV to -1.5 eV, labeled IV in Figures 4.4 (g) and (h). These observations potentially signify unique interactions or electronic configurations within Al-aGr composite material with trace nitrogen concentrations.

To determine the electrical consequence of nitrogen in composites, average electronic conductivities were estimated. We observe that with $\approx$ 5% and $\approx$ 10% nitrogen concentration in aGr, the conductivity of Al-aGr was reduced by $\approx$ 7% and $\approx$ 12 % respectively, as compared to impurity-free Al-aGr composites. Nex,t with the same impurity concentrations for Al-Gr, the reduction in conductivities was $\approx$ 7.5% and $\approx$ 20 % compared to Al-Gr composites. The reduction in conductivities with increasing nitrogen additives is due to the introduction of localized states near the Fermi level capable of capturing and trapping charge carriers (electrons) as they move through the material, hindering their mobility and reducing the overall conductivity [53, 141]. The effect was more pronounced for Al-aGr than Al-Gr composites as observed in Figure 4.4 (e) and (f) (right axis), characterized by high electronic inverse participation ratio (EIPR) near the Fermi level. The EIPR measures the extent of localization of Kohn-Sham states. High (low) EIPR values indicate a localized (extended) Kohn-Sham state. Further insight for such reduction from SPC analysis indicated that nitrogen atoms disrupt the electronic transport in the layered structure [53].

4.1.3 Conclusions

In summary, this work is one of the first demonstrations of the incorporation of amorphous graphene (aGr) to engineer metal-graphene composites and study their

interfacial transport properties through *ab initio* analysis. With enhanced electronic properties observed in different aluminum-crystalline graphene composites, this work highlights the potential of the inclusion of aGr in metal. This work revealed a mixed bonding character at the interface and demonstrated that aGr enables electrical conduction partially, as evidenced by spatial projections of electrical conductivity. This provides insight into effective material processing for achieving desired interface strengths. Next, with the addition of nitrogen into aGr, the average electrical conductivity of composites is hindered. This suggests that introducing nitrogen into these interfaces has the potential to create distinctive routes for electronic conduction. These findings provide atomistic insight into the role of disordered carbon structures, like aGr, as an important alternate material to ameliorate scattering at the metal grains, as well as its integration into sought-after metal-carbon composite materials. For completeness, we note that the present work explores only a few configuration-specific aluminum surfaces and specific models of aGr; as such, the results should be viewed as qualitative. Nevertheless, this work points the way to a more complete understanding of the remarkable behavior of metal-carbon composites.

4.2 Electronic Conductivity of Copper-Graphene Composites With Crystal Orientation and Common-Coal Functional Impurities

Enhancing the electronic conductivity of face-centered cubic (FCC) metals, such as copper, is a significant area of research in materials physics and engineering. Any performance improvements are valuable given copper's critical role in power transmission and distribution, motors, and generators. Traditional alloying methods using additives like silver, niobium, and silicon carbide [142–144] can enhance copper's mechanical properties but often compromise its electronic conductivity. However, recent advancements in incorporating graphene additives into copper matrices have shown promise in developing copper-graphene composites with improved electronic conductivity [41, 42, 145–149].

There is a growing body of work involving computer simulations using molecular dynamics (MD) and density-functional theory (DFT) to explain atomic-level interaction in metal-graphene composites [41, 42, 145, 147, 148]. These studies describe the formation and properties of metal-graphene nanostructures but do not provide atomistically detailed information about electronic activity in the composites. Using the Kubo-Greenwood formula (KGF) for electronic conductivity and the Space-Projected Conductivity (SPC) method, the electronic conduction activity has been spatially resolved in copper-graphene [77] and aluminum-graphene [83]. Identifying conductive regions can assist in the development of materials for other applications such as conducting bridge random access memory (CBRAM), physical unclonable function (PUF) devices, and other systems where atomistic insights into charge transport are essential [85, 86, 88, 89]. Some other ways to identify conductive regions are used: the $q_i - q_j$ method based upon overlapping wavefunctions [85], and an approach based on the Kohn-Sham charge density evaluated at the Fermi level. [90].

4.2.1 Sandwich Structures of Copper-Carbon Composites

Interfacial models of copper-graphene composites were constructed as ”sandwich” geometries as illustrated in Figure 4.5 (a), where a layer of graphene was inserted into different low-energy crystallographic orientations of copper: (100), (110), and (111). The sandwich structure maximizes interface contact, ensuring optimal interaction at the interface (properties at the interface significantly impact the overall conductivity of the system [41, 42, 145, 146, 150]). Figure 4.5 (b) [i-iii] depicts the atomic misalignment between carbon and copper atoms at the interface for different composites. The carbon atoms in a honeycomb lattice of graphene (lattice constant of 2.46 Å) have a lattice mismatch of $\approx 4\%$ with (111) copper crystal (hexagonal lattice parameter of 2.56 Å). The lattice mismatch with the rectangular (110) copper lattice (lattice parameters of 2.56

Table 4.1: Structural and electronic parameters in copper-graphene composites post relaxation and DFT calculation. P = transverse component of the stress tensor. d_{Cu-G} = average interface distance between copper and graphene layer after relaxation. Φ = work function: energy required to remove an electron from the copper surface. $\triangle q$ = net charge transfer to carbon atoms from interface copper atoms.

gray!30	**Cu-Gr (100)**		**Cu-Gr (110)**			**Cu-Gr (111)**					
gray!10 P gray!5 [GPa]	d_{Cu-G} [Å]	Φ^a [eV]	$\triangle q$ [eV/atom]	P [GPa]	d_{Cu-G} [Å]	Φ^a [eV]	$\triangle q$ [eV/atom]	P [GPa]	d_{Cu-G} [Å]	Φ^a [eV]	$\triangle q$ [eV/atom]
0.00 [b]	3.40	3.75	0.01	0.00 [b]	3.39	3.70	0.01	0.00 [b]	3.20	3.50	0.02
3.00	3.03	2.85	0.01	2.71	2.97	2.68	0.01	1.50	2.67	2.49	0.05
7.50	2.70	2.15	0.03	4.53	2.51	1.93	0.03	5.60	2.36	1.00	0.08
10.5	2.52	1.89	0.03	8.50	2.40	1.52	0.04	8.40	2.32	0.95	0.09

[a] The pure copper work-functions (Φ) for (100), (110), and (111) are 4.53, 4.25, and 4.57 eV, respectively.

[b] The equilibrium configuration of the models with no vertical compression

Å and 3.62 Å) is $\approx$ 4% and $\approx$ 47% respectively. The interface between (100) and sp^2 carbon has the most significant lattice mismatch with $\approx$ 47% ((100) is a square lattice with a lattice parameter of 3.62 Å). These models were relaxed under finite compression to form an interface. The simulated compression pushes the materials into a high-energy state with special properties and perhaps mimics the external pressure exerted on the composites during solid-phase extrusion [10–12]. It should be noted that the compressed models in this work aim to represent realistic microstructures, which differ from the ideal geometries typically used to study interface transport properties in composites. The vertical compression (P) on the models and their associated interfacial distances (d_{Cu-G}) are summarized in Table 4.1.

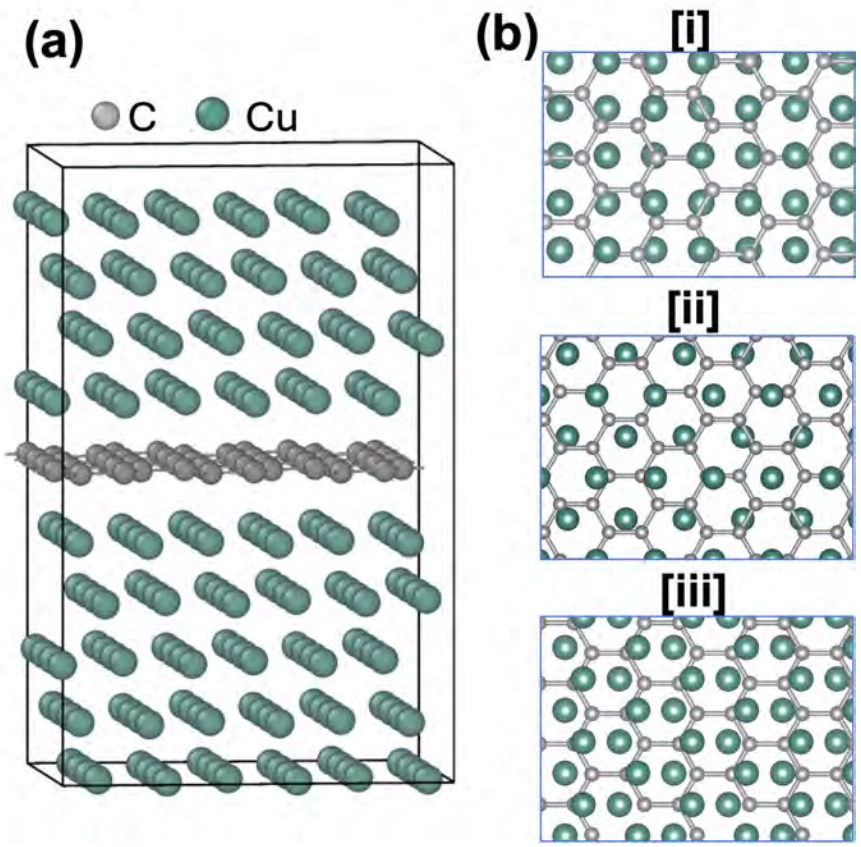

Figure 4.5: (a) A typical sandwich configuration of the copper-graphene interface model. (b) [i, ii, iii] depict a top view of the interface showing the arrangement of carbon atoms and copper (100), (110), and (111) grain, respectively. Green and grey spheres represent copper (Cu) and carbon (C) atoms, respectively.

Geometric relaxation for the models was implemented with the conjugate gradient approach implemented within `VASP`. To account for Van der Waals contributions, Grimme's D2 correction was employed during the relaxation. The structural relaxation and the electronic calculations were conducted using a plane-wave basis set with a kinetic energy cutoff of 420 eV and 520 eV, respectively, and the self-consistent loop tolerance of 10^{-6} eV was considered for energy convergence. The projected augmented wave (PAW) potentials

[105] was utilized for ion-electron interactions, and the generalized gradient approximation of Perdew-Burke-Ernzerhof (PBE) [106] was used as the exchange-correlation functional. The Brillouin zone was sampled using the Monkhorst-Pack scheme [114] with a 2×2×1 **k**-point mesh for geometrical relation and electronic conductivity calculations, while a finer 4×4×2 **k**-point mesh was used for the density of states calculations. Periodic boundary conditions were implemented throughout that models an infinite graphene sheet sandwiched between a copper matrix along the planar direction, and the graphene sheet is repeated along the transverse direction for 20 – 25 Å. Electronic conductivity was calculated using the KGF, following the protocols outlined in Reference [77].

4.2.2 Results and Discussions

To check the proposed quadratic relationship between the full Kubo-Greenwood electronic conductivity and the density of states at the Fermi level, detailed in Chapter 2, the electronic properties of sandwich models constructed with (100), (110), and (111) copper grains are examined. An increase in electronic conductivity with compression was observed for all the configurations (see Figure 4.6). The improvement in electronic conductivity in Figure 4.6 (a) directly correlates with the squared electronic density of states at the Fermi level, $N^2(\epsilon_f)$, in Figure 4.6 (b). This validates the argument that the conductivity scales as $N^2(\epsilon_f)$ and not linearly as $N(\epsilon_f)$, as intuitively defined from KGF and utilized by Watanabe *et al.* in Reference [90] and in Reference [151]. To provide additional evidence that the scaling of electronic conductivity is not linear, spatially decomposed $N(\epsilon_f)$ is also presented.

Electronic conduction in copper-graphene composites reveals a strong dependence on the crystallographic orientation of copper, with the (111) orientation exhibiting the highest conductivity, followed by (110) and then (100) grains. To study this dependence, the relaxation effects on these composites are explored. Figure 4.11 (a), (b), and (c) present

the ”top view” of the self-organized interface structures for (100), (110), and (111) copper orientations, respectively, after energy optimization, starting from the configurations shown in Figure 4.5 (b). While no periodic atomic alignment between carbon atoms and (100) copper atoms is observed, the interface atoms in (110) and (111) crystal orientations form near-perfect registries, creating continuous networks. These networks, termed the ”bridge” (110) and ”top-fcc” (111) registries, see Figure 4.11 (b) and (c) respectively, represent low-energy, highly favorable geometries for electron transport in metal-carbon composites.

To investigate the influence of the copper-carbon interfacial configuration on the electronic transport properties of the composites, work functions (ϕ) for the composites at different compression levels are computed, summarized in Table 4.1. At equilibrium (no vertical compression at the copper-graphene interface), the (100) orientation exhibited the highest work function, followed by the (110) and (111) surfaces. This suggests that electrons from (111) copper are the most likely to transfer to the graphene layer. Reduced work functions were observed in all composites as the interface distance decreased. The extent of this reduction depends on the copper orientation within the composites, as detailed in Table 4.1. A decreasing work function indicates more efficient electron transfer from the copper surface to carbon atoms. This efficiency in electron transfer is quantified by computing the net charge transfer ($\triangle q$) to carbon atoms using Bader charge analysis [2]. The Bader charge for composites with varying interface distances is summarized in Table 4.1. A significant charge transfer of approximately 0.1 e^-/atom for the (111) interface at shorter interface distances is observed, compared to 0.04 e^-/atom and 0.03 e^-/atom for the (110) and (100) composites, respectively.

In the study by Gwalani *et al.*, transmission electron microscopy (TEM) analysis reveals a predominant coherence of graphene flakes with the (110) copper grains and a reduced grain boundary density in copper-graphene composites compared to pure copper, contributing to the enhanced electronic conductivity. Our findings indicate that the (111)

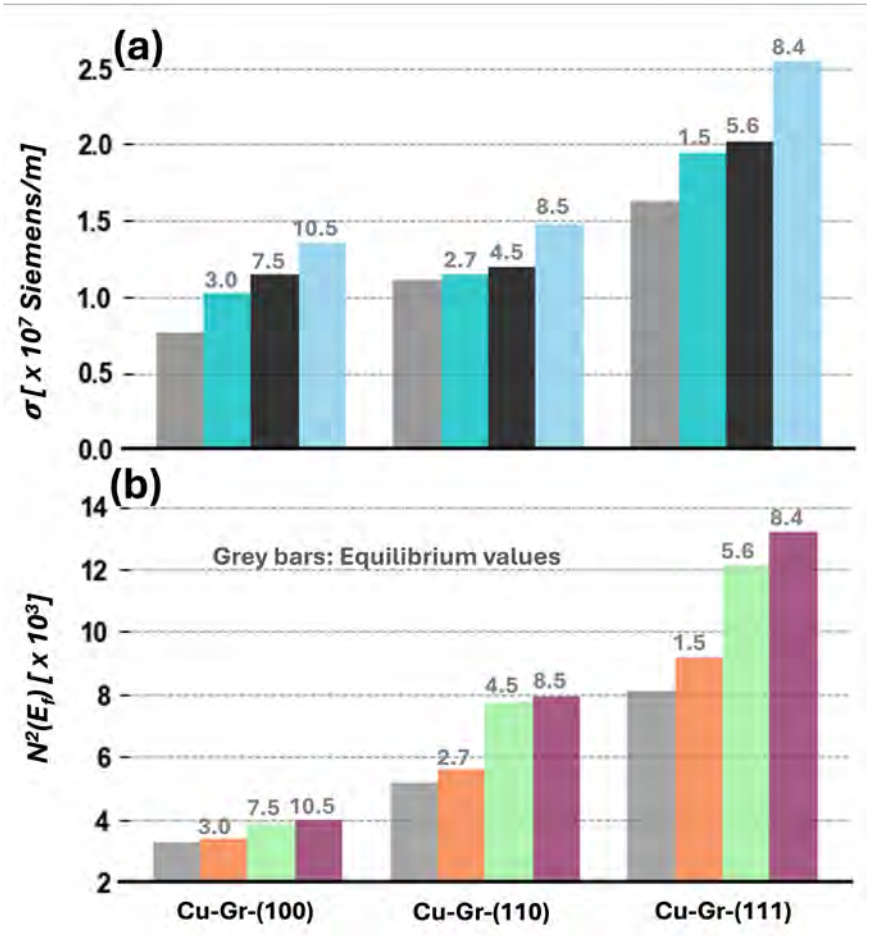

Figure 4.6: Electronic Conductivity (σ) and Squared Electronic Density at Fermi level $N^2(\epsilon_f)$ in copper-graphene-copper composites. (a) Displays σ for copper grains oriented along (100), (110), and (111) at different compression values (written at the top of each bar in GPa). (b) Shows $N^2(\epsilon_f)$ for the same orientations and compressions.

orientation forms a commensurate registry with graphene, potentially dressing the grains. Additionally, the observed low-energy registry of the (110) orientation may improve the coherent alignment of copper (110) with graphene. Such coherence and commensurate registry likely facilitate enhanced electronic coupling, thereby improving global electrical conductivity.

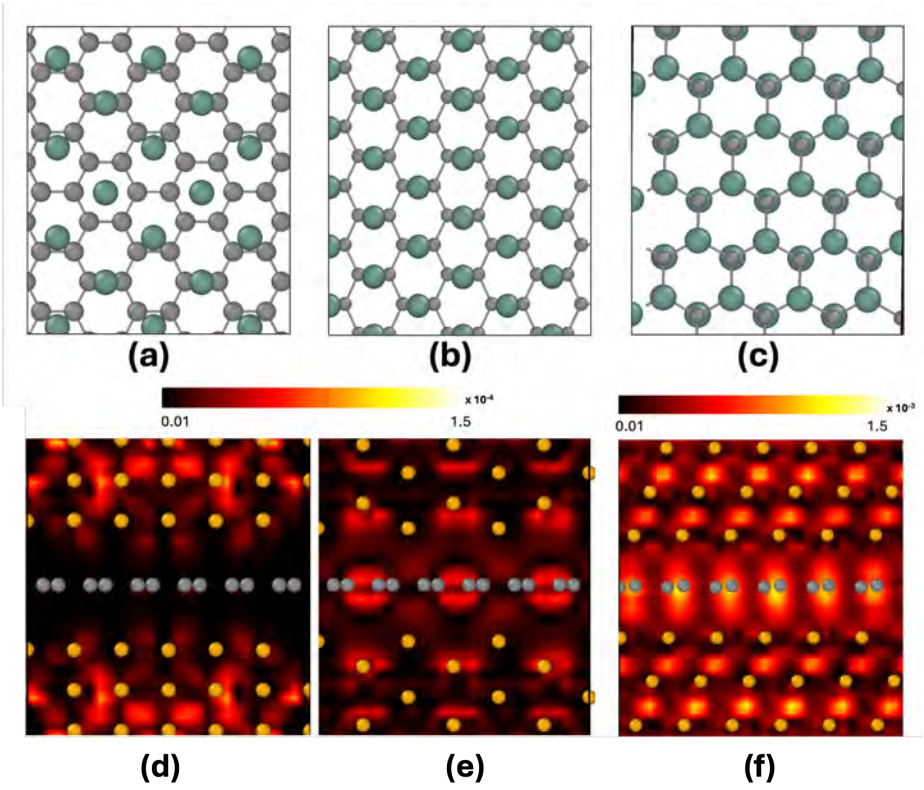

Figure 4.7: (a-c) depicts the top view of composite interfaces after structural relaxation, with copper grains oriented along (100), (110), and (111), respectively. Note the remarkable metal and carbon atoms registry on the (111) orientation. The side view of these interfaces, shown in (d-f), depicts space-projected conductivity as a heat map showing the conduction active region at the copper-graphene interface. Figure (d-f) corresponds to the interface of graphene with (111), (110), and (100) copper grains, respectively. SPC Values are scaled by the maximum value in the (111) copper composite. (d-f) correspond to composites with copper oriented along (100), (110), and (111) directions, respectively. The color bar represents the intensity of electronically favorable pathways, ranging from blue (low intensity) to red (high intensity).. Color Nomenclature: Brown: copper, grey: carbon.

For completeness, generalizing the reported electronic properties at elevated temperatures is not obvious and requires further investigation. Nepal *et al.* [83] showed that aluminum-multilayer graphene composites exhibit enhanced conductivity under compression at high temperatures, consistent with the results for solid-phase extruded composite samples [12]. This enhancement is likely due to improved interlayer contact, reduced potential barriers, and hopping between localized states driven by lattice motion at T > 0, as discussed in References [152], [153], and [154], as well as by Mott and Davis in Reference [155].

4.2.3 Impurities and Electronic Conduction in Copper-Graphene Composites

Following the work by Ugwumadu *et al.* [53, 156] where carbonization and graphitization of coal-like compositions were studied, it is known that nitrogen (N) tends to form a sp^2 structure with carbon (graphitic-nitrogen) while oxygen (O) and sulfur (S) form an ether bridge: C–O–C and C–S–C, respectively. Based on this, interface models incorporating such carbon structures into the copper matrix are created. Specifically, models with nitrogen (5% and 10% by weight), models with oxygen (5% and 10% by weight), a model with nitrogen and oxygen (10% by weight), and a model with nitrogen, oxygen and sulfur (15% by weight) in graphene sheets are developed. These interface models are relaxed to form a low-energy configuration. Here, the interfaces with (111) copper grains are exclusively focused on.

With 5% and 10% graphitic nitrogen atoms in the sp^2 configuration, the electronic conductivities of the composites are reduced by approximately 40% and 55%, respectively, compared to composites with pure graphene ($\sigma_0 \approx 2.6\times10^7$ S/m). Introducing 5% and 10% oxygen at the interface reduces conductivity by ≈ 50% and 65%, respectively. Additionally, a combination of 5% nitrogen and 5% oxygen reduces the conductivity by ≈ 60%, and with 5% nitrogen, 5% oxygen, and 5% sulfur, the conductivity was reduced by ≈ 75%. This

Table 4.2: Structural parameters in copper-graphene composites with different impurity concentrations. All parameters are the average values. C–N: carbon-nitrogen bond distance. δ: Shift from graphitic C–C bond length (1.42 Å). C–N–C: carbon-nitrogen-carbon bond angle. $\Delta\theta$: Shift from graphitic C–C–C bond angles (120 °). C–O: carbon-oxygen bond distance. C–S: carbon-sulfur bond distance. C–O–C: carbon-oxygen-carbon bond angle. C–S–C: carbon-sulfur-carbon bond angle N–Cu: nitrogen-copper bond distance. O–Cu: oxygen-copper bond distance. S–Cu: sulfur-copper bond distance. All distances and angles are in Å and °

Composites	**Impurities in the Graphene Layer**						**Impurities with Copper**	
Cu-Gr +	**C–N**	δ	**C–N–C**	$\Delta\theta$	**C–O / C–S**	**C–O–C / C–S–C**	**N–Cu**	**O–Cu / S–Cu**
N [5%]	1.45	0.03	114.37	5.74	-	-	2.06	-
N [10%]	1.45	0.03	114.14	5.86	-	-	2.05	-
O [5%]	-	-	-	-	1.49	115.70	-	2.03
O [10%]	-	-	-	-	1.48	117.43	-	2.03
N & O [10%]	1.49	0.07	113.20	6.80	1.48	116.78	2.05	2.03
N, O, & S [15%]	1.49	0.07	113.40	6.60	1.42 / 1.75	110.54 / 105.20	1.98	2.03 / 2.10

indicates that oxygen and sulfur impurities have a more detrimental effect on the overall conductivity than nitrogen impurities. Figure 4.8 summarizes these observations on the left axis. Furthermore, the squared density of states was also computed and is plotted on the right axis in Figure 4.8, with values scaled relative to the maximum value for the composite with pure graphene. Indeed, $N^2(\epsilon_f)$, represented by the black line in the figure, follows the trend in electronic conductivity (shown by the green line), except for the case of the model with nitrogen, oxygen, and sulfur atoms.

To analyze the significant reduction of electronic conductivity with the addition of impurities, the extent of structural disorder impurity atoms bring to the planar sp^2 structure

of graphene and at the interface is examined. Table 4.2 provides average structural parameters and distances, illustrating the impact of impurities on graphene's structure and its interface with copper. Nitrogen impurities at concentrations of 5% and 10% lead to slight increases in the C–N bond distance, shift ≈ 0.03 Å, and deviations in the C–N–C bond angles by ≈ 5.8° from the ideal graphitic carbon, indicating significant structural disorder. Notably, with no copper surface, the graphitic nitrogen shows minimal deviation from the ideal planar structure, as reported in [53]. Incorporating oxygen and sulfur into graphene exhibited an equally or more detrimental effect. These atoms break the sp^2 coordination

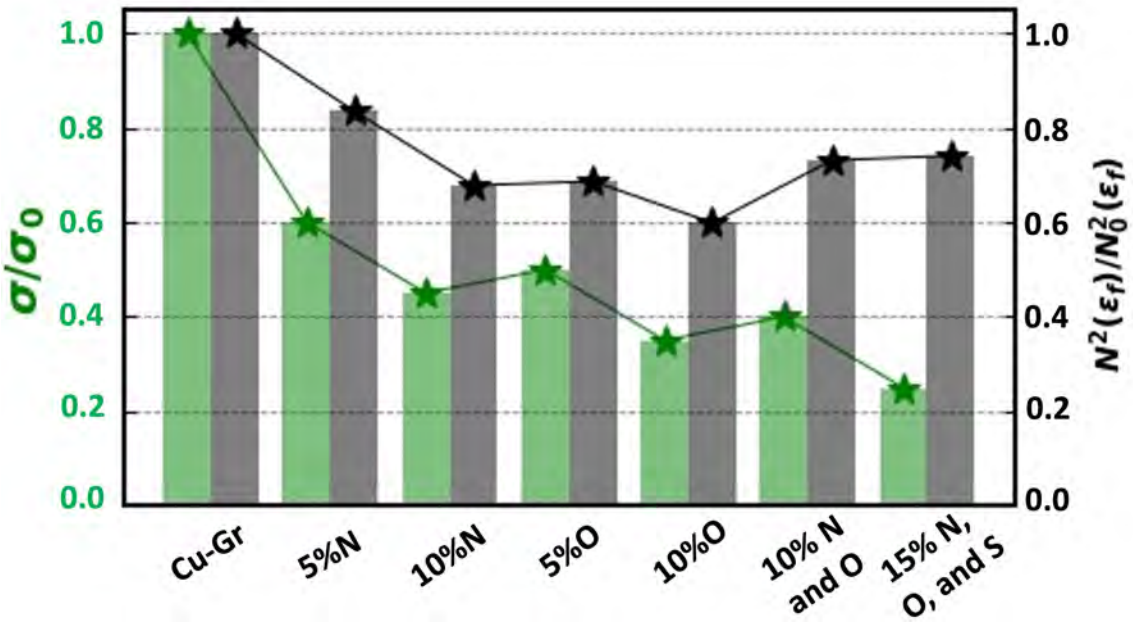

Figure 4.8: [[Left] Electronic conductivity (σ/σ_0) for copper-graphene composites with various impurities, where $\sigma_0 \approx 2.6 \times 10^7$ S/m represents the conductivity of the composite with pure graphene. [Right] Squared density of states ($N^2(\epsilon_f)/N_0^2(\epsilon_f)$) for the same systems, scaled by the value corresponding to the composite with pure graphene. The trends in $N^2(\epsilon_f)$ align closely with the changes in electronic conductivity, except for the case with sulfur due to localized states near ϵ_f.

and migrate towards the copper atoms, forming O–Cu and S–Cu bond length at ≈ 2.03 Å and 2.10 Å. In the interface model with oxygen and nitrogen, A significant shift in C–N bond lengths (0.07 Å) and impurity-centered bond angles (shift in nitrogen-centered C–N–C is ≈ 6.80°) is observed. The presence of sulfur in the graphene sheet further deteriorates the structure. This disorder introduces the undulating graphene structure, disrupting the $\pi-$conjugated graphene network at the interface (See Table 4.2 for detailed structural data).

Next, the electronic density of states (EDoS) for all interface models with impurities is computed. The EDoS is provided in Figure 4.9 (a) for copper-graphene composites with pristine graphene. The spectrum features distinct dip regions near the Fermi level (indicated by the orange vertical line), labeled ”I”. Additionally, the spectrum is characterized by degenerate and extended states near the Fermi level, as shown by the vertical drop lines with a small inverse participation ratio (IPR). With 5% and 10% substitutional nitrogen in the graphene interface, the reduced regions in the EDoS spectrum are filled, shown in Figure 4.9 (b) and (c). This is a consequence of the structural symmetry breaking at the interface due to impurity atoms. It is important to note that substitutional nitrogen does not contribute to localized states near the Fermi level, indicated by the small IPR. In composites containing 10% oxygen, 10% of both oxygen and nitrogen, some states with higher IPR values (labeled ”a” and ”b” in Figure 4.9 (d) and (e) are observed, indicating some degree of electronic state localization around the impurity atoms. The model with nitrogen, oxygen, and sulfur atoms introduces localized states near the Fermi level (labeled ”c”), see the highlighted region in Figure 4.9 (f). This results in a poor agreement between KGF conductivity and N^2, demonstrated in Figure 4.8.

Impurity atoms result in significant structural disorders and reduced electronic conductivity, however, no strong localization of electronic states near the Fermi level was observed. To better understand how these impurities affect charge transport in graphene

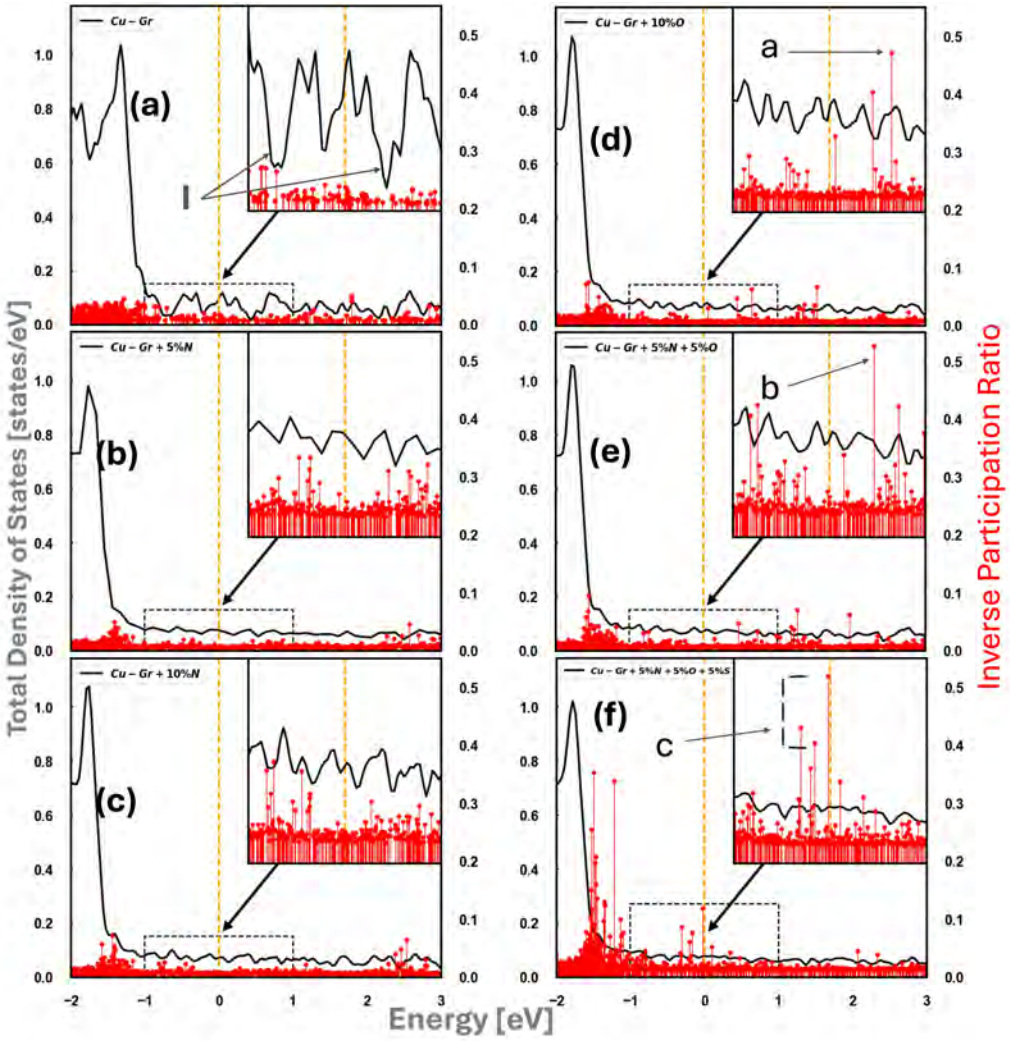

Figure 4.9: Total density of states (TDoS) is shown as black plots on the left axis, and inverse participation ratio (IPR) is shown by red vertical droplines on the right axis. TDoS for copper-graphene composite with (a) no impurity, (b) and (c) 5% and 10 % of the nitrogen in graphene, (d) 10 % of the oxygen, (e) 5% nitrogen and 5% oxygen, and (f) 5% nitrogen, 5% oxygen and 5% sulfur. The Fermi level is set at zero, shown by vertical orange lines. Insets show the high-resolution image for the energy region [-1 eV, 1 eV].

and the composites Bader charge of the impurity atoms and a real-space decomposition $N^2(\epsilon_f)$ is computed.

The in-plane charge density calculations reveal that impurity atoms obstruct the charge flow within the sp^2 network of graphene. They can trap carriers, reducing the overall mobility of electrons in the graphene sheet and impacting the composites' electrical conductivity. This effect is quantified by computing the Bader charge in interface models. In models with nitrogen and/or oxygen, the average Bader charge in nitrogen and oxygen was increased by ≈ 0.90 eV per atom and by 0.95 eV per atom, respectively. This charge redistribution to impurity atoms reduced the average charge gained by carbon from the copper atoms. At a shorter interface distance, $d_{Cu-G} = 2.32$ Å, the average charge in carbon atoms reduced from around 0.1 eV to 0.05 eV per atom. Further, adding sulfur into these interface models with nitrogen and oxygen reduced the average charge gained by carbon atoms to 0.02 eV per atom.

Next, the SPC along the plane and transverse to the graphene layer is computed. SPC favors pathways consisting of carbon atoms along the hexagonal structure, while impurity atoms terminate the transport, as illustrated in Figure 4.10 (a). Moreover, the undulating structure of graphene, coupled with impurities, disrupts the continuous network across the copper grains and hinders orbital mixing at the interface. This disruption results in reduced transport across the graphene, as evidenced by the discontinuous and weaker network of SPC, shown in Figure 4.10 (b), contrasting with the continuous network observed with pristine graphene at the interface (see Figure 4.11 (f)).

4.2.4 Electronic Transport From Squared Charge Density Near the Fermi Level

Spatially projecting N^2 involves computing the band-decomposed squared charge density as defined in Equation 2.29. For this, 60 single-particle Kohn-Sham states that are within the vicinity of the Fermi level were used as wave functions. Since the electronic

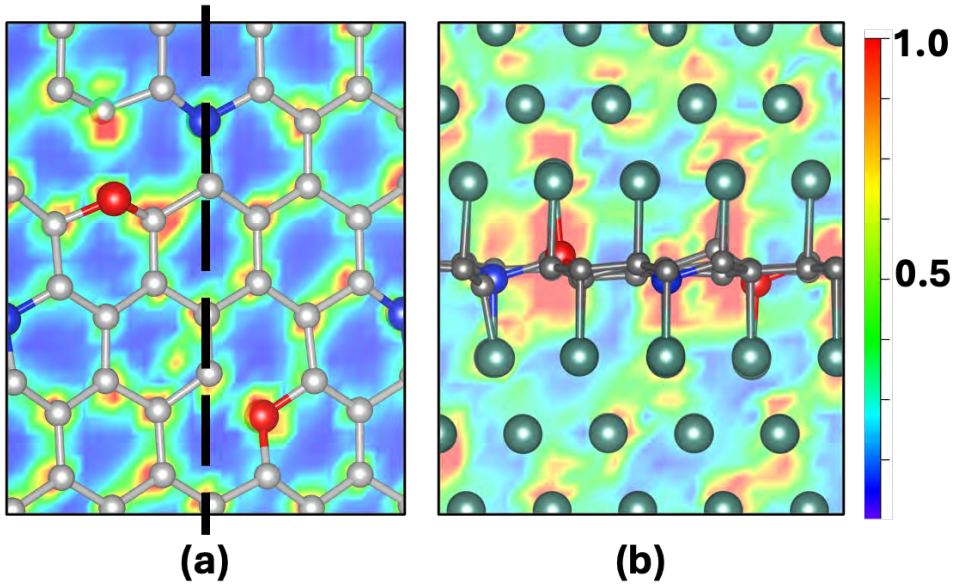

Figure 4.10: The two-dimensional heat map of SPC for copper-graphene composites with impurity atoms (scaled by the maximum value) visualized along (a) within the plane and (b) perpendicular to the graphene plane. Copper, carbon, nitrogen, and oxygen atoms are represented by green, silver, blue, and red spheres, respectively. The color bar indicates the intensity of favorable conduction pathways, highlighted by regions in red or reddish-yellow.

density of states is an intrinsic property of any quantum system, it is expected that the N^2 projections should be consistent across any complete basis set, whether constructed from plane waves, atomic orbitals, Wannier functions, or other relevant representations. The δ function in Equation 2.29 was approximated with a Gaussian function with a smearing width of 0.05 eV. Although the numerical value depends on this width, the spatial projection of N^2 remained smooth and consistent.

$\bar{\zeta}(\epsilon_f, \mathbf{r})$ is shown as a heat map in Figure 4.11 (d-f) for the composites with different grain orientations. The red (high intensity $\bar{\zeta}(\epsilon_f, \mathbf{r})$) depicts the region in interface with active

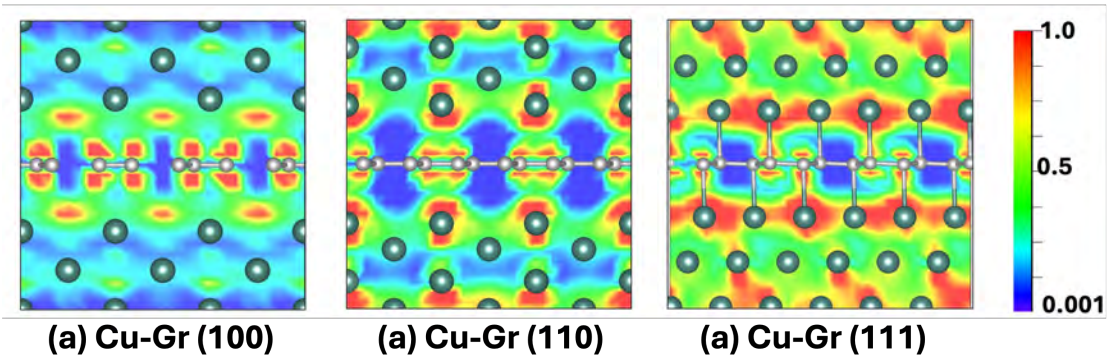

Figure 4.11: The spatial projection of N^2, i.e., the local density of states from Kohn-Sham orbitals near the Fermi level, visualized as a heatmap perpendicular to the graphene plane for composites (a) (100), (b) (110), and (c) (111) copper grains. Values are scaled by the maximum value for the composite with (111) grain. The grey and green spheres are carbon and copper atoms, respectively. The color bar indicates the intensity of the conduction active region, increasing from blue to red.

conductive areas, while blue represents low conductive regions. A visual inspection shows that the interface between (111) copper-matrix and graphene shows higher interactive networks, followed by composites with (110) and (100) copper, depicted in Figure 4.11 (d-f) respectively. These interactive regions at the contact signify graphene's role as a connecting link across the copper grains. Further, the efficiency is associated with the grain orientations.

4.2.5 Charge Density Near the Fermi Level to Estimate the Conduction Activity in Materials

Here, the density of states at the Fermi level to identify regions of active conduction activity is considered, and a comparison with the results from the proposed N^2 method is

offered. The electronic density of states is defined in Equation 2.25a for $E = \epsilon_f$. The spatial projection of $N(\epsilon_f)$ over the electronic states near the Fermi level is obtained as:

$$\chi(\epsilon_f, \mathbf{r}) = \frac{1}{M} \sum_i |\psi_i(\mathbf{r})|^2 \delta_f^i \tag{4.1}$$

As required, the volume integral of the Equation 4.1 results in $N(\epsilon_f)$. To compute $\chi(\epsilon_f, \mathbf{r})$, the density of states is projected onto 60 single-particle Kohn-Sham states near the Fermi level, and the δ function is approximated with a Gaussian function with a smearing width of 0.05 eV.

The spatially-resolved density of states, $\chi(\epsilon_f, \mathbf{r})$, is depicted as a heat map in Figure 4.12 for composites with various grain orientations. High-intensity regions, shown in red, correspond to areas of active conduction activity at the interface, while blue regions indicate low. The heat map in Figure 4.12 depicts the highest interaction between graphene and (111)-oriented copper, followed by (110) and (100) orientations. However, the conduction pathways are not as distinctly predicted by $\chi(\epsilon_f, \mathbf{r})$. The space-resolved N distribution is more local on individual atoms, while no visible interacting network across the interface is formed. In contrast, the space projected N^2, $\bar{\zeta}(\epsilon_f, \mathbf{r})$, the patterns in images Figure 4.11 (d-f) reveal more extensive and interconnected regions of high intensity, indicating the pathways that are electronically favorable.

Next, $\bar{\zeta}(\epsilon_f, \mathbf{r})$ along the plane and transverse to the graphene layer is computed. $\bar{\zeta}(\epsilon_f, \mathbf{r})$ favors pathways consisting of carbon atoms along the hexagonal structure, while impurity atoms terminate the transport, as illustrated in Figure 4.10 (a). Moreover, the undulating structure of graphene, coupled with impurities, disrupts the continuous network across the copper grains and hinders orbital mixing at the interface. This disruption results in reduced transport across the graphene, as evidenced by the discontinuous and weaker network of $\bar{\zeta}(\epsilon_f, \mathbf{r})$, shown in Figure 4.10 (b), contrasting with the continuous network observed with pristine graphene at the interface (see Figure 4.11 (f)).

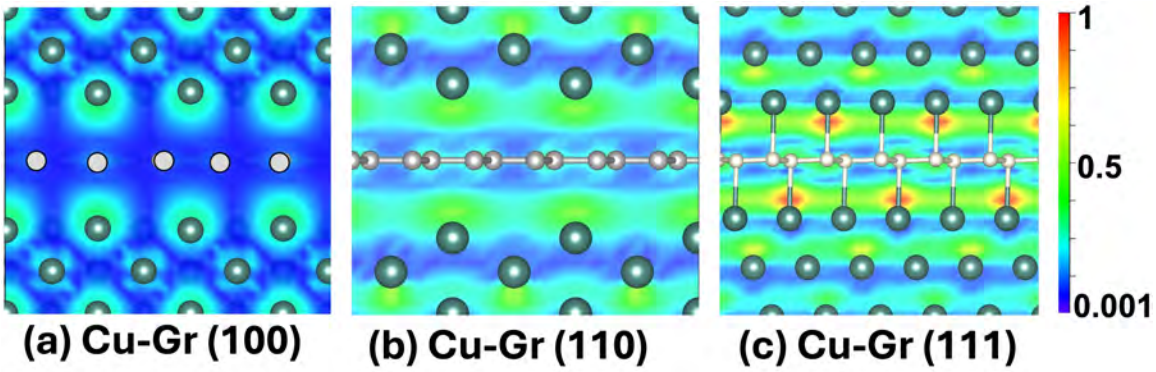

Figure 4.12: The spatial projection of N, i.e., the local density of states from Kohn-Sham orbitals near the Fermi level, visualized as a heatmap perpendicular to the graphene plane for composites (a) (100), (b) (110), and (c) (111) copper grains. Values are scaled by the maximum value for the composite with (111) grain. The grey and green spheres are carbon and copper atoms, respectively. The color bar indicates the intensity of the conduction active region, increasing from blue to red.

The N^2 formalism, which identifies electronically active conduction sites in materials is introduced. Using the method, visual evidence for copper-graphene composites with (111) grains demonstrating the highest electronic dynamics at the interface compared to (110) and (100) configurations is provided. Additionally, the presence of impurities, such as nitrogen, oxygen, and sulfur, in graphene sheets diminishes conductivity, highlighting the sensitivity of electronic properties to defects. These results provide valuable insights into optimizing the design and fabrication of metal-graphene composites for electronic applications, emphasizing the need for precise control over structural alignment and impurity levels to harness their full potential in next-generation electronic devices.

4.2.6 Conclusion

The electronic and transport properties of copper-graphene composites with different crystal orientations of copper grains and the incorporation of graphene with impurities are studied. From *ab initio* density functional theory calculations, it was identified that the orientation of copper grains significantly influences the electronic conductivity of the composites, with the (111) orientation exhibiting the highest conductivity due to favorable contact with graphene. Our findings emphasize the importance of contact alignment in enhancing carrier transport across interfaces. This work posits that controlling the structural alignment can tailor the electronic performance of graphene-based devices, offering potential advancements in areas ranging from flexible electronics to energy storage and beyond.

5 Metal-Coal Composites: Role of Functional Impurities and Topological Disorder.

Associated Publication

1. **K. Nepal**, R. Hussein, Y. Al-Majali and D. A. Drabold, Electronic conduction in copper-graphene composites with functional impurities, J. Chem. Phys. 163, 124701 (2025)

Graphene has been extensively recognized in the material science community and is a key material in electronics devices for its exceptional performance in applications such as electro-chemical sensing devices [157], transparent conductive electrodes [158], battery electrodes [159], energy-storage devices [160, 161], and lubricants [162]. Its recent role as an additive into FCC metals like aluminum and copper led to the development of ultraconductors, which have further extended its already remarkable versatility [163, 164]. There has been a shift toward integrating coal-derived graphene [24–28], which offers a cost-effective and scalable approach to producing metal-carbon composites.

Coal-derived graphene has the potential to be an accessible and cost-effective source for high-performance ultra-conductors for a range of applications. Unlike conventional graphene production methods, which are challenging for large-scale production, coal-derived graphene utilizes an abundant and inexpensive raw material, making large-scale production economically viable [26, 28, 165–168]. Various methods exist for producing coal-derived graphene: direct carbonization through pyrolysis, chemical exfoliation involving oxidation-reduction, microwave-assisted methods utilizing rapid heating, and laser-induced graphene (LIG) offering precise control and patterned structures [26, 27, 54–62]. This opens the door to widespread applications, from advanced electronics and energy storage to composite materials and high-efficiency conductors. As the world pushes toward greener, more efficient technologies, coal-derived graphene is poised to play a crucial

role. To ensure the effective industrial application of high-performance metal-graphene conductors, it is critical to systematically examine how graphene's quality—specifically its purity, structure, and defect density—affects the composite's electrical properties.

We first describe the structural and electronic properties of sp^2 common coal. Next, we present a simulation of carbon-coal composites, aiming to provide insights for engineering optimized metal-graphene electronic devices. The Kubo-Greenwood formula (KGF) and space-projected conductivity (SPC) are used to spatially resolve electronic conductivity, demonstrating that both crystal orientation and graphene purity play critical roles in determining the electronic transport in the composites. We show that functional groups and ring disorder in the metal-graphene interface result in localized states near the Fermi level, with functional groups contributing primarily to states below it and disordered rings contributing to states above. These states act as carrier-trapping sites, disrupting coherent electronic interactions at the interface. Composites involving hydroxides showed higher electronic conductivity than oxide composites with pristine graphene; hydroxides are more or equally detrimental in composites with disordered graphene. Next, we show that, with a high density of impurities, the electronic conductivity is largely unaffected by the interfacial purity of graphene, implying that impurity-driven scattering overshadows the benefits of using pristine graphene. A significant limitation is that only T = 0 K results are reported, thus neglecting phonon scattering. This is discussed within an adiabatic approximation [79, 82].

The rest of this chapter is organized as follows: Section 5.1 provides a summary of the computational models used in this work. Sections 5.1.1 and Section 5.1.2 detail the simulation protocols and methodologies utilized for electronic properties and electronic conductivities calculations. In Section 5.2, the interface signatures and electronic transport of copper-carbon composites with functional impurities and ring disorder are reported.

Copper-composites based on crystalline graphene and functional impurities, and the coal-based metal composites (CMC) are detailed in section 5.2.2.

5.1 Computational Methodology

5.1.1 Electronic Structure Calculations

The conjugate gradient algorithm, as implemented in VASP, was applied in the geometry optimization of the models to minimize the total energy of the modeled systems. The convergence criterion for the forces on atoms of the configuration in an iteration step was set at 1×10^{-6} eV. Geometric relaxation of layered graphene (amorphous and pristine), with and without functional impurities, employed Γ point sampling of the Brillouin zone, while the Monkhorst-Pack scheme [114] with 2×2×1 $\boldsymbol{k}$-points was implemented for the orthorhombic unit cell of the "sandwich" structure of metal-graphene composite. Periodic boundary conditions were used in all the calculations, such that an infinite sheet of planar graphene sheets is repeated for $\approx$ 20-25 Å along the transverse direction. We used a plane-wave basis set with a kinetic energy cutoff of 420 eV. Projected augmented wave (PAW) [105] potentials to account for ion-electron interactions, and the generalized gradient approximation of Perdew-Burke-Ernzerhof (PBE) [106] as the exchange-correlation functional. We implemented Grimme's van der Waals (D2) correction [115] during structural relaxation of the interface models. A kinetic cut-off of 520 eV was implemented for electronic structure and electronic conductivity calculations. We note that the convergence of electronic structure calculations was well tested.

5.1.2 Electronic Conductivity, Space-Projected Conductivity

We computed electronic conductivity using the Kubo-Greenwood Formula. For the atomistic local distribution of conductivity, we computed the space-projected conductivity (SPC), an extension of the space decomposition of KGF. The methodology for SPC is

detailed elsewhere [76]. For larger supercells that have a relatively dense electronic density of states near the Fermi level, a smaller broadening width can be invoked, which provides better agreement with experiment (as reported by Subedi *et. al.*[82] for FCC aluminum).

For this work, we focus on the DC limit, where the frequency of the Kubo field goes to zero ($\omega = 0$) in Equation 2.9. Next, in the Equation 2.9, the single-particle Kohn-Sham states $\psi_{i,k}$ were computed from static calculations in VASP, the Fermi-Dirac distribution was approximated at 1000 K smearing temperature, and the δ function by a Gaussian distribution with a width k_BT (where K_B and T are the Boltzmann constant and smearing temperature). While the exact conductivity value from Equation 2.9 depends on the choice of Gaussian width, the qualitative analysis remains largely unaffected, as demonstrated in [82].

5.2 Results and Discussions

5.2.1 Structural and Electronic Properties of Graphene with Functional Impurities

Functional impurities (oxidation groups) and ring disorder (pentagons and heptagons at grain boundaries) are common features of graphene. Ring disorder may create local curvature (non-planarity) and influence the electronic properties of the material [50, 169]. In this section, we model and analyze the structure of graphene with topological disorder, followed by the effects of functional impurities, examining their corresponding electronic properties.

5.2.1.1 Pristine Graphene With Functional Impurities. Oxides and hydroxides are common functional impurities in graphene. A layer of graphene with these functional impurities is created from a sp^2 carbon layer; a representative structure is shown in Figure 5.1 (a). We simulated models with an epoxy group, the schematic of the relaxed layer is shown in Figure 5.1, models with hydroxide groups, and models with epoxy and hydroxide,

see Figure 5.1(b-c). After energy minimization, significant structural modifications were observed in hexagonal graphene. The local bonding environment of graphene with different oxidation groups is shown in Figures 5.1 (d-e). Epoxy group in graphene disrupts the sp^2 coordination of carbon atoms, forming fourfold-coordinated carbon atoms. This structural modification weakens the C-C bonds. These fourfold carbon atoms exhibit a longer bond length of ≈ 1.56 Å. Longer bond lengths are reported for fourfold carbon atoms in graphene [170], and sp^3 diamond [171]. The average bond length between C and O was 1.47 Å. In the model with hydroxide groups, the O-H bond length was observed at 0.98 Å, while the C-O bond length was ≈ 1.48 Å. A C–O–H bondangle was ≈ 107.3°. In models with oxides and hydroxides, singly-bonded C and O atoms at 1.46 Å, while double-bonded C and O showed a shorter bond length of ≈ 1.23 Å. Refer to Table 5.1 for the summarized structural parameters for these different models.

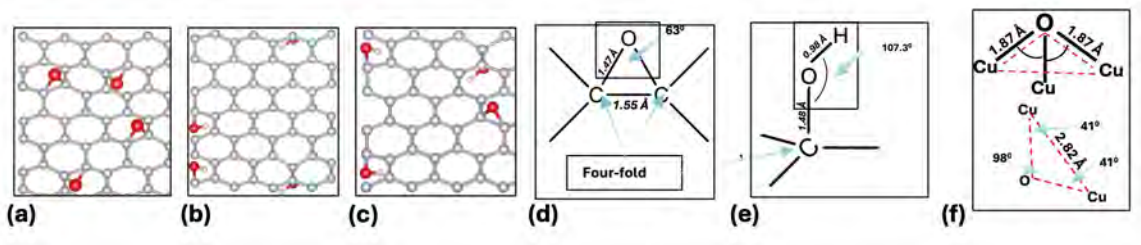

Figure 5.1: Pristine sp^2 graphene with functional impurities (a) epoxides, (b) hydroxides, (c) epoxides and hydroxides. (d-e) local bonding chemistry of the epoxide group and the hydroxide group, respectively. (f) triangular pyramid arrangement of copper and oxygen at the copper-graphene interface. The numbers are average values. Color nomenclature: Brown-copper, gray-carbon, red-oxygen, and white-hydrogen.

The electronic density of states (EDOS) and the electronic inverse participation ratio (EIPR) of graphene with different oxidation groups were investigated to examine the impact of structural modification on its electronic properties. The EDOS at the Fermi level (E_f)

Models	**Functional Group -**	**Bond-angle C-O-C [°]**	**Bond-length C-O [Å]**	**Bond-length C–C (four-fold)[Å]**	**Bond-length O-H [Å]**	**Bond-angle C-O-H [°]**
Gr-O	-O-	63	1.47	1.56	-	-
Gr-OH	-OH	-	1.48	-	0.98	107.3
Gr-O-OH	-O/-OH	64/-	1.46/1.48	1.55/-	-/0.98	-/107.1
aGr-O	-O	62	1.45	1.51	-	-
aGr-OH	-OH	-	1.47	-	0.98	106.8
aGr-O-OH	-O/-OH	64/-	1.46/1.50	1.56/-	-/0.98	-/107.09

Table 5.1: Average structural parameters of functionalized graphene with oxygen and hydroxyl groups. C–O–C: carbon-oxygen-carbon bond angle, C–O: carbon-oxygen bond distance, C–C: carbon-carbon bond distance, O–H: oxygen-hydrogen bond distance, C–O–H: carbon-oxygen-hydrogen bond distance.

provides insight into the transport processes in the materials. With extended states at E_F, as illustrated in [164], the conductivity scales as the square of the electronic density of states at the Fermi level [$\sigma \propto N^2(E_f)$], and regions of conduction activity in the material microstructure can be mapped out by spatial projection of $N^2(E_f)$ [164]. To enhance electronic conductivity, one needs to modify the material's microstructure to increase the density of states at the Fermi level.

The electronic density of states (EDOS) and the electronic inverse participation ratio (EIPR) of graphene with different oxidation groups were studied to analyze the influence of structural modification on electronic properties. The EDOS, especially at the Fermi level (E_f), provides insight into the transport processes in the materials. With extended states at E_F, as illustrated in [164], the conductivity scales as the square of the electronic density of states at the Fermi level [$\sigma \propto N^2(E_f)$], and regions of conduction activity in the material microstructure can be mapped out by spatial projection of $N^2(E_f)$. To enhance electronic

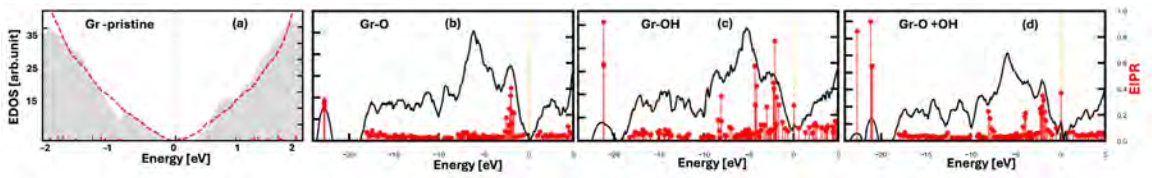

Figure 5.2: [Left-axis]](a) Electronic density of states (EDOS) for pristine graphene. The red dashed line is EDOS from Reference [3], (b) Electronic Density of states for pristine graphene with functional impurities. [right-axis] Electronic Inverse Participation Ratio (EIPR) for the same models. Localized states are indicated by high EIPR values for graphene with functional impurities. The yellow vertical line represents the Fermi level.

conductivity, one needs to modify the material's microstructure to have an increased density of states at the Fermi level. This is reminiscent of "gap sculpting", designing the material with desired electronic properties through biased atomistic simulation [172, 173]

For qualitative comparison, first, the EDOS and EIPR were computed for pristine graphene, shown in Figure 5.2 (a), left and right axes, respectively. Notice a clear EDOS minimum at the Fermi level, and electronic states are extended as indicated by low EIPR values (red vertical drop lines). Next, for models with oxides, shown in Figure 5.2(b), depicts a shoulder peak at -2 eV below the Fermi level. EIPR corresponding to this peak shows some degree of localization (shown by red vertical droplines with higher IPR values). Atomic projection of these states shows that the major contribution to these localized states arises from the oxygen atom in the model. A similar shoulder peak at -2 eV below the Fermi level is observed for a graphene model with hydroxide, shown in Figure 5.2(c). In the Gr-OH model, energies ranging from -8 eV to -2 eV below the Fermi level show several localized electronic states, as indicated by higher EIPR values (red vertical drop lines). For the Gr-O-OH model, localized electronic states contributed by both oxides and hydroxides below the Fermi level were observed, shown in Figure 5.2 (d).

5.2.1.2 Amorphous Graphene With Variable Ring Disorder and Functional Impurities. We simulated three topologically disordered graphene samples (amorphous graphene, aGr) with varying defect densities, following the protocol detailed in [42]. Starting from random initial configurations, layers of amorphous graphene were generated by subjecting them to first-principles simulations at approximately 3000 K and graphitic density. The resulting structures exhibited layers of sp^2 carbon with varying degrees of topological disorder, quantified by n_6/n, where n_6 and n are the numbers of hexagonal and non-hexagonal carbon rings, respectively. From the amorphous graphene layers, those with lattice parameters closely matching those of copper surfaces (used in this work, see section 5.1.1) were selected to create the copper–amorphous graphene composite model. For $n_6/n = 3.0$, there is one non-hexagonal ring for every 3 hexagonal rings. Three models with $n_6/n = 1.3,\ 2.2$, and 3.0 were simulated to study the electronic consequence of topological disorder in graphene. Refer to Figure 5.3 (a) for a representative model corresponding to $n_6/n = 3.0$. Next, oxides and hydroxides were introduced into aGr with defect density $n_6/n = 3.0$. The structural features associated with functional impurities are summarized in Table 5.1. The representative structure of aGr with oxidation groups is shown in Figure 5.3 (b). We label the models of aGr with oxides and hydroxides as aGr-O and aGr-OH, respectively, and models with both oxidation groups as aGr-O-OH.

EDOS and EIPR for aGr with varying n_6/n were computed and compared to pristine graphene, see Figure 5.4. EDOS spectrum for aGr (black plots) models shows no distinct DoS minimum at the Fermi level, otherwise present in pristine Gr, shown in Figure **??** (a). In addition to that, electronic states at energies ≈ 5 eV above the Fermi level display some degree of localization, as indicated by their high IPR values (gray vertical drop lines). The projection of these states into atomic contributions showed that carbon atoms common to pentagons and heptagons contribute the most. While EDOS spectra in aGr with variations in the n_6/n ratio do not appear to cause significant changes in the EDOS spectra, we report

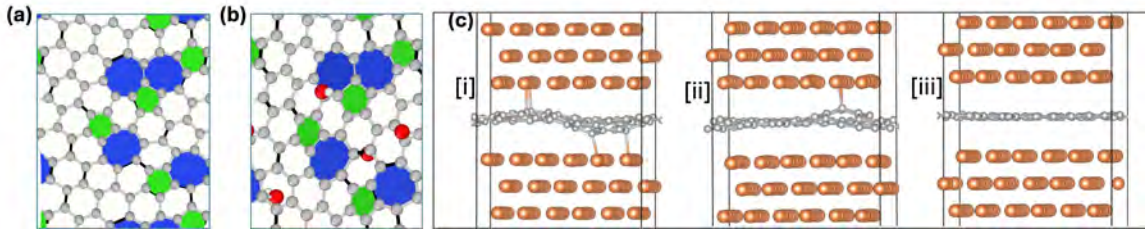

Figure 5.3: (a) Amorphous graphene showing sp^2 non-hexagonal rings. (b) Functional impurities (oxide and hydroxide groups) in amorphous graphene. Colored-rings: blue-heptagon, green-pentagon. Black colored bonds correspond to long bond lengths in amorphous graphene. (c-e) Relaxed structure of amorphous graphene with increasing hexagonal carbon rings in the system, respectively. Color nomenclature: Brown-copper, gray-carbon, red-oxygen, and white-hydrogen.

new features in aGr (especially in the vicinity of the Fermi level) not present in pristine graphene.

With oxides in aGr, localized states at ≈ 2 eV below the Fermi level were observed. These are illustrated in Figure 5.5(a-b) for single oxide and two oxides in aGr, respectively. For aGr-OH, more states near the Fermi level are localized, indicated by higher IPR values in Figure 5.5(c-d). In addition, localized electronic states ≈ 5 eV above the Fermi level in aGr indicate the presence of non-hexagonal rings in the material.

5.2.2 Copper-graphene composites

5.2.2.1 Orientation Dependence of Electronic Conductivity. Following the work by Nepal *et. al.* [164], strong orientational dependence in conductivity was observed in composites for different copper crystal orientations. Ideal low-energy interface structures were formed between the (111) and (110) copper surfaces and sp^2 graphene, exhibiting higher electronic conductivity [164]. The finding was evidenced by the increased interface electron dynamics and a spatial projection of the squared density of states at the Fermi level.

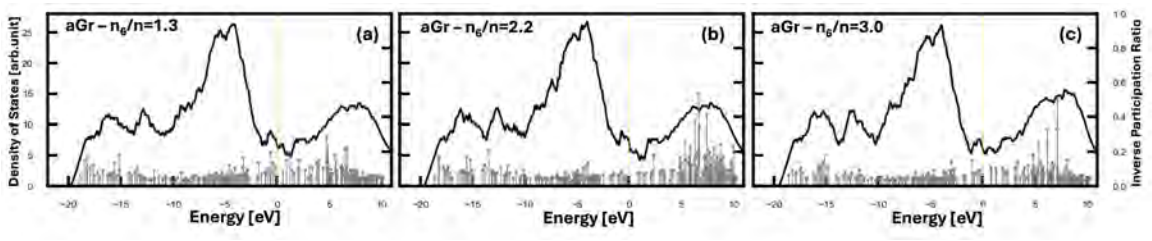

Figure 5.4: [Left axis] Electronic density of states and [Right axis] Electronic Inverse participation ratio for (a) pristine graphene and (b-d) amorphous graphene models for varying disorder density (labeled in legends). Localized states are induced with topological disorder in graphene as indicated by high IPR values near 5 eV above the Fermi level. The yellow vertical line represents the Fermi level.

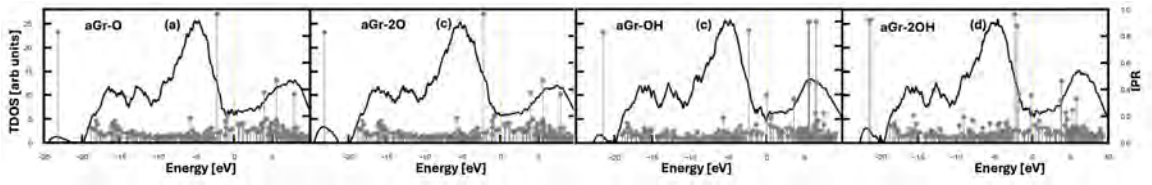

Figure 5.5: [Left-axis] Electronic density of states for amorphous graphene with varying functional impurities, as shown by plots' legends. [right-axis] Electronic Inverse Participation Ratio for the same models. Localized states are induced, indicated by high IPR values, with topological disorder [5 eV above the Fermi level] and functional impurities (the majority of localized states at energies below the Fermi level). The yellow vertical line represents the Fermi level.

To add, we computed the real-space projection of the KGF conductivity for composites with copper in three different crystallographic directions ((111), 110, and (100)).

The connectivity and continuity of conduction activity within the composite are analyzed by computing transverse SPC. By visualizing SPC through two-dimensional

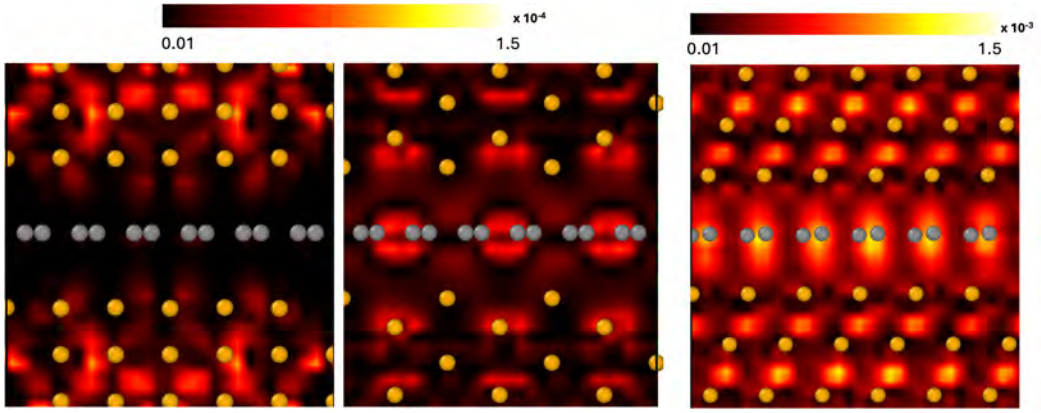

Figure 5.6: Space projected conductivity as a heat map showing the conduction active region at the copper-graphene interface. Figure a(a-c) corresponds to the interface of graphene with (111), (110), and (100) copper grains, respectively. The colorbar shows the intensity of SPC increasing from dark to red to bright. Color Nomenclature: Brown: copper, grey: carbon.

heatmap plots, we identify regions of high and low conductivity, aiding in the analysis of how different contacts between graphene and grain orientations impact the overall electronic performance of the composite. The ”Top FCC” registry formed between graphene and (111) copper induces a continuous network for carrier transport. This results in resonant mixing at the Fermi level, forming highly conductive pathways at the interface. This is highlighted by the high SPC regions in Figure 5.6 (a). (110) copper formed ”bridge” registries with lower connectivity at the interface as compared to (111) (see Figure 5.6 (b), however, poor connectivity at the interface contact between graphene and (100) copper facilitates comparatively lesser carrier transport. Figure 5.6(c) reveals this with low-intensity SPC values. As noted in the previous literature, atomic alignments forming low-energy registry alleviate scattering, whereas misaligned geometries tend to act as sources of scattering [83, 84].

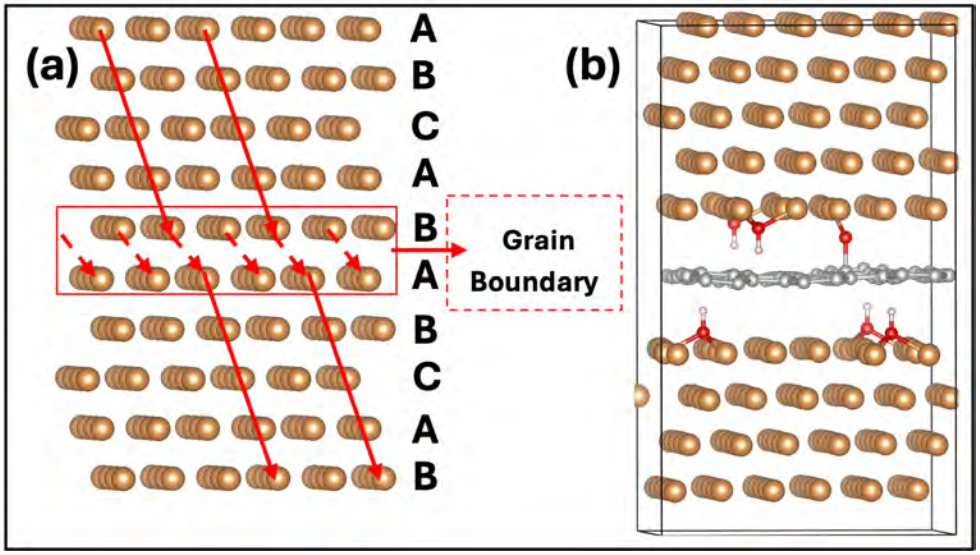

Figure 5.7: Relaxed structure of (a) (111) copper with a stacking fault forming a simple grain boundary model. The lines are guides to the eye to visualize the grain defect in the model. (b) interface model of amorphous graphene with functional impurities in (111) copper matrix. Color Nomenclature: Brown-copper, gray-carbon, red-oxygen, and white-hydrogen.

For the rest of the paper, we work on the (111) oriented copper composites. An orthorhombic cell of 240 atoms of the Cu-only system with a fault layer is modeled, shown in Figure 5.7(a), representing a simple, realistic grain boundary model, for comparison purposes. The KGF conductivity for the copper-only system was scaled to the standard IACS value (σ_{Cu}) $\approx 5.8 \times 10^7$ Siemens/m). Whenever required, a comparison is made with the pressurized copper-graphene composite model, which exhibits an electronic conductivity $\approx$ 118 % IACS. We computed conductivities from Equation 2.9 for smearing widths 0.05-0.005 eV that approximate a delta function. For larger supercells that have a relatively dense electronic state splitting near the Fermi level, a smaller broadening width can be considered, which provides better agreement with the experiment, as reported by

[82] for FCC aluminum. For this work, we find that the smearing width of 0.005 eV is in close agreement with the experiment. The dependence of electronic conductivity on the smearing width and other factors such as the number of atoms, smearing temperature, and the energy cut-off for finite-size cells is discussed in the References [107–109]. In addition, References [77, 83] detail the dependence of electronic conductivity in aluminum and copper-based composites with external pressure.

5.2.2.2 Pristine Graphene With Functional Impurities in Copper Matrix. The interface structures with the graphene structure containing common coal functional groups were created and structurally relaxed (representative structure for a relaxed interface is shown in Figure 5.7 (b)). Post-relaxation, the functional groups -O- and -OH migrate from their interstitial sites towards interface copper atoms (not all functional O migrate, but all -OH migrate). This results in a variety of bonding environments, forming a complicated structure at the metal-graphene interface. Hydroxides attached to carbon atoms migrate to form a metal hydroxide (Cu-OH), while the oxide group forms metal oxides (Cu-O-Cu). Oxygen also formed an interlink connecting interface carbon and copper (forming a Cu-O-C structure). A more complicated tetrahedron geometry with Cu_3O chemical composition, shown in Figure 5.1 (f) [top], was observed at the interface. Oxygen sits at the apex of three neighboring planar copper atoms such that any Cu–O–Cu forms a perfectly planar structure (sum of internal angles is equal to 180 degrees), as illustrated in Figure 5.1 (f)[bottom]. These copper atoms form a distorted local configuration exhibiting longer Cu–Cu bond lengths ($d_{Cu-Cu} \approx 2.82$ Å). This suggests that copper reacts strongly with oxygen, forming complex chemical environments at the interface. Our findings can guide an experiment that provides in-depth interfacial chemistry of the material and engineers the material for optimal efficiency. The microstructure of the extruded copper-graphene

composites is likely to have regions of copper oxide, leading to localized oxidation at the interface.

5.2.2.2.1 Electronic Density of States With -O and -OH. The total density of states (black plots) and the projected density of states in copper (green plots), carbon (red plots), oxygen (red plots), and hydrogen (cyan plots) atoms for copper-graphene composite with functional impurities are shown in Figure 5.8. Plots in the last row of Figure 5.8 show the electronic inverse participation ratio as grey-colored drop lines. For all plots in Figures 5.8, yellow-colored vertical lines represent the Fermi level shifted to zero. Insets in the first row in Figure 5.8 compare the total density of states to the projected density of states into copper atoms and the density of states for the Cu-only model (red-dashed line). The projected density of state at the Fermi level for copper atoms in the composite is comparable to the TDOS of the Cu-only system; meanwhile, this is slightly lower than the TDOS in the copper-graphene system. This suggests an increase in electronic states near the Fermi level with graphene additions, an electronic characteristic consistent with previous reports [77, 83].

For the Cu-Gr-O model, the PDOS of oxygen atoms shows small peaks at energies -1.0 and -6.0 eV below the Fermi level. For the Cu-Gr-OH model, the PDOS into oxygen and hydrogen atoms peaks at energies -1.0, -6.0, and -9.0 eV below the Fermi level. Note an additional peak at -9.0 for the Cu-Gr-OH model, dominantly from the H. Peaks at energies -1.0, -6.0, and -9.0 eV below the Fermi level for the Cu-Gr-O-OH models were observed. See Figures in the second row in Figure 5.8. For each composite model with functional impurities, the localized electronic states, as illustrated with the higher electronic inverse participation ratio, shown in the bottom row in Figure 5.8, correspond to the energies where PDOS into oxygen and hydrogen atoms peaks.

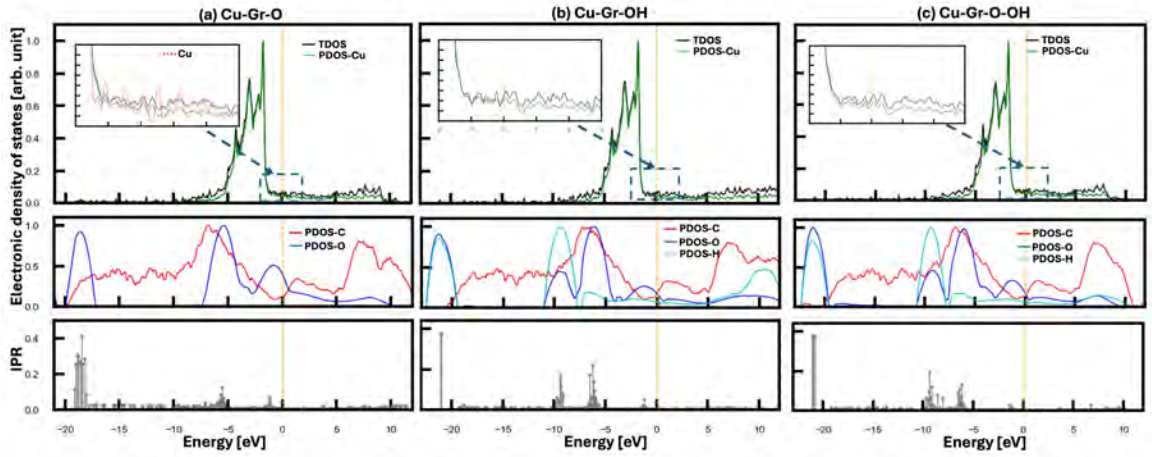

Figure 5.8: Total density of states (TDOS) in copper-graphene composites (Cu-Gr) with different functional groups shown in black plots. Projected density of states into copper (green plots), carbon atoms (red plots), oxygen atoms (blue plots), and hydrogen (cyan plots). The electronic inverse participation ratio is shown as a grey colored vertical dropline. The Fermi level is shifted to zero, shown by yellow vertical lines in each plot. (a-c) respectively corresponds to copper-graphene composites with oxides, hydroxides, and both oxidation groups. The inset in (a) compares the PDOS of Cu and TDOS of the composites with the copper-only model (red dashed lines) in the vicinity of the Fermi level.

5.2.2.2.2 Electronic Conductivity With -O and -OH. Next, the conductivity of the interface models was computed and compared to the conductivity of a pure copper-only and impurity-free copper-graphene composite. Detailed electronic and transport behavior of impurity-free copper-graphene composites has been previously reported [77, 164]. The EDOS shows that functional impurities have some degree of consequence for the localization of electronic states, intuitively expecting a significant effect on the transport properties of the composite. For the Cu-Gr interface with increasing oxidation groups, the electronic conductivity decreased. With two and four oxides, the material exhibits

the electronic conductivity of $\approx$ 54% and $\approx$ 43% IACS. Carbon atoms gain ($\triangle q$) $\approx$ 0.02 e^{-1}/atom on average from interface copper atoms, while the charge accumulation to oxygen atoms at the interface is significantly higher ($\triangle q \approx 0.9$ e^{-1}/atom). This is a reduction of 40 % of charge transfer to carbon atoms from the interface copper as compared to the impurity-free Cu-Gr composite. With -OH functional impurities, the charge transfer to carbon is 0.03 e^{-1}/atoms, with significant charge accumulation in oxygen ($\rangle$ 1 e^{-1}/atom), the majority of which is from hydrogen atoms. Composites with hydroxides exhibited slightly higher electronic conductivity as compared to oxides in the composite interface. Cu-Gr composite with two OH functional groups exhibits electronic conductivity $\approx$ 70.1 % IACS, while this value reduces to 55.5 % with four hydroxide groups. Figure 5.9 summarizes the conductivity results for composites with varying functional impurities compared to the copper system computed at 300K .

5.2.2.3 Amorphous Graphene in Copper Matrix. Interface structures were created with amorphous graphene with a varying n_6/n. Amorphous graphene in copper matrix forms an undulating structure, shown in Figure 5.3 (c-d), due to non-hexagonal rings causing puckering of amorphous graphene [169]. With increasing order in the topology of graphene, a planar structure is observed at the interface, highlighted in Figure 5.3(e). The PDOS and IPR plots for Cu-aGr composites for varying n_6/n show reduction of the localization of states (at energies 5 eV above the Fermi level), as highlighted with electronic states with low IPR values in Figure 5.10 (a), while the DOS spectrum shows no significant variations. The KGF conductivity of the composites varied with n_6/n aGr in microstructure, providing insights into the sensitivity of electronic conductivity to topological disorder in graphene. The electronic conductivity for n_6/n = 3.0 is ($\approx$ 74 % IACS, with further reduction with lower n_6/n. Conductivities for n_6/n = 2.2 and n_6/n = 1.3 are $\approx$ 65 % and $\approx$ 56 % IACS. The comparison is illustrated in Figure 5.10 (b). Note that the electronic

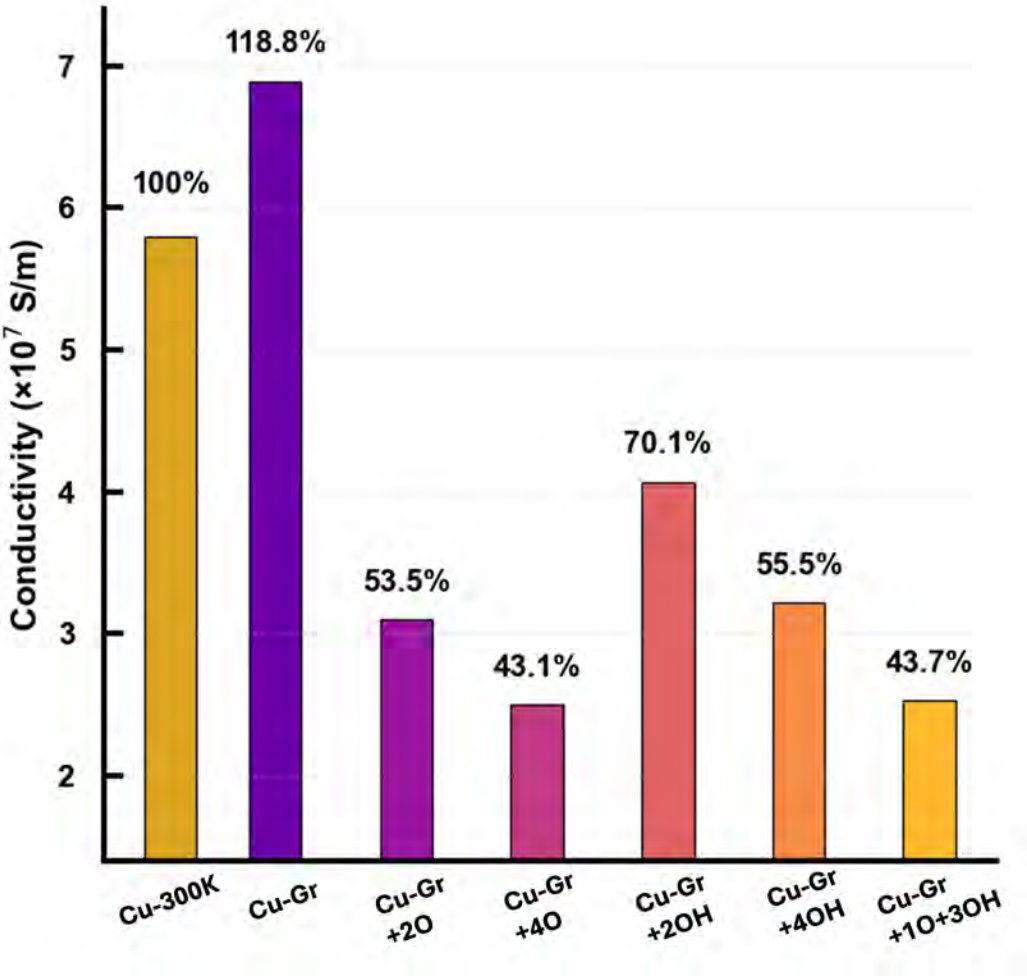

Figure 5.9: Electronic conductivity in Cu-Gr composites with oxides and hydroxides relative to the copper-only model calculated at 300 K.

conductivity for Cu-aGr composite with $n_6/n = 3.0$ is slightly higher than Cu-Gr composite with two OH functional groups in the microstructure.

Topological disorder in graphene affects the flow of carriers along the sp^2 connected carbon rings, as well as affects the overlap between graphene's pi-orbital with the interface copper. To visualize this, space-projected conductivity along the plane of graphene in the composite's microstructure is computed and shown in Figure 5.10 (c)[i]. Non-hexagonal

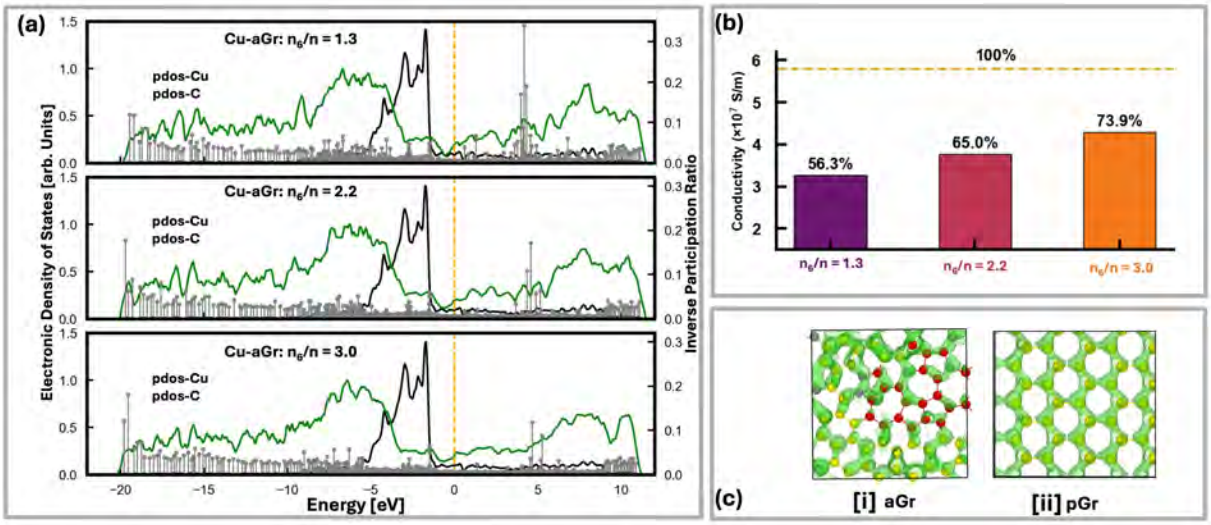

Figure 5.10: (a) Density of states projected into copper and carbon atoms for varying defect density in the graphene, as indicated by legends in subplots. (b) Relative KGF conductivities of Cu-aGr composites at varying n_6/n. (c) Space projected conductivity as an isosurface plot showing the electron conduction pathways in amorphous and pristine graphene. Red-colored sphere corresponds to carbon atoms participating in forming non-hexagonal rings.

rings with connecting atoms (depicted by red-colored atoms) limit the continuous flow of electrons as opposed to a homogenous and continuous flow of electrons in pristine graphene, shown as an isosurface (green color) plot in Figure 5.10(c) [ii]. By computing transverse space-projected conductivity, the electronic dynamics between the metal surface and pi orbitals in sp^2 graphene were assessed and compared to those of Cu-Gr composite. While there is poor electron activity at the interface for Cu-aGr composites, an increase at the interface and in the bulk was observed with reduced topological disorder. Figures 5.11 [i–iii] show the SPC as a heat map corresponding to Cu-aGr interfaces with $n_6/6$ = 1.3, 2.2,

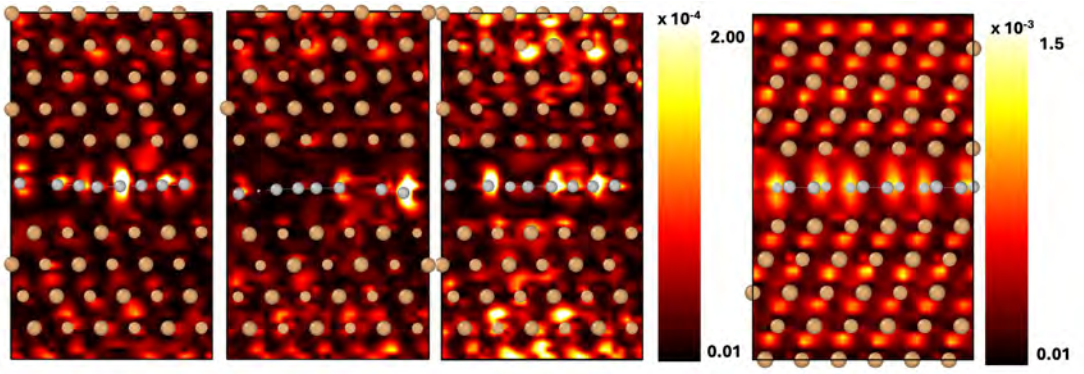

Figure 5.11: Transverse space projected conductivity as a heat map showing the conduction activity at copper-graphene microstructure with varying topological disorder density in (a) amorphous graphene and (b) pristine graphene. The colorbar shows the intensity of SPC increasing from dark to red to bright. Color Nomenclature: Brown: copper, grey: carbon.

and 3.0, respectively. The SPC intensity increases from black to red to bright, depicted by color bars.

Next, we introduce aGr with functional groups (-OH and -O) to model coal-derived graphene into a metal matrix. Coal-derived graphene is characterized by the presence of topological disorders and different oxidation groups on the graphene surface. For the rest of the analysis, we explicitly work on aGr with $n_6/6 = 3.0$. After relaxation, migration of functional groups from graphene to the copper interface was observed.

5.2.2.3.1 Cu-aGr With Oxides. Electronic density of states for the composite with oxides is shown in Figure 5.12 (a). No drastic variation in DoS was observed with increasing oxide in the material. We observed regions in the energy spectrum with several electronic states exhibiting some extent of localization as indicated by high IPR values in Figure 5.12(b). Localized states at energy -22 eV below the Fermi level are due to the oxide in the material microstructure. We observed peaks at ≈-8.5 eV below the Fermi level (labeled ”i”), -2 eV (labeled ”ii”), and states ”iii-iv” at energies ≈ 5 eV above the Fermi

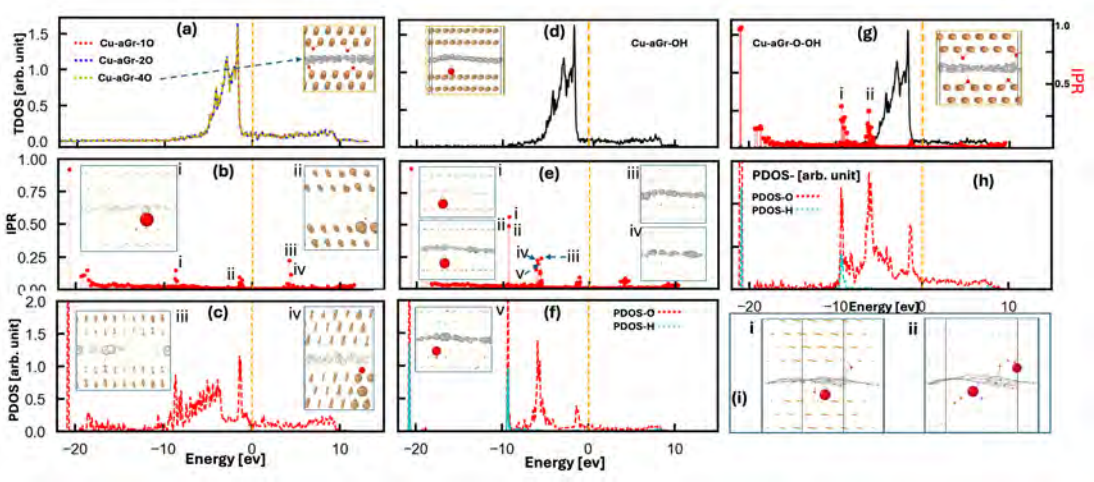

Figure 5.12: (a) Total electronic density of states (DOS) for Cu-Gr composites with oxides. The inset shows a representative interface structure of the relaxed composite model. (b) Electronic inverse participation ratio (IPR) depicting localized states at energies -22, -8.5, -1, and + 5 eV relative to the Fermi level (yellow vertical line at 0 eV). (c) Projected DOS into oxygen atoms. Note the peaks at PDOS into O atoms correspond to energies with localized states in (b), except at 5 eV above the Fermi level. Insets in (b) and (c) show the atom projection of these localized states. (d) EDOS for copper-graphene composites with hydroxide. (e) IPR depicting localized states at energies -21, -9, -6, and + 5 eV relative to the Fermi level (a yellow vertical line at 0 eV), labeled "i-v". (f) Projected DOS into oxygen atoms (red plots) and hydrogen atoms (blue plots). (g) [left axis] Total EDOS for Cu-Gr composites with different oxide and hydroxide. [Right axis] Electronic IPR depicting some localized states at energies -21 eV, -9 eV, -6 eV relative to the Fermi level (shown by a yellow vertical line at 0 eV), some are labelled "i-ii". (h) Projected DOS into oxygen atoms (red plots) and hydrogen atoms (blue plots). Note the peaks at PDOS into O and H atoms correspond to energies with localized states in (g). (i) Atom projection of localized states labeled "i-ii" in (g).

level. By computing projected DOS into the O atom, we see that oxygen present in the microstructure contributes to these localized states, shown in Figure 5.12 (c). However, O has no significant contribution to the localization of states above the Fermi level. The states i-iv are projected into the atoms weighted by their contribution to those states, shown as an inset in Figure 5.12(b-c). The size of the sphere corresponds to the weight of atoms in the electronic state. The state ”i” is primarily localized in the O atom and a C atom in its neighborhood, while state ”ii” is primarily localized in the interface copper atoms. Both states ”iii” and ”iv” are consequences of non-hexagonal rings in graphene, with state ”iv” showing the mixed contribution from oxygen and copper atoms.

5.2.2.3.2 Cu-aGr With Hydroxide. Electronic density of states for the composite with -OH is shown in Figure 5.12 (d) with an inset showing a relaxed microstructure of Cu-aGr interface with the OH group. We observed regions in the energy spectrum with several electronic states exhibiting some extent of localization as indicated by high IPR values in Figure 5.12(e). Notably, we observe two localized states (labeled ”i” and ”ii”) at ≈ -9.5 eV and a few states (labelled ”i-iv”) below -5 eV below the Fermi level. States ”i-ii” are explicitly due to the -OH group present in the material microstructure, as shown by PDOS in H atoms in Figure 5.12 (f), and atom projected IPR weighted by their contribution, shown in Figure 5.12(e) (inset). States ”iii-v” have contribution from C and O atom, as shown by the insets in Figure 5.12 (e-f).

5.2.2.3.3 Cu-aGr With Oxides and Hydroxides. Electronic density of states for the composite with -O and -OH is shown in Figure 5.12 (g) with an inset showing a relaxed microstructure of Cu-aGr interface. We observed regions in the energy spectrum with several electronic states exhibiting some extent of localization as indicated by high IPR values in Figure 5.12(g) [right axis]. We observe states at ≈ -9.5 eV and -6 eV below the Fermi level. exhibiting localization. These states, labeled ”i” and ”ii”, are explicitly due to

the -OH and -O present in the system, as shown by PDOS plots in Figure 5.12 (h). Further analysis was made on these states by projecting into atoms weighted by their contribution, shown in Figure 5.12(i).

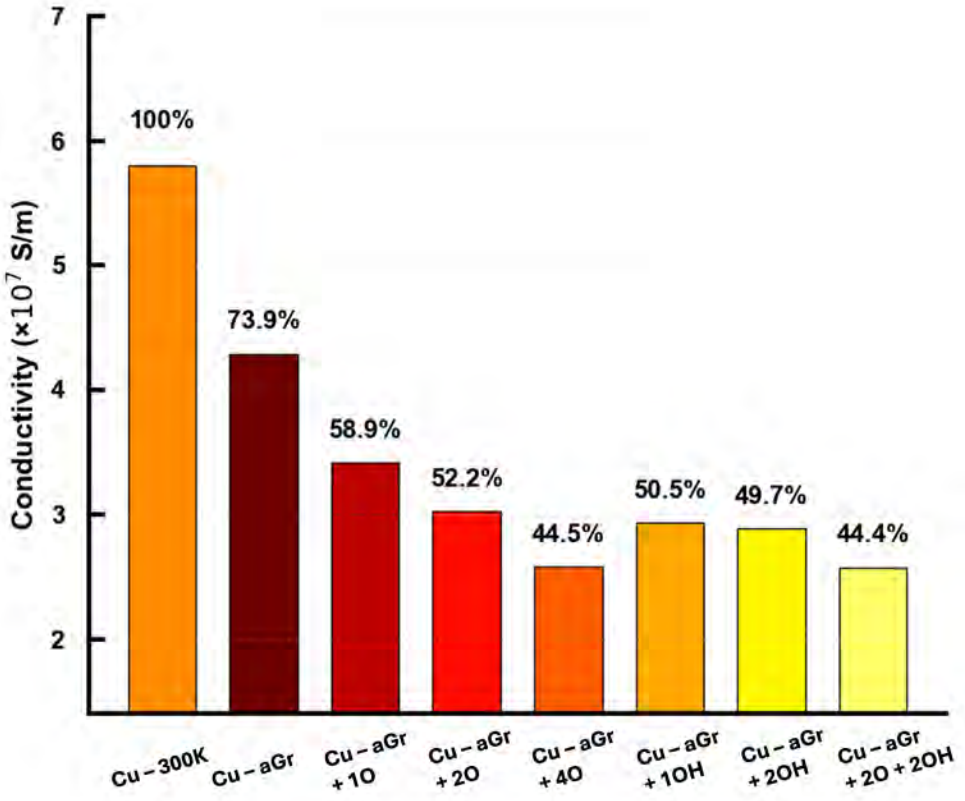

Figure 5.13: Relative KGF conductivities for copper-amorphous graphene composites with functional impurities compared to the standard IACS value for copper.

5.2.2.3.4 Electronic Conductivity of Cu-aGr With -O and -OH. Functional impurities in the material microstructure resulted in the localization of electronic states. These atoms act as a site for trapping carriers, limiting the flow of electrons in the microstructure. This results in reduced electronic conductivity of the material. With increasing O groups in the material, the conductivity decreases linearly. The computed

electronic conductivity for one, two, and four -O groups is ≈ 59 %, ≈ 52 %, and ≈ 45 % IACS, respectively. The conductivity of the composite model with one and two -OH groups is ≈ 51 % and 50 % IACS. The Cu-aGr model with two -O and two -OH composite is ≈ 44 % IACS. Figure 5.13 summarizes the KGF electronic conductivity for Cu-aGr models with different functional impurities. These observations show that the electronic conductivity of metal-graphene composites with a high impurity density likely remains similar regardless of the purity of graphene at the interface.

The space-projected conductivity was calculated for these composite models and is shown as isosurface plots in Figure 5.14. The reduction in total electronic conductivity with the introduction of functional impurities in the metal microstructure is due to diminished local SPC contributions, particularly evident by the weakened continuity of the isosurfaces at the interface. For aGr in a metal matrix, the isosurfaces show partial connectivity across the graphene layers, and the connectivity recovers as we go to the bulk metal, see Figure 5.14 (a). However, with functional impurities in the microstructure, a breakdown in isosurface connectivity is seen, not only at the metal-graphene interfaces but also within the bulk metal, as shown in Figure 5.14(b-f), indicating impaired electron transport in the metal microstructure.

5.3 Conclusion

In conclusion, our study investigated the structural, electronic, and transport properties of copper-coal composites, detailing the role of copper orientation, graphene structure, defect density, and chemical impurities in the composites microstructure. The striking atomic registry between the copper (111) and hexagonal graphene was observed to enhance the transport across the copper grains significantly. The influence of grain disorder at varying densities and with oxidation groups, such as oxides and hydroxides (common in

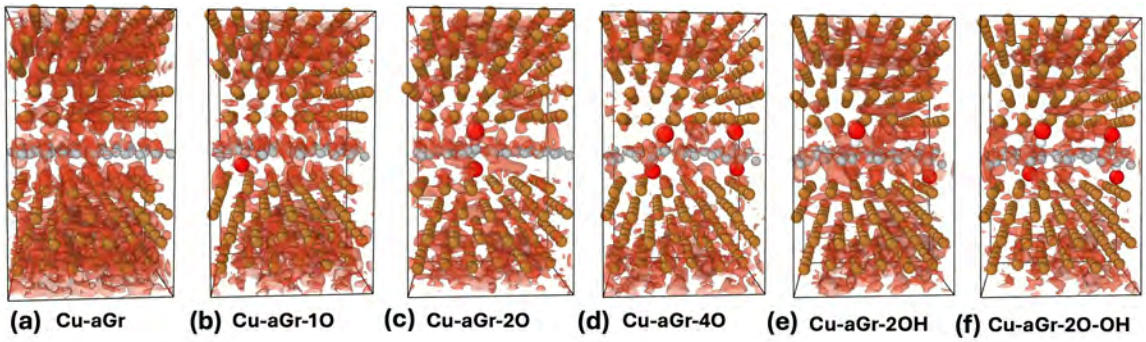

Figure 5.14: Space projected conductivity as a heat map showing the regions of active conduction at copper-amorphous graphene microstructure with functional impurities. We include 20 % of the highest local contributions to SPC in each plot. Color Nomenclature: Brown-copper, gray-carbon, red-oxygen, and white-hydrogen.

coal-derived graphene), on the electronic conductivity was analyzed. We noted a migration of functional groups from graphene to the interface copper, significantly influencing the interface structure and electronic properties. Strong reactivity between copper and oxygen was observed, leading to the formation of metal oxides in the microstructure of the material, which can be observed in experimentally extruded copper-graphene composites. These oxidation groups induce localized states below the Fermi level that act as carrier trapping sites, as evidenced by the accumulation of $\approx 1\ e^{-1}/atom$ and limiting the charge transfer to the carbon atoms from the copper interface. Additionally, the connecting atoms common to pentagonal and heptagonal rings in the graphene deteriorate the in-plane conductivity in graphene; the undulation structure due to non-hexagonal puckering affects the overlap between the graphene pi-orbitals and copper's electron sea, leading to the partial interaction between copper and graphene along the transverse direction. We showed this with the SPC plots.

This work provides one of the first realistic simulations for the potential of coal-derived graphene in the development of high-performance metal-coal conductors for motor applications and thus guides engineers in optimizing the different thermophysical conditions while extruding composites. For completeness, realistic calculations of conductivity at higher temperatures require phonon scattering; this can be addressed within an adiabatic approximation (thermal MD simulations on the canonical ensemble and by averaging the Kubo–Greenwood formula). The temperature dependence of electronic conductivity in composites will be detailed in the subsequent work.

6 Conclusion of Dissertation

In this dissertation, I have systematically investigated the electronic transport properties of metal–graphene composites and explored efficient computational frameworks for understanding transport in complex, disordered materials. Our studies show that in copper–graphene composites, electronic conductivity increases as the copper–graphene interfacial distance decreases and eventually saturates. This behavior is driven by enhanced charge transfer, an increased density of states near the Fermi level, and the direct participation of graphene in conduction pathways, as revealed by space-projected conductivity analyses. Similarly, in aluminum–graphene composites, first-principles calculations indicate that graphene can enhance the electronic density of states at the Fermi level for certain interfaces, with structural registry and layering (e.g., single vs. double graphene layers) influencing both interface structure and the temperature dependence of conductivity. Together, these results demonstrate that carefully engineered metal–graphene interfaces can actively improve electronic conduction by facilitating metal–carbon electronic coupling, and that atomic-scale interfacial structure plays a critical role in determining transport behavior in both copper- and aluminum-based composites.

Further investigations highlight the importance of atomic-scale disorder and impurities in modulating conductivity. In aluminum–graphene systems, incorporating amorphous or defective carbon at metal interfaces can still sustain enhanced conductivity compared to traditional defective graphene, as disorder and the presence of impurities such as nitrogen influence both the density of states at the Fermi level and the spatial pathways for electron transport. In copper–graphene composites, the crystallographic orientation of the metal and the presence of non-carbon impurities (e.g., N, O, S) modulate electronic conduction by altering interfacial registry and connectivity across grains. These findings collectively emphasize that optimized interfacial registry, controlled defect landscapes, and impurity

management are critical for tuning and enhancing charge transport in metal–carbon composites.

Additionally, we demonstrate that topological disorder in graphene, including non-hexagonal carbon rings and common functional impurities (such as oxides and hydroxides from coal-derived graphene), introduces localized electronic states that disrupt coherent electron flow. Functional groups primarily contribute states below the Fermi level, while structural disorder affects states above it. Moreover, both the anisotropy and the magnitude of the conductivity depend critically on the interplay between the quality of the graphene and the metal interface structure, emphasizing the need for careful control of these factors to optimize electronic transport.

From a methodological perspective, the N^2 method developed in this work provides an efficient and physically transparent surrogate framework for evaluating electronic transport in complex and disordered systems. By reformulating the Kubo–Greenwood conductivity in terms of pairwise band contributions at the Fermi level and exploiting the orthonormality and completeness of the Kohn–Sham states, the N^2 method avoids explicit summation over all virtual transitions while retaining the essential physics of conduction. This approach reduces computational cost without sacrificing accuracy, is compatible with both localized-basis and plane-wave basis first-principles calculations, and forms the theoretical foundation for space-projected conductivity analyses that directly identify spatially resolved conduction pathways. As such, the N^2 method bridges rigorous transport theory with practical computational scalability, enabling detailed atomic-scale insight into realistic materials.

In summary, this dissertation advances our understanding of electronic transport in metal–graphene composites and complex disordered materials, introduces efficient computational methodologies, and highlights the transformative potential of machine-learning approaches for large-scale simulations. Together, these contributions provide

a foundation for the rational design of high-performance materials and the predictive modeling of realistic systems at the atomic scale.

References

[1] A. Chowdhury and S. Bhattacharjee, "Experimental investigation of change in sheet resistance and Debye temperatures in metallic thin films due to low-energy ion beam irradiation," *Journal of Physics D: Applied Physics*, vol. 46, no. 43, p. 435304, 2013.

[2] W. Tang, E. Sanville, and G. Henkelman, "A grid-based bader analysis algorithm without lattice bias," *Journal of Physics: Condensed Matter*, vol. 21, no. 8, p. 084204, 2009.

[3] M. Aliofkhazraei, N. Ali, W. Milne, C. Ozkan, S. Mitura, and J. Gervasoni, *Graphene Science Handbook: Nanostructure and Atomic Arrangement*. 05 2016.

[4] W. Liu, Y. Han, J. Zhang, C. Zhang, and Y. Ding, "Advancing copper wire technology: Graphene/cu composites for superior conductivity and strength," *Applied Sciences*, vol. 14, p. 9273, Oct. 2024.

[5] K. Zhou, Y. Jia, D. Jia, J. Wang, W. Sun, Y. Wang, X. Kong, R. Zhang, and Y. Fu, "Progress of highly conductive graphene-reinforced copper matrix composites: A review," *Journal of Materials Research and Technology*, vol. 33, p. 7546–7571, Nov. 2024.

[6] M. Eid, S. Kaytbay, A. El-Assal, and O. Elkady, "Electrical, thermal, and mechanical characterization of hot coined carbon fiber reinforced pure aluminium composites," *Metals and Materials International*, vol. 28, p. 2747–2765, Mar. 2022.

[7] M. S, M. S, B. Y, and M. S. Dennison, "Microstructural evolution and performance analysis of mwcnt and gr reinforced aluminium matrix composites," *Discover Materials*, vol. 6, Dec. 2025.

[8] T. Li, Y. Wang, M. Yang, H. Hou, and S. Wu, "High strength and conductivity copper/graphene composites prepared by severe plastic deformation of graphene coated copper powder," *Materials Science and Engineering: A*, vol. 826, p. 141983, Oct. 2021.

[9] K. Nitheeshwaran, T. Padmanathan, S. Sakthi Vignesh, M. Shri Anantha Sayan, and M. Phanibhushana, "Study of microstructure and mechanical properties of metal matrix composites subjected to severe plastic deformation – a review," *Materials Today: Proceedings*, vol. 46, p. 799–805, 2021.

[10] K. S. Kappagantula, J. A. Smith, A. K. Nittala, and F. F. Kraft, "Macro copper-graphene composites with enhanced electrical conductivity," *Journal of Alloys and Compounds*, vol. 894, p. 162477, 2022.

[11] B. Gwalani, X. Li, A. Nittala, W. Choi, M. Reza-E-Rabby, J. Atehortua, A. Bhattacharjee, M. Pole, J. Silverstein, M. Song, and K. Kappagantula, "Unprecedented

electrical performance of friction-extruded copper-graphene composites," *Materials and Design*, vol. 237, p. 112555, 2023.

[12] A. Nittala, J. Smith, B. Gwalani, J. Silverstein, F. Kraft, and K. Kappagantula, "Simultaneously improved electrical and mechanical performance of hot-extruded bulk scale aluminum-graphene wires," *Materials Science and Engineering: B*, vol. 293, p. 116452, 2023.

[13] L. Weiping, L. Delong, F. Qiang, and P. Chunxu, "Conductive enhancement of copper/graphene composites based on a high-quality graphene," *RSC Advances*, vol. 5, pp. 80428–80433, 2015.

[14] H. Rho, Y. S. Jang, S. Kim, S. Bae, T.-W. Kim, D. S. Lee, J.-S. Ha, and S. H. Lee, "Porous copper–graphene heterostructures for cooling of electronic devices," *Nanoscale*, vol. 9, no. 22, pp. 7565–7569, 2017.

[15] Z. An, J. Li, A. Kikuchi, Z. Wang, Y. Jiang, and T. Ono, "Mechanically strengthened graphene-cu composite with reduced thermal expansion towards interconnect applications," *Microsystems Nanoengineering*, vol. 5, no. 1, p. 20, 2019.

[16] J. Yang, Y. He, X. Zhang, W. Yang, Y. Li, X. Li, Q. Chen, X. Chen, K. Du, and Y. Yan, "Improving the electrical conductivity of copper/graphene composites by reducing the interfacial impurities using spark plasma sintering diffusion bonding," *Journal of Materials Research and Technology*, vol. 15, pp. 3005–3015, 2021.

[17] T. Ellis, I. Anderson, H. Downing, and J. Verhoeven, "Deformation-processed wire prepared from gas-atomized cu-nb alloy powders," *Metallurgical Transactions A*, vol. 24, no. 1, pp. 21–26, 1993.

[18] D. M. Felicia, R. Rochiem, and S. M. Laia, "The effect of silver (ag) addition to mechanical and electrical properties of copper alloy (cu) casting product," *AIP Conference Proceedings*, vol. 1945, no. 1, p. 020075, 2018.

[19] L. Zheng, H. Zheng, D. Huo, F. Wu, L. Shao, P. Zheng, Y. Jiang, X. Zheng, X. Qiu, Y. Liu, *et al.*, "N-doped graphene-based copper nanocomposite with ultralow electrical resistivity and high thermal conductivity," *Scientific reports*, vol. 8, no. 1, pp. 1–7, 2018.

[20] C. M. e. a. Orofeo, "Influence of cu metal on the domain structure and carrier mobility in single-layer graphene," *Carbon*, vol. 50, no. 6, pp. 2189–2196, 2012.

[21] L. e. a. Banszerus, "Ultrahigh-mobility graphene devices from chemical vapor deposition on reusable copper," *Science Advances*, vol. 1, no. 6, p. e1500222, 2015.

[22] C. Pan, A. P. S. Gaur, M. Lynn, M. P. Olson, G. Ouyang, and J. Cui, "Enhanced electrical conductivity in graphene–copper multilayer composite," *AIP Advances*, vol. 12, no. 1, p. 015310, 2022.

[23] J. Zhang, C. Liang, and J. B. Dunn, "Graphite Flows in the U.S.: Insights into a Key Ingredient of Energy Transition," *Environmental Science & Technology*, vol. 57, no. 8, 2023.

[24] P. A. Advincula, W. Meng, L. J. Eddy, J. L. Beckham, I. R. Siqueira, D. X. Luong, W. Chen, M. Pasquali, S. Nagarajaiah, and J. M. Tour, "Ultra-high loading of coal-derived flash graphene additives in epoxy composites," *Macromolecular Materials and Engineering*, vol. 308, no. 6, p. 2200640, 2023.

[25] A. Azenkeng, N. E. Stanislowski, J. E. Tibbetts, and J. D. Laumb, "Laboratory-Scale Coal-Derived Graphene Process (Final Report)," tech. rep., University of North Dakota Energy & Environmental Research Center, 2023.

[26] Q. Zhou, Z. Zhao, Y. Zhang, B. Meng, A. Zhou, and J. Qiu, "Graphene sheets from graphitized anthracite coal: preparation, decoration, and application," *Energy & fuels*, vol. 26, no. 8, pp. 5186–5192, 2012.

[27] S. B. Singh, N. Haskin, and S. A. Dastgheib, "Coal-based graphene oxide-like materials: A comprehensive review," *Carbon*, p. 118447, 2023.

[28] S. Zhang, Q. Liu, H. Zhang, R. Ma, K. Li, Y. Wu, and B. J. Teppen, "Structural order evaluation and structural evolution of coal-derived natural graphite during graphitization," *Carbon*, vol. 157, pp. 714–723, 2020.

[29] L. Lin, H. Peng, and Z. Liu, "Synthesis challenges for graphene industry," *Nature materials*, vol. 18, no. 6, pp. 520–524, 2019.

[30] Y. Hernandez, V. Nicolosi, M. Lotya, F. M. Blighe, Z. Sun, S. De, I. T. McGovern, B. Holland, M. Byrne, Y. K. Gun'Ko, *et al.*, "High-yield production of graphene by liquid-phase exfoliation of graphite," *Nature nanotechnology*, vol. 3, no. 9, pp. 563–568, 2008.

[31] W. Lee, S. Jang, M. J. Kim, and J.-M. Myoung, "Interfacial interactions and dispersion relations in carbon–aluminium nanocomposite systems," *Nanotechnology*, vol. 19, p. 285701, jun 2008.

[32] Y. Liu, Y. Chen, J. Deng, and J. Wang, "N-doped aluminum-graphite (al-gr-n) composite for enhancing in-situ production and activation of hydrogen peroxide to treat landfill leachate," *Applied Catalysis B: Environmental*, vol. 297, p. 120407, 2021.

[33] J. Tokutomi, T. Uemura, S. Sugiyama, J. Shiomi, and J. Yanagimoto, "Hot extrusion to manufacture the metal matrix composite of carbon nanotube and aluminum with excellent electrical conductivities and mechanical properties.," *CIRP Annals - Manufacturing Technology*, vol. 64, 2015.

[34] C. Gong, D. Hinojos, W. Wang, N. Nijem, B. Shan, R. M. Wallace, K. Cho, and Y. J. Chabal, "Metal–graphene–metal sandwich contacts for enhanced interface bonding and work function control.," *ACS Nano*, vol. 6, pp. 5381–5387, 2012.

[35] F. A. Chyada, A. R. Jabur, and H. A. Alwan, "Effect addition of graphene on electrical conductivity and tensile strength for recycled electric power transmission wires," *Energy Procedia*, vol. 119, p. 121–130, 07 2017.

[36] L. Brown, P. Joyce, D. Forrest, and L. Salamanca-Riba, "Physical and mechanical characterization of a nanocarbon infused aluminum-matrix composite," *Materials Performance and Characterization*, vol. 3, no. 1, pp. 65–80, 2014.

[37] X. Zhang and S. Wang, "Interfacial strengthening of graphene/aluminum composites through point defects: A first-principles study.," *Nanomaterials (Basel)*, vol. 11, p. 3, 2021.

[38] D.-Y. Kim and H.-J. Choi, "Recent developments towards commercialization of metal matrix composites," *Materials*, vol. 13, no. 12, p. 2828, 2020.

[39] M. S. Ayar, P. M. George, and R. R. Patel, "Advanced research progresses in aluminium metal matrix composites: An overview," *AIP Conference Proceedings*, vol. 2317, no. 1, p. 020026, 2021.

[40] A. M. Ali, M. Z. Omar, H. Hashim, M. S. Salleh, and I. F. Mohamed, "Recent development in graphene-reinforced aluminium matrix composite: A review," *Reviews on Advanced Materials Science*, vol. 60, no. 1, pp. 801–817, 2021.

[41] M. Cao, Y. Luo, Y. Xie, Z. Tan, G. Fan, Q. Guo, Y. Su, Z. Li, and D.-B. Xiong, "The influence of interface structure on the electrical conductivity of graphene embedded in aluminum matrix," *Advanced Materials Interfaces*, vol. 6, no. 3, p. 1900468, 2019.

[42] W. Wang, Y. Liu, T. Wang, K. Sheng, and B. Yu, "Graphene/cu (111) interface study: The density functional theory calculations," in *2011 International Conference on Electronics, Communications and Control (ICECC)*, pp. 265–268, IEEE, 2011.

[43] Y. Li, F. Inam, A. Kumar, M. F. Thorpe, and D. A. Drabold, "Pentagonal puckering in a sheet of amorphous graphene," *physica status solidi (b)*, vol. 248, no. 9, pp. 2082–2086, 2011.

[44] V. Kapko, D. A. Drabold, and M. F. Thorpe, "Electronic structure of a realistic model of amorphous graphene," *physica status solidi (b)*, vol. 247, no. 5, pp. 1197–1200, 2010.

[45] A. Kumar, M. Wilson, and M. F. Thorpe, "Amorphous graphene: a realization of zachariasen's glass," *Journal of Physics: Condensed Matter*, vol. 24, p. 485003, oct 2012.

[46] Z. El-Machachi, M. Wilson, and V. L. Deringer, "Exploring the configurational space of amorphous graphene with machine-learned atomic energies," *Chem. Sci.*, vol. 13, pp. 13720–13731, 2022.

[47] A. Antidormi, L. Colombo, and S. Roche, "Emerging properties of non-crystalline phases of graphene and boron nitride based materials," *Nano Materials Science*, vol. 4, no. 1, pp. 10–17, 2022. Special issue on Graphene and 2D Alternative Materials.

[48] H. Tian, Y. Ma, and Z. Li et. al., "Disorder-tuned conductivity in amorphous monolayer carbon," *Nature*, vol. 615, pp. 56–71, 2023.

[49] R. Ravinder, R. Kumar, M. Agarwal, and N. M. A. Krishnan, "Evidence of a two-dimensional glass transition in graphene: Insights from molecular simulations," *Scientific Reports*, vol. 9, no. 1, 2019. Special issue on Graphene and 2D Alternative Materials.

[50] R. Thapa, C. Ugwumadu, K. Nepal, J. Trembly, and D. A. Drabold, "Ab initio simulation of amorphous graphite," *Phys. Rev. Lett.*, vol. 128, p. 236402, Jun 2022.

[51] C. Ugwumadu, K. Nepal, R. Thapa, Y. Lee, Y. Al Majali, J. Trembly, and D. Drabold, "Simulation of multi-shell fullerenes using machine-learning gaussian approximation potential," *Carbon Trends*, vol. 10, p. 100239, 2023.

[52] C. Ugwumadu, R. Thapa, Y. Al-Majali, J. Trembly, and D. A. Drabold, "Formation of amorphous carbon multi-walled nanotubes from random initial configurations," *physica status solidi (b)*, vol. 260, no. 3, p. 2200527, 2023.

[53] C. Ugwumadu, R. O. III, N. L. Smith, K. Nepal, Y. Al-Majali, J. Trembly, and D. A. Drabold, "Computer simulation of carbonization and graphitization of coal," *Nanotechnology*, vol. 35, p. 095703, dec 2023.

[54] M. Murakami, A. Tatami, and M. Tachibana, "Fabrication of high quality and large area graphite thin films by pyrolysis and graphitization of polyimides," *Carbon*, vol. 145, pp. 23–30, 2019.

[55] C. Badenhorst, C. Santos, J. Lázaro-Martínez, B. Białecka, M. Cruceru, A. Guedes, R. Guimarães, K. Moreira, G. Predeanu, I. Suárez-Ruíz, *et al.*, "Assessment of graphitized coal ash char concentrates as a potential synthetic graphite source," *Minerals*, vol. 10, no. 11, p. 986, 2020.

[56] S. Liu, J. Xue, X. Liu, H. Chen, and X. Li, "Pitch derived graphene oxides: Characterization and effect on pyrolysis and carbonization of coal tar pitch," *Journal of Analytical and Applied Pyrolysis*, vol. 145, p. 104746, 2020.

[57] X. Liu, J. Liu, D. Zhan, J. Yan, J. Wang, D. Chao, L. Lai, M. Chen, J. Yin, and Z. Shen, "Repeated microwave-assisted exfoliation of expandable graphite for the preparation of large scale and high quality multi-layer graphene," *RSC advances*, vol. 3, no. 29, pp. 11601–11606, 2013.

[58] A. K. Jehad, K. Kocabas, and M. Yurddaskal, "A comparative study for producing few-layer graphene sheets via electrochemical and microwave-assisted exfoliation from graphite powder," *Journal of Materials Science: Materials in Electronics*, vol. 31, pp. 7022–7034, 2020.

[59] P. Chamoli, M. K. Das, and K. K. Kar, "Structural, optical, and electrical characteristics of graphene nanosheets synthesized from microwave-assisted exfoliated graphite," *Journal of Applied Physics*, vol. 122, no. 18, 2017.

[60] R. Ye, D. K. James, and J. M. Tour, "Laser-induced graphene," *Accounts of chemical research*, vol. 51, no. 7, pp. 1609–1620, 2018.

[61] R. Ye, D. K. James, and J. M. Tour, "Laser-induced graphene: from discovery to translation," *Advanced Materials*, vol. 31, no. 1, p. 1803621, 2019.

[62] L. X. Duy, Z. Peng, Y. Li, J. Zhang, Y. Ji, and J. M. Tour, "Laser-induced graphene fibers," *Carbon*, vol. 126, pp. 472–479, 2018.

[63] W. Kohn, A. D. Becke, and R. G. Parr, "Density functional theory of electronic structure," *The journal of physical chemistry*, vol. 100, no. 31, pp. 12974–12980, 1996.

[64] R. M. Martin, *Electronic Structure: Basic Theory and Practical Methods*. Cambridge University Press, 2008.

[65] P. E. Blöchl, "Projector augmented-wave method," *Phys. Rev. B*, vol. 50, pp. 17953–17979, Dec 1994.

[66] P. E. Blöchl, "Projector augmented-wave method," *Phys. Rev. B*, vol. 50, pp. 17953–17979, Dec 1994.

[67] G. Kresse and J. Hafner, "Ab initio molecular dynamics for liquid metals," *Phys. Rev. B*, vol. 47, pp. 558–561, Jan 1993.

[68] J. M. Soler, E. Artacho, J. D. Gale, A. García, J. Junquera, P. Ordejón, and D. Sánchez-Portal, "The SIESTA method for *ab initio* materials simulation," *Journal of Physics: Condensed Matter*, vol. 14, no. 11, pp. 2745–2779, 2002.

[69] A. P. Thompson, H. M. Aktulga, R. Berger, D. S. Bolintineanu, W. M. Brown, P. S. Crozier, P. J. in 't Veld, A. Kohlmeyer, S. G. Moore, T. D. Nguyen, R. Shan, M. J. Stevens, J. Tranchida, C. Trott, and S. J. Plimpton, "LAMMPS - a flexible simulation tool for particle-based materials modeling at the atomic, meso, and continuum scales," *Computer Physics Communications*, vol. 271, p. 108171, 2022.

[70] G. Csanyi, "Research data: Machine learning a general-purpose interatomic potential for silicon," 2021.

[71] D. Unruh, R. V. Meidanshahi, S. M. Goodnick, G. Csányi, and G. T. Zimányi, "Gaussian approximation potential for amorphous si : H," *Physical Review Materials*, vol. 6, June 2022.

[72] R. Kubo, "Statistical-mechanical theory of irreversible processes. i. general theory and simple applications to magnetic and conduction problems," *J.Phys.Soc.Jpn*, vol. 12, no. 6, pp. 570–586, 1957.

[73] D. A. Greenwood, "The boltzmann equation in the theory of electrical conduction in metals," *Proc.Phys.Soc.*, vol. 71, pp. 585–596, apr 1958.

[74] P. B. Allen and J. Q. Broughton *J. Phys. Chem.*, vol. 91, p. 4964, 1987.

[75] S. Caravati, M. Bernasconi, and M. Parrinello, "First principles study of the optical contrast in phase change materials," *Journal of Physics: Condensed Matter*, vol. 22, p. 315801, jul 2010.

[76] K. N. Subedi, K. Prasai, and D. A. Drabold, "Space-projected conductivity and spectral properties of the conduction matrix, in "form and function of disorder"," *Phys. Status Solidi B*, vol. 258, p. 2000438, 2020.

[77] K. N. Subedi, K. Nepal, C. Ugwumadu, K. Kappagantula, and D. A. Drabold, "Electronic transport in copper–graphene composites," *Applied Physics Letters*, vol. 122, p. 031903, 2023.

[78] K. N. Subedi, K. Prasai, M. N. Kozicki, and D. A. Drabold, "Structural origins of electronic conduction in amorphous copper-doped alumina," *Phys. Rev. Materials*, vol. 3, p. 065605, Jun 2019.

[79] T. A. Abtew, M. Zhang, and D. A. Drabold, "Ab initio estimate of temperature dependence of electrical conductivity in a model amorphous material: Hydrogenated amorphous silicon," *Physical Review B*, vol. 76, July 2007.

[80] K. N. e. a. Subedi *Phys. Rev. Materials*, vol. 3, no. 6, p. 065605, 2019.

[81] J. M. Ziman, "Electrons and phonons: The theory of transport phenomena in solids," Oxford University Press, 1960.

[82] K. N. e. a. Subedi, "Electrical conduction processes in aluminum," *Phys. Rev. B*, vol. 105, no. 10, p. 104114, 2022.

[83] K. Nepal, C. Ugwumadu, K. N. Subedi, K. Kappagantula, and D. A. Drabold, "Physical origin of enhanced electrical conduction in aluminum-graphene composites," *Applied Physics Letters*, vol. 124, p. 091902, 02 2024.

[84] K. Nepal, C. Ugwumadu, A. Gautam, K. Kappagantula, and D. A. Drabold, "Electronic conductivity in metal-graphene composites: The role of disordered carbon structures, defects, and impurities," *Journal of Physics: Materials*, 2024.

[85] K. N. Subedi, K. Prasai, and D. A. Drabold, "Modeling of glasses: Electronic conduction mechanisms in $GeSe_3$: Ag and Al_2O_3: Cu," in *The world scientific reference of amorphous materials: Structure, Properties, Modeling and Main Applications Volume 1-Structure, Properties, Modeling and Applications of Amorphous Chalcogenides*, pp. 79–105, World Scientific, 2021.

[86] C. Ugwumadu, K. Subedi, R. Thapa, P. Apsangi, S. Swain, M. Kozicki, and D. Drabold, "Structure, vibrations and electronic transport in silicon suboxides: Application to physical unclonable functions," *Journal of Non-Crystalline Solids: X*, vol. 18, p. 100179, 2023.

[87] R. Thapa, B. Bhattarai, M. N. Kozicki, K. N. Subedi, and D. A. Drabold, "Structure and charge transport of amorphous cu-doped ta_2o_5: An ab initio study," *Phys. Rev. Mater.*, vol. 4, p. 064603, Jun 2020.

[88] K. Prasai, G. Chen, and D. A. Drabold, "Amorphous to amorphous insulator-metal transition in $GeSe_3$:Ag glasses," *Phys. Rev. Mater.*, vol. 1, p. 015603, Jun 2017.

[89] D. R. Basaula, M. Daeipour, B. Feygelson, and S. Nakhmanson, "Predicting thermoelectric figure of merit in complex materials: What do we need to know?," *Acta Materialia*, vol. 271, p. 119889, 2024.

[90] B. Xiao, T. Gu, T. Tada, and S. Watanabe, "Conduction paths in Cu/amorphous-Ta_2O_5/Pt atomic switch: First-principles studies," *Journal of Applied Physics*, vol. 115, no. 3, 2014.

[91] N. K. Hindley, "Random phase model of amorphous semiconductors ii. hot electrons," *Journal of Non-Crystalline Solids*, vol. 5, no. 1, pp. 31–40, 1970.

[92] L. Friedman and N. F. Mott, *THE HALL EFFECT NEAR THE METAL–INSULATOR TRANSITION*, pp. 529–534.

[93] L. Friedman, "Hall conductivity of amorphous semiconductors in the random phase model," *Journal of Non-Crystalline Solids*, vol. 6, no. 4, pp. 329–341, 1971.

[94] N. K. Hindley, "Random phase model of amorphous semiconductors i. transport and optical properties," *Journal of Non-Crystalline Solids*, vol. 5, no. 1, pp. 17–30, 1970.

[95] N. F. Mott, "Conduction in non-crystalline materials: Iii. localized states in a pseudogap and near extremities of conduction and valence bands," *Philosophical Magazine*, vol. 19, no. 160, pp. 835–852, 1969.

[96] M. H. Cohen, "Electronic structure and transport in covalent amorphous semiconducting alloys," *Journal of Non-Crystalline Solids*, vol. 2, pp. 432–443, 1970.

[97] N. Marzari, A. A. Mostofi, J. R. Yates, I. Souza, and D. Vanderbilt, "Maximally localized wannier functions: Theory and applications," *Rev. Mod. Phys.*, vol. 84, pp. 1419–1475, Oct 2012.

[98] U. Stephan and D. A. Drabold, "Order-*n* projection method for first-principles computations of electronic quantities and wannier functions," *Phys. Rev. B*, vol. 57, pp. 6391–6407, Mar 1998.

[99] U. Stephan, R. M. Martin, and D. A. Drabold, "Extended-range computation of wannier-like functions in amorphous semiconductors," *Phys. Rev. B*, vol. 62, pp. 6885–6888, Sep 2000.

[100] P. Ordejón, D. A. Drabold, R. M. Martin, and M. P. Grumbach, "Linear system-size scaling methods for electronic-structure calculations," *Phys. Rev. B*, vol. 51, pp. 1456–1476, Jan 1995.

[101] J. M. Luttinger, *Transport Theory*, ch. 4, pp. 157–193. Boston, MA: Springer US, 1968.

[102] N. F. Mott and E. A. Davis, "Theory of electrons in a non-crystalline medium," pp. 11–15, 1979.

[103] G. H. Wannier, "The structure of electronic excitation levels in insulating crystals," *Phys. Rev.*, vol. 52, pp. 191–197, Aug 1937.

[104] G. Henkelman, A. Arnaldsson, and H. Jónsson, "A fast and robust algorithm for bader decomposition of charge density," *Computational Materials Science*, vol. 36, no. 3, pp. 354–360, 2006.

[105] P. E. Blöchl, "Projector augmented-wave method," *Phys. Rev. B*, vol. 50, pp. 17953–17979, Dec 1994.

[106] J. P. Perdew, K. Burke, and M. Ernzerhof, "Generalized gradient approximation made simple [phys. rev. lett. 77, 3865 (1996)]," *Phys. Rev. Lett.*, vol. 78, pp. 1396–1396, Feb 1997.

[107] A. Belmonte, U. Celano, A. Redolfi, A. Fantini, R. Muller, W. Vandervorst, M. Houssa, M. Jurczak, and L. Goux *IEEE Trans.Elec.Devices*, vol. 62, p. 4349, 2015.

[108] D. Knyazev and P. levashov *Computational Materials Science*, vol. 79, p. 817, 2013.

[109] L. Calder'm, V. Karaseiv, and S. Trickey *Computer Physics Communications*, vol. 221, p. 118, 2017.

[110] P. Bulanchuk *Computational Materials Science*, vol. 261, p. 107714, 2021.

[111] T. L. Y. et al., "Ab initio study of stability and migration of point defects in copper-graphene layered composite," *Journal of Alloys and Compounds*, vol. 692, pp. 49–58, 2017.

[112] N. A. e. a. Lanzillo, "Pressure-enabled phonon engineering in metals," *PNAS*, vol. 111, no. 24, pp. 8712–8716, 2014.

[113] N. F. Mott and E. A. Davis, *Electronic Processes in Non-Crystalline Materials*. Oxford: Clarendon Press, 1979.

[114] H. J. Monkhorst and J. D. Pack, "Special points for brillouin-zone integrations," *Physical review B*, vol. 13, no. 12, p. 5188, 1976.

[115] S. Grimme, "Semiempirical gga-type density functional constructed with a long-range dispersion correction," *Journal of Computational Chemistry*, vol. 27, no. 15, pp. 1787–1799, 2006.

[116] K. N. Subedi, K. Kappagantula, F. Kraft, A. Nittala, and D. A. Drabold, "Electrical conduction processes in aluminum: Defects and phonons," *Phys. Rev. B*, vol. 105, p. 104114, Mar 2022.

[117] Y. Qi, L. G. Hector, N. Ooi, and J. B. Adams, "A first principles study of adhesion and adhesive transfer at al(111)/graphite(0001)," *Surface Science*, vol. 581, no. 2, pp. 155–168, 2005.

[118] W. Lee, S. Jang, M. J. Kim, and J. M. Myoung, "Interfacial interactions and dispersion relations in carbon–aluminium nanocomposite systems," *Nanotechnology*, vol. 19, p. 285701, 2008.

[119] Y. Qi and L. G. Hector, "Adhesion and adhesive transfer at aluminum/diamond interfaces: A first-principles study," *Phys. Rev. B*, vol. 69, p. 235401, Jun 2004.

[120] A. Samal, A. K. Kushwaha, D. Das, M. R. Sahoo, N. A. Lanzillo, and S. K. Nayak, "Thermal and electrical conductivity of copper-graphene heterosystem: An effect of strain and thickness," *Advanced Engineering Materials*, vol. 25, no. 13, p. 2201192, 2023.

[121] S. Ono, "C-axis resistivity of graphite in connection with stacking faults," *Journal of the Physical Society of Japan*, vol. 40, no. 2, pp. 498–504, 1976.

[122] N. Iwashita, H. Imagawa, and W. Nishiumi, "Variation of temperature dependence of electrical resistivity with crystal structure of artificial graphite products," *carbon*, vol. 61, pp. 602–608, 2013.

[123] S. Bapat, "Thermal conductivity and electrical resistivity of two types of ATJ-S graphite to 3500° k," *carbon*, vol. 11, pp. 511–514, 1973.

[124] K. Matsubara, K. Sugihara, and T. Tsuzuku, "Electrical resistance in the c direction of graphite," *Phys. Rev. B*, vol. 41, pp. 969–974, Jan 1990.

[125] D. X. Luong, K. V. Bets, W. A. Algozeeb, M. G. Stanford, C. Kittrell, W. Chen, R. V. Salvatierra, M. Ren, E. A. McHugh, P. A. Advincula, *et al.*, "Gram-scale bottom-up flash graphene synthesis," *Nature*, vol. 577, no. 7792, pp. 647–651, 2020.

[126] K. M. Wyss, D. X. Luong, and J. M. Tour, "Large-scale syntheses of 2d materials: Flash joule heating and other methods," *Advanced Materials*, vol. 34, no. 8, p. 2106970, 2022.

[127] K. Gong, F. Du, Z. Xia, M. Durstock, and L. Dai, "Nitrogen-doped carbon nanotube arrays with high electrocatalytic activity for oxygen reduction," *Science*, vol. 323, no. 5915, pp. 760–764, 2009.

[128] S. U. Lee, R. V. Belosludov, H. Mizuseki, and Y. Kawazoe, "Designing nanogadgetry for nanoelectronic devices with nitrogen-doped capped carbon nanotubes," *Small*, vol. 5, no. 15, pp. 1769–1775, 2009.

[129] F. Joucken, Y. Tison, J. Lagoute, J. Dumont, D. Cabosart, B. Zheng, V. Repain, C. Chacon, Y. Girard, A. R. Botello-Méndez, S. Rousset, R. Sporken, J.-C. Charlier, and L. Henrard, "Localized state and charge transfer in nitrogen-doped graphene," *Phys. Rev. B*, vol. 85, p. 161408, Apr 2012.

[130] P. Stumm and D. Drabold, "Structural and electronic properties of nitrogen doped fourfold amorphous carbon," *Solid State Communications*, vol. 93, no. 7, pp. 617–621, 1995.

[131] P. Stumm, D. A. Drabold, and P. A. Fedders, "Defects, doping, and conduction mechanisms in nitrogen-doped tetrahedral amorphous carbon," *Journal of Applied Physics*, vol. 81, pp. 1289–1295, 02 1997.

[132] J. Zhao, G. Zhu, W. Huang, Z. He, X. Feng, Y. Ma, X. Dong, Q. Fan, L. Wang, Z. Hu, *et al.*, "Synthesis of large-scale undoped and nitrogen-doped amorphous graphene on mgo substrate by chemical vapor deposition," *Journal of Materials Chemistry*, vol. 22, no. 37, pp. 19679–19683, 2012.

[133] K. Kappagantula, M. Reza-E-Rabby, A. Nittala, and P. Ottoni Negrao, "Ultra-Conductor Development for Enhanced EV Performance," *in "Vehicles Technology Office Materials Program FY 2022 Annual Progress Report*, pp. 127 – 133, 2022.

[134] J.-M. Zhang, F. Ma, and K.-W. Xu, "Calculation of the surface energy of fcc metals with modified embedded-atom method," *Applied Surface Science*, vol. 229, no. 1, pp. 34–42, 2004.

[135] Y. Wang, M. Li, P. Peng, H. Gao, J. Wang, and B. Sun, "Preferred orientation at the al/graphene interface: First-principles calculations and experimental observation," *Journal of Alloys and Compounds*, vol. 900, p. 163304, 2022.

[136] K. Nepal, C. Ugwumadu, K. N. Subedi, K. Kappagantula, and D. A. Drabold, "Physical origin of enhanced electrical conduction in aluminum-graphene composites," 2024.

[137] A. D. Becke and K. E. Edgecombe, "A simple measure of electron localization in atomic and molecular systems," *J. Chem. Phys.*, vol. 92, p. 5397–5403, May 1990.

[138] Q. Yang, J. Huang, S. Chen, Z. Ye, W. Wang, and J. Yang, "Influence of interfacial configuration on bonding properties and thermal conductivity of heterogeneous interface in al/graphite composite used for electronic packaging," *Surfaces and Interfaces*, vol. 35, p. 102452, 2022.

[139] S.-O. Guillaume, B. Zheng, J.-C. Charlier, and L. Henrard, "Electronic properties and stm images of doped bilayer graphene," *Phys. Rev. B*, vol. 85, p. 035444, Jan 2012.

[140] B. Zheng, P. Hermet, and L. Henrard, "Scanning tunneling microscopy simulations of nitrogen- and boron-doped graphene and single-walled carbon nanotubes," *ACS Nano*, vol. 4, 2010.

[141] F. Joucken, Y. Tison, J. Lagoute, J. Dumont, D. Cabosart, B. Zheng, V. Repain, C. Chacon, Y. Girard, A. R. Botello-Méndez, S. Rousset, R. Sporken, J.-C. Charlier, and L. Henrard, "Localized state and charge transfer in nitrogen-doped graphene," *Phys. Rev. B*, vol. 85, p. 161408, Apr 2012.

[142] R. Thapa, C. Ugwumadu, K. Nepal, J. Trembly, and D. A. Drabold, "Ab initio simulation of amorphous graphite," *Phys. Rev. Lett.*, vol. 128, p. 236402, Jun 2022.

[143] T. W. Ellis, I. E. Anderson, H. L. Downing, and J. D. Verhoeven, "Deformation-processed wire prepared from gas-atomized Cu-Nb alloy powders," *Metallurgical Transactions A*, vol. 24, no. 1, pp. 21–26, 1993.

[144] M. R. Akbarpour, F. Gazani, H. Mousa Mirabad, I. Khezri, A. Moeini, N. Sohrabi, and H. S. Kim, "Recent advances in processing, and mechanical, thermal and electrical properties of Cu-SiC metal matrix composites prepared by powder metallurgy," *Progress in Materials Science*, vol. 140, p. 101191, 2023.

[145] W. Li, D. Li, Q. Fu, and C. Pan, "Conductive enhancement of copper/graphene composites based on high-quality graphene," *RSC advances*, vol. 5, no. 98, pp. 80428–80433, 2015.

[146] F. Chen, J. Ying, Y. Wang, S. Du, Z. Liu, and Q. Huang, "Effects of graphene content on the microstructure and properties of copper matrix composites," *Carbon*, vol. 96, pp. 836–842, 2016.

[147] S. D. Rad, A. Islam, and A. Alnasser, "Development of metal–graphene-filled hybrid composites: Characterization of mechanical, thermal, and electrical properties," *Journal of Composite Materials*, vol. 53, no. 24, pp. 3363–3376, 2019.

[148] L. Adamska, Y. Lin, A. J. Ross, M. Batzill, and I. I. Oleynik, "Atomic and electronic structure of simple metal/graphene and complex metal/graphene/metal interfaces," *Phys. Rev. B*, vol. 85, p. 195443, May 2012.

[149] V. G. Konakov, O. Y. Kurapova, and I. Y. Archakov, "Improvement of copper–graphene composites properties due to the lubricating effect of graphene in the powder metallurgy fabrication process," *Metals and Materials International*, vol. 26, pp. 1899–1907, 2020.

[150] C. Gong, D. Hinojos, W. Wang, N. Nijem, B. Shan, R. M. Wallace, K. Cho, and Y. J. Chabal, "Metal–graphene–metal sandwich contacts for enhanced interface bonding and work function control," *ACS Nano*, vol. 6, no. 6, pp. 5381–5387, 2012.

[151] V. L. Deringer, N. Bernstein, G. Csányi, C. Ben Mahmoud, M. Ceriotti, M. Wilson, D. A. Drabold, and S. R. Elliott, "Origins of structural and electronic transitions in disordered silicon," *Nature*, vol. 589, no. 7840, pp. 59–64, 2021.

[152] J. Li and D. A. Drabold, "Electron hopping between localized states: A simulation of the finite-temperature Anderson problem using density functional methods," *Phys. Rev. B*, vol. 68, p. 033103, Jul 2003.

[153] T. A. Abtew and D. A. Drabold, "Thermally driven hopping and electron transport in amorphous materials from density functional calculations," *Journal of Physics: Condensed Matter*, vol. 16, p. S5289, oct 2004.

[154] T. A. Abtew, M. Zhang, and D. A. Drabold, "Ab initio estimate of temperature dependence of electrical conductivity in a model amorphous material: Hydrogenated amorphous silicon," *Phys. Rev. B*, vol. 76, p. 045212, Jul 2007.

[155] N. F. Mott and E. A. Davis, "Theory of electrons in a non-crystalline medium," in *Electronic Processes in Non-crystalline Materials*, ch. 6, pp. 209–235, Clarendon/Oxford University Press, Oxford, New York, 2 ed., 1979.

[156] C. Ugwumadu, D. A. Drabold, N. L. Smith, J. Trembly, R. Olson, E. Shereda, and Y. T. Al-Majali, "The structure of appalachian coal: Experiments and ab initio modeling," *Carbon*, vol. 225, p. 119086, 2024.

[157] H. Ren, "Graphene and its derivatives for electrochemical sensing," *Sensors*, vol. 25, p. 1993, Mar. 2025.

[158] J. Miao and T. Fan, "Flexible and stretchable transparent conductive graphene-based electrodes for emerging wearable electronics," *Carbon*, vol. 202, pp. 495–527, 2023.

[159] C. Dai, G. Sun, L. Hu, Y. Xiao, Z. Zhang, and L. Qu, "Recent progress in graphene-based electrodes for flexible batteries," *InfoMat*, vol. 2, p. 509–526, Sept. 2019.

[160] M. Gautam, S. Kanade, and B. B. Kale, "Electrochemical energy storage and conversion applications of graphene oxide: A review," *Energy amp; Fuels*, vol. 37, p. 17134–17160, Oct. 2023.

[161] Y.-X. Yu, "Can all nitrogen-doped defects improve the performance of graphene anode materials for lithium-ion batteries?," *Physical Chemistry Chemical Physics*, vol. 15, no. 39, p. 16819, 2013.

[162] D. Berman, A. Erdemir, and A. V. Sumant, "Graphene: a new emerging lubricant," *Materials Today*, vol. 17, p. 31–42, Jan. 2014.

[163] W. Frazier and K. S. Kappagantula, "A computational study of the effects of graphene additions on electrical properties of polycrystalline copper," *Composites Communications*, vol. 52, p. 102124, Dec. 2024.

[164] K. Nepal, C. Ugwumadu, F. Kraft, Y. Al-Majali, and D. Drabold, "The effects of crystal orientation and common coal impurities on electronic conductivity in copper–carbon composites," *Carbon*, vol. 231, p. 119711, Jan. 2025.

[165] M. Shi, C. Song, Z. Tai, K. Zou, Y. Duan, X. Dai, J. Sun, Y. Chen, and Y. Liu, "Coal-derived synthetic graphite with high specific capacity and excellent cyclic stability as anode material for lithium-ion batteries," *Fuel*, vol. 292, p. 120250, 2021.

[166] L. Yuan, Q. Liu, J. P. Mathews, H. Zhang, and Y. Wu, "Quantifying the structural transitions of chinese coal to coal-derived natural graphite by xrd, raman spectroscopy, and hrtem image analyses," *Energy & Fuels*, vol. 35, no. 3, pp. 2335–2346, 2021.

[167] B. Xing, C. Zhang, Y. Cao, G. Huang, Q. Liu, C. Zhang, Z. Chen, G. Yi, L. Chen, and J. Yu, "Preparation of synthetic graphite from bituminous coal as anode materials for high performance lithium-ion batteries," *Fuel processing technology*, vol. 172, pp. 162–171, 2018.

[168] Y.-M. Wang and C.-H. Zhang, "Study on structural evolution of synthetic graphite derived from lignite prepared by high temperature–high pressure method," *Crystals*, vol. 12, no. 4, p. 464, 2022.

[169] Y. Li, F. Inam, A. Kumar, M. F. Thorpe, and D. A. Drabold, "Pentagonal puckering in a sheet of amorphous graphene," *physica status solidi (b)*, vol. 248, p. 2082–2086, July 2011.

[170] D. Odkhuu, D. Shin, R. S. Ruoff, and N. Park, "Conversion of multilayer graphene into continuous ultrathin sp3-bonded carbon films on metal surfaces," *Scientific Reports*, vol. 3, Nov. 2013.

[171] X.-W. Yi, Z. Zhang, Z.-W. Liao, X.-J. Dong, J.-Y. You, and G. Su, "T-carbon: Experiments, properties, potential applications and derivatives," *Nano Today*, vol. 42, p. 101346, Feb. 2022.

[172] K. Prasai, P. Biswas, and D. A. Drabold, "Sculpting the band gap: a computational approach," *Scientific Reports*, vol. 5, Oct. 2015.

[173] K. Prasai, P. Biswas, and D. A. Drabold, "Electronically designed amorphous carbon and silicon," *physica status solidi (a)*, vol. 213, p. 1653–1660, Feb. 2016.